

博士論文

Development of Numerical Model for The Safety Design
Against Unstable Ductile Fracture in Offshore Pipelines

(海底パイプライン不安定延性破壊防止設計のための
数値モデル開発)

中居 寛明

Acknowledgment

A part of the present study was supported by JAPEX(JAPAN PETROLEUM EXPLORATION CO.,LTD.). Especially, I am sincerely grateful to Mr.Kazumoto Chiba, Mr.Satoshi Mori and Mr.Takamasa Miyadai from JAPEX for their support and advice from the engineering point of view.

I would like to express the deepest appreciation to my Professor Dr.Shuji Aihara, you have been always a great teacher for me. You have been spending your time for my study not only on weekdays but also on weekends. Your advice always moved my study one step further. I also would like to thank you for growing me as a researcher. You will be my role model as a researcher forever.

I also would like to thank technical staff Mr.Akiyasu Morita for considerable help in conducting difficult experiments. Words cannot express how I am grateful for your massive contribution and commitment. I also thank you for encouraging me with funny and informative talk.

I also want to thank technical staff Mr.Shigehiro Kaneda for helping my experiments. You are experiment expert, and I learned many tips for successful experiments from you. I also would like to thank Dr.Masatoshi Tsukamoto, you are the best expert of pipe burst tests in Japan. Your advice contributed greatly to the successful experiments.

I also want to express deep appreciation to Lecturer Dr.Kazuki Shibanuma, you have been always giving me precise advice which resulted in successful completion of my study. I also want to thank you for showing me how enjoyable research is by your own attitude.

I also would like to thank my colleague, Mr.Masaki Mitsuya, Mr.Itsuki Kawata, Mr.Kazuteru Tsumura, Mr.Shuheii Yoshizu, Mr.Masaki Sano and Mr.Kuriya Miyamoto for letting Aihara Lab. be an enjoyable and informative place. Discussions with you colleagues grew me as not only a researcher but also a person. Also, funny talks encouraged and relaxed me.

A special thanks to my family. Your support was always with me.

Contents

1	Introduction	1
1.1	Background	2
1.1.1	Growing supply of natural gas	2
1.1.2	Offshore pipelines for CCS	2
1.1.3	Situation of offshore pipelines	5
1.1.3.1	Offshore pipelines in America and Europe	5
1.1.3.2	Offshore pipelines in Japan	6
1.1.4	Fracture in pipelines	9
1.1.4.1	Fracture types	9
1.1.4.2	Unstable ductile fracture	11
1.2	Previous studies on unstable ductile fracture	13
1.2.1	Methods for evaluating unstable ductile crack prop- agation	13
1.2.1.1	Battelle Two-Curve method	13
1.2.1.2	HLP method	13
1.2.1.3	Finite element based model and other mod- els	14
1.2.2	Methods for offshore pipelines	15
1.2.3	Existing full-scale offshore pipeline burst tests . .	18
1.3	Objectives of the present study	20
1.4	Structure of the thesis	20
2	Basic theories	23
2.1	Compressible fluid mechanics	23
2.1.1	State equation	23
2.1.2	Mass conservation in one-dimensional flow	23
2.1.3	Momentum conservation in one-dimensional flow .	24
2.1.4	Energy conservation law(isentropic process)	24
2.1.5	Acoustic velocity	26

2.1.6	Choked flow	26
2.2	Bubble growth equation	28
2.3	Relationship between displacements and strains of a shell element in a thin cylinder under finite deformation	31
2.4	Summary	33
3	The UT offshore model description	35
3.1	Overview of the UT offshore model	35
3.2	Pipe deformation model	36
3.2.1	Governing equation	36
3.2.2	Water backfill effect	43
3.3	Gas decompression model	46
3.3.1	Governing equations	46
3.3.2	Gas leak	47
3.3.2.1	Gas leak from pipe to bubble through crack opening	47
3.3.2.2	Gas leak in the axial direction from the full bore opening at the pipe center to the bubble	51
3.4	Bubble growth model	52
3.4.1	Governing equations	52
3.4.2	Generation of a new node depending on crack prop- agation	55
3.5	Crack propagation model	55
3.6	Calculation flow	57
3.7	An example of calculation result	59
3.8	Summary	67
4	Underwater rupture tests	69
4.1	Testing conditions	69
4.2	Test results	78
4.2.1	Overview of the results	78
4.2.2	The history of the bubble growth	94
4.3	Calculation results for the validation of the bubble growth modeling in the UT offshore models	98
4.4	Summary	106

5	Calculation for the full-scale offshore pipeline burst test	107
5.1	Testing conditions	107
5.2	Testing result	109
5.3	Calculated result	111
5.4	Summary	111
6	Parametric study	115
6.1	Reference conditions	115
6.2	Water depth	115
6.3	Pipe thickness	116
6.4	Pipe outer diameter	119
6.5	Pipe grade(tensile yield strength)	119
6.6	Toughness	121
6.7	Summary	123
7	Conclusions	125
7.1	Summary of the present study	125
7.2	Future works	128
	Bibliography	131

List of Figures

1.1	World total primary energy supply from 1971 to 2012 . . .	3
1.2	Natural gas production from 1971 to 2013 by region	3
1.3	Total energy demand in Japan from 1965 to 2012 by fuel .	4
1.4	Transportation cost of natural gas in Northeast Asia	4
1.5	Schematic showing elements of CCS infrastructure	5
1.6	Pipeline grids in Europe	7
1.7	The route of the Nord Stream	7
1.8	Offshore pipeline projects from 1966 to 2012 including projects under construction, showing depth and length of each project	8
1.9	Pipelay vessel Castoro Sei	8
1.10	Pipe installation methods: S-lay and J-lay	9
1.11	Sakhalin project in Japan	10
1.12	Mechanism of unstable ductile crack propagation	12
1.13	Photo of unstable ductile crack propagation	12
1.14	Battelle two-curve method	14
1.15	An example calculated result for the full-scale natural gas pipeline burst tests with and without soil backfill	16
1.16	The effect of soil backfill depth on unstable ductile crack propagation	16
1.17	Ductile fracture correlations between air, sand and water backfill	17
1.18	Dependence of kinds of backfill on crack resistance curve in BTC	18
1.19	A photo of full-scale offshore pipeline burst test	19
2.1	Mass conservation in one-dimensional compressible gas flow	24
2.2	Momentum conservation in one-dimensional compressible gas flow	25
2.3	One-dimensional choked flow	27

2.4	A bubble in non-compressible liquid	28
2.5	Bubble surface	30
2.6	Deformation of thin cylindrical shell element	31
3.1	Overview of the fracture behavior in offshore pipelines . .	36
3.2	Coordinates and displacements of deformed pipe	37
3.3	Shape parameter ψ determining pipe deformation	38
3.4	Thin-shell element receiving forces and bending moment .	40
3.5	Distribution of stress and strain generated by bending mo- ment in thickness direction	40
3.6	Water backfill around a pipe	45
3.7	Dependence of shape parameter and water depth on added density, $\rho_{\text{water}} = 1,000\text{kg/m}^3$, $R_0 = 12\text{inch}$ and $h =$ 30mm	45
3.8	Mass conservation of fluid with leakage from a crack opening	48
3.9	Crack opening length of deformed pipe	48
3.10	Gas leakage from a pipe to a bubble	50
3.11	Dependence of the ratio of leaking pressure to internal pres- sure on function H determining mass flow rate	50
3.12	Dependence of mass flow rate on bubble pressure and ini- tial pressure	51
3.13	One-dimensional compressible gas glow with increasing cross sectional area inside a bubble	54
3.14	Calculation flow chart	58
3.15	Crack tip position versus crack velocity	60
3.16	3D pipe view at 17.5ms	61
3.17	3D pipe view at 35.1ms	61
3.18	3D pipe view at 52.6ms	62
3.19	3D bubble view at 17.5ms	62
3.20	3D bubble view at 35.1ms	63
3.21	3D bubble view at 52.6ms	63
3.22	History of pressure distribution inside a pipe at each time .	64
3.23	History of flow rate distribution inside a pipe at each time .	64
3.24	History of bubble pressure distribution at each time	65
3.25	History of flow rate distribution in a bubble at each time . .	65
3.26	History of bubble radius distribution at each time	66
3.27	History of bubble growth rate distribution at each time . .	66

4.1	Tested pipe arrangement, top view	70
4.2	Surface notch geometry	71
4.3	Water tank	73
4.4	Water tank	74
4.5	Window for high-speed camera and lighting	74
4.6	Tested pipe setting	74
4.7	High-speed camera and lighting	75
4.8	Photo of the test	75
4.9	Pressurizing system and instruments for measurements . .	76
4.10	Photo of pipe setting	76
4.11	Photo during the test	77
4.12	Photo of the tested pipe in the water	77
4.13	Photo of tested pipe after the burst for No.1	79
4.14	Fractured tested pipe for No.1	80
4.15	Fractured tested pipe for No.2	80
4.16	Time histories of dynamic internal and external pressure for No.1	81
4.17	Time histories of dynamic internal and external pressure for No.2	81
4.18	Bubble profile at 0ms after the burst for No.1, side view . .	82
4.19	Bubble profile at 2ms after the burst for No.1, side view . .	82
4.20	Bubble profile at 4ms after the burst for No.1, side view . .	83
4.21	Bubble profile at 6ms after the burst for No.1, side view . .	83
4.22	Bubble profile at 20ms after the burst for No.1, side view . .	84
4.23	Bubble profile at 40ms after the burst for No.1, side view . .	84
4.24	Bubble profile at 0ms after the burst for No.1, axial view . .	85
4.25	Bubble profile at 2ms after the burst for No.1, axial view . .	85
4.26	Bubble profile at 4ms after the burst for No.1, axial view . .	86
4.27	Bubble profile at 6ms after the burst for No.1, axial view . .	86
4.28	Bubble profile at 20ms after the burst for No.1, axial view . .	87
4.29	Bubble profile at 40ms after the burst for No.1, axial view . .	87
4.30	Bubble profile at 0ms after the burst for No.2, side view . .	88
4.31	Bubble profile at 2ms after the burst for No.2, side view . .	88
4.32	Bubble profile at 4ms after the burst for No.2, side view . .	89
4.33	Bubble profile at 6ms after the burst for No.2, side view . .	89
4.34	Bubble profile at 20ms after the burst for No.2, side view . .	90
4.35	Bubble profile at 40ms after the burst for No.2, side view . .	90

4.36	Bubble profile at 0ms after the burst for No.2, axial view	91
4.37	Bubble profile at 2ms after the burst for No.2, axial view	91
4.38	Bubble profile at 4ms after the burst for No.2, axial view	92
4.39	Bubble profile at 6ms after the burst for No.2, axial view	92
4.40	Bubble profile at 20ms after the burst for No.2, axial view	93
4.41	Bubble profile at 40ms after the burst for No.2, axial view	93
4.42	Transparent board with white grids at the same position as the tested pipes, captured by high-speed camera	95
4.43	An example of bubble outline traced by yellow line	95
4.44	An example of bubble profile, bubble radius distribution	96
4.45	Time history of bubble profile at each time for No.1	96
4.46	Time history of bubble profile at each time for No.2	97
4.47	Calculated time history of dynamic internal pressure for No.1	100
4.48	Calculated time history of dynamic internal pressure for No.2	101
4.49	Calculated bubble profile at 2ms after the burst for No.1	101
4.50	Calculated bubble profile at 4ms after the burst for No.1	102
4.51	Calculated bubble profile at 6ms after the burst for No.1	102
4.52	Calculated time history of bubble radius at the pipe center for No.1	103
4.53	Calculated bubble profile at 2ms after the burst for No.2	103
4.54	Calculated bubble profile at 4ms after the burst for No.2	104
4.55	Calculated bubble profile at 6ms after the burst for No.2	104
4.56	Calculated time history of bubble radius at the pipe center for No.2	105
5.1	Tested pipe arrangement and Charpy energy of each pipe	108
5.2	Instrumentation layout	108
5.3	Photos of the test showing high water column	109
5.4	Experimental time histories of internal pressure 3.4m and 18m away from the pipe center	110
5.5	Experimental time histories of the crack length	110
5.6	Calculated time histories of internal pressure 3.4m and 18m away from the pipe center	113
5.7	Calculated crack tip position versus crack velocity	113
6.1	Dependence of crack propagation/arrest on water depth	117
6.2	Dependence of internal pressure distributions on water depth, t=50ms	117

6.3	Dependence of crack propagation/arrest on pipe thickness .	119
6.4	Dependence of crack propagation/arrest on pipe outer diameter	120
6.5	Dependence of crack propagation/arrest on tensile yield stress (pipe grade)	121
6.6	Dependence of crack propagation/arrest on toughness . . .	122

List of Tables

3.1	Calculation condition	60
4.1	Testing condition	72
4.2	Pressure(MPa) at the rupture	78
4.3	Calculation condition	100
5.1	Testing condition	108
5.2	Reference conditions for the parametric studies	112
6.1	Reference conditions for the parametric study	116
6.2	Changed water depth	116
6.3	Changed pipe thickness	118
6.4	Changed pipe outer diameter	120
6.5	Changed pipe grade	120
6.6	Changed toughness	122

Chapter 1

Introduction

Recently, the demand for natural gas has been increasing rapidly around the world. There are two major methods for natural gas transportation: pipelines and liquefied natural gas carrier. Pipelines are usually chosen when transportation distance is shorter than several thousand kilometers. Especially, offshore pipelines might give us a good solution due to advantages as follows:

- offshore pipelines build a shortest connection between countries across the deep sea.
- procuring of site for laying offshore pipelines is usually easier than that for laying onshore pipeline, though negotiation with fishery is necessary.
- laying cost for offshore pipelines is lower than that for onshore pipelines especially in Japan.

However, a method for the safety design against fractures in offshore pipelines still has a number of uncertain aspects. In the present study, the author developed a numerical model for unstable ductile fracture in offshore pipelines, which is one of major fracture types in pipelines, and also conducted small-scale pipe rupture tests to validate the model.

In this chapter, background and objectives of the present study are described. Also, previous studies for unstable ductile fracture in pipelines are presented to clarify the motivation of the present study.

1.1 Background

1.1.1 Growing supply of natural gas

World energy consumption has been growing rapidly with economic growth of developing countries in Asia and Africa, see Fig. 1.1[1]. Especially, production of the natural gas is increasing notably due to its rich deposit, low carbon dioxide emission, high heat efficiency, see Fig. 1.2[1]. In addition, production of non-conventional natural gas such as shale gas and methane hydrate is expanding[2]. Therefore, natural gas production is expected to keep increasing in the future.

In Japan, the use of natural gas which was imported from overseas started instead of the use of naphtha since about 1967, and the use of natural gas in major cities started after a few years. Since then, the supply of natural gas has been increasing continuously, and natural gas is now one of key energy resources, see Fig. 1.3. Especially, the supply of natural gas is expected to be accelerated as a substitution for nuclear energy after Fukushima nuclear accident in 2011.

For the use of natural gas, methods for transporting it from production area to consumption area are necessary. There are two major methods for the transportation: pipelines and liquefied natural gas carrier. The more economical method depending on transportation distance is chosen. Provisional calculation suggests that when Japan imports natural gas from East Asia and Southeast Asia, transportation by pipelines should be more economical way if transportation distance is shorter than about 4,300km, see Fig. 1.4[3, 4]. Because Japan is surrounded by the sea, transportation by offshore pipelines might be best way.

1.1.2 Offshore pipelines for CCS

CCS(Carbon Capture & Storage) is now regarded as one of the most effective way to reduce carbon dioxide emissions, where waste carbon dioxide is captured in power plants, and transported into storage site, then deposited there. Recently, the use of CCS has been expanding around the world[6, 7]. Pipelines play an important role in transporting waste carbon dioxide into storage site. Especially, offshore pipelines are necessary when storage site is located under the seabed, see Fig. 1.5.

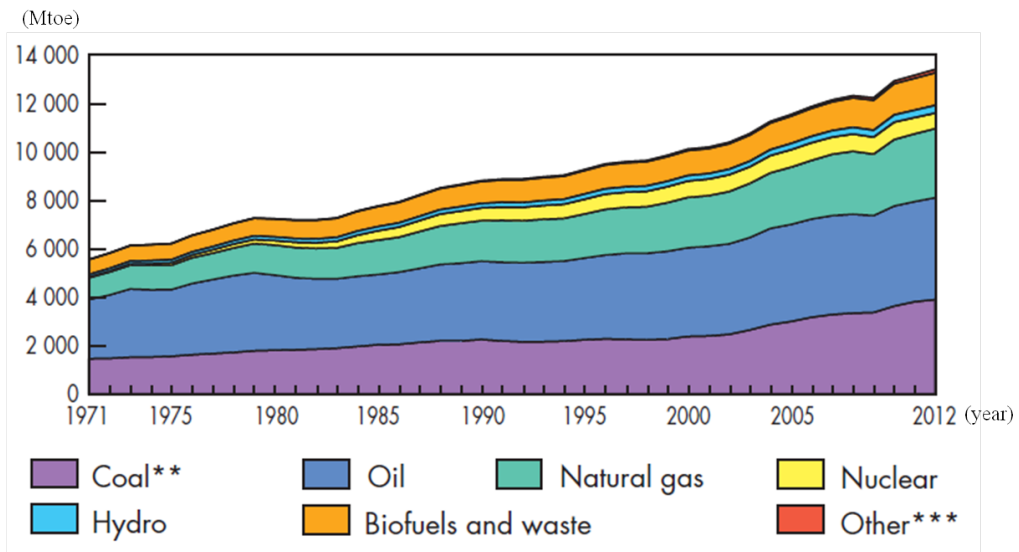


Fig. 1.1 World total primary energy supply from 1971 to 2012[1]

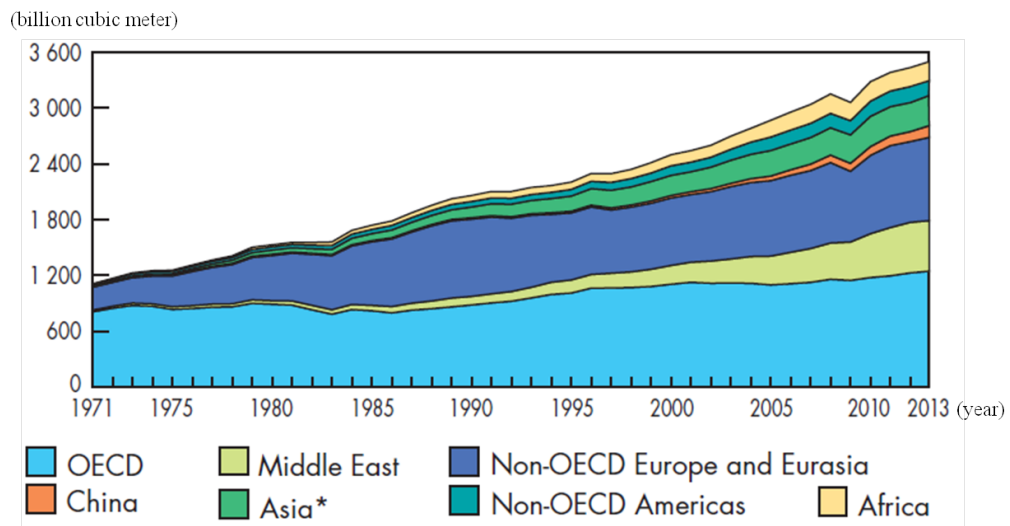


Fig. 1.2 Natural gas production from 1971 to 2013 by region[1]

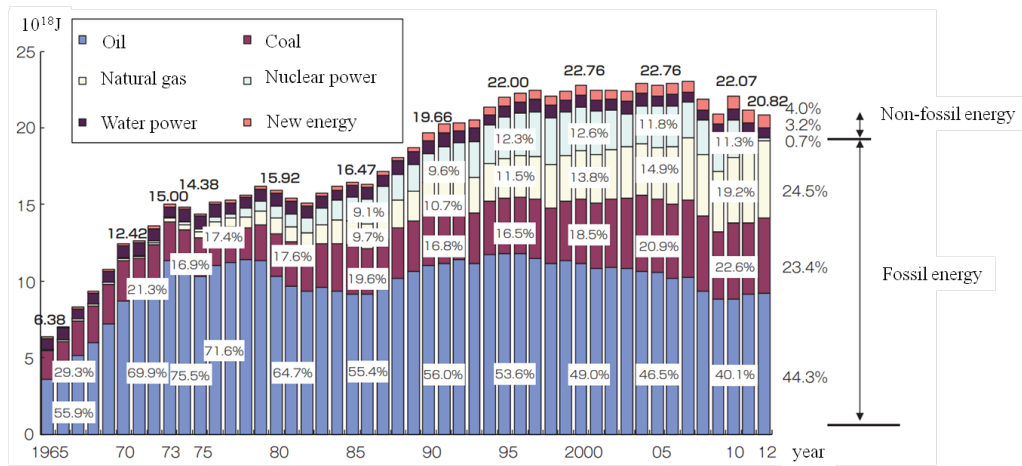


Fig. 1.3 Total energy demand in Japan from 1965 to 2012 by fuel(edited from [5])

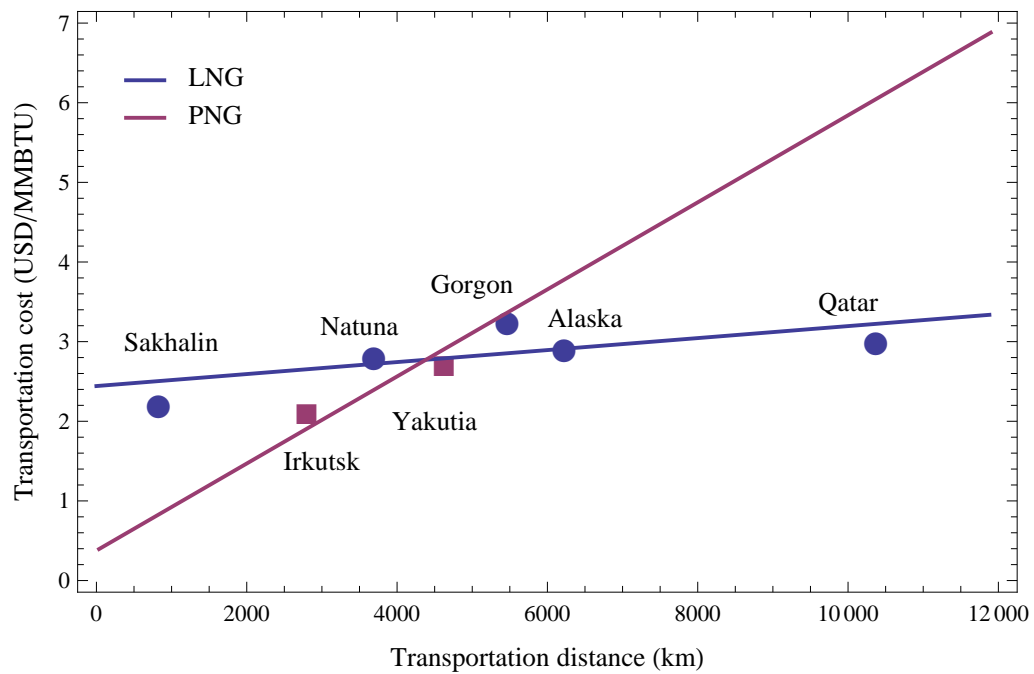


Fig. 1.4 Transportation cost of natural gas in Northeast Asia[4]

If pipelines transporting natural gas from production area to consumption area are regarded as arteries of energy, pipelines for CCS is regarded as veins of energy. Pipelines which have roles of arteries and veins of energy are crucially important in energy industry.

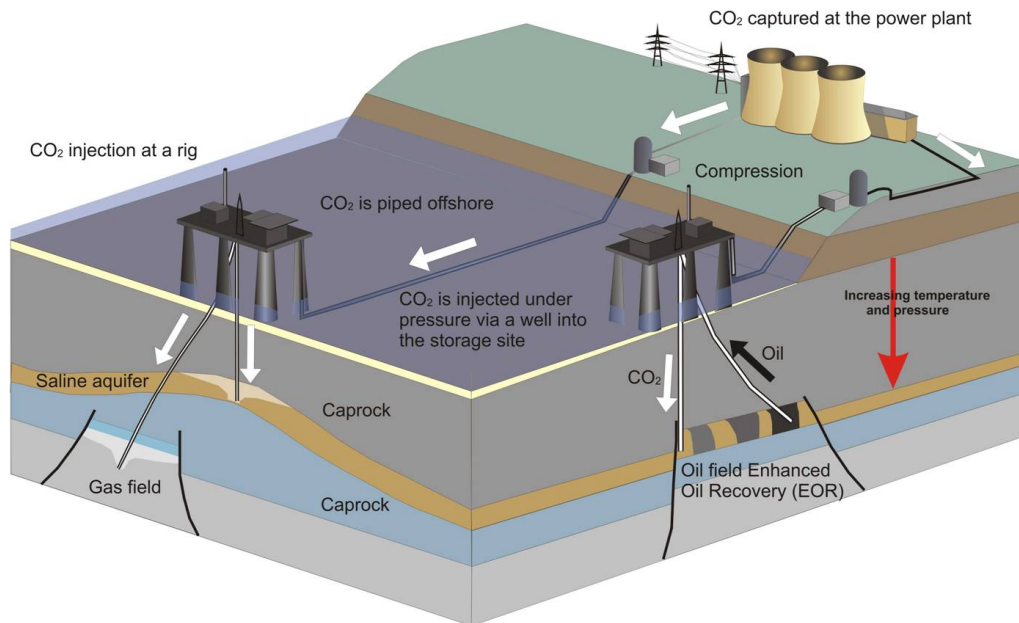


Fig. 1.5 Schematic showing elements of CCS infrastructure[8]

1.1.3 Situation of offshore pipelines

The history of natural gas pipelines and the situation of offshore pipelines in Japan and overseas are briefly introduced below[9, 10, 11].

1.1.3.1 Offshore pipelines in America and Europe

Laying onshore pipelines in America in the 1920s, an onshore pipeline with the length of 1,600km linking Texas to Chicago was constructed in 1931. In Europe, construction of small-scale onshore pipelines started in the early 1940s, and an onshore pipeline with the lengths of 788km was laid in Russia. In the 1960s, construction of a widespread pipeline grid for transporting natural gas in Groningen gas field into European countries started. Since then, pipelines has been not only a key of energy policy but also a key of diplomacy in America and Europe. Now, there is a dense and widespread pipeline grid in Europe, see Fig. 1.6.

On the other hand, construction of large-scale offshore pipelines started when development of the North Sea gas field started. Although North Sea gas field was found in the 1970s, laying offshore pipelines was accelerated in the 1990s due to the need of high technologies regarding both of production and transportation. Since then, many offshore pipelines linking Africa, Russia and West Asia to European countries has been constructed.

The longest offshore pipeline is Nord Stream with the lengths of 1,222km, linking Russia to Germany through the Baltic sea, see Fig. 1.7. Construction started 5 years after the agreement between Russia and Germany, then was successfully completed in 2012. On the other hand, constructions of offshore pipelines laid with water depths exceeding 1,000m have been expanding recently. Medgaz is offshore pipelines with maximum water depths of 2,160m, linking Algeria to Spain, and is now under operation. South stream is planned offshore pipelines linking Russia to Bulgaria through the Black Sea, and the maximum water depths is supposed to be 2,250m.

Fig. 1.8 shows 197 offshore pipeline projects from 1966 to 2012 including projects under construction as length versus depth graph, which were laid by Saipem's pipelaying vessels[11]. Solid marks represent the projects of more than 25 inches pipeline, and open marks are for the projects of less than 25 inches pipeline diameter. Circle marks represent the projects completed after 1995, and triangular marks for the projects completed before 1995. It is clearly seen that almost offshore pipelines in the deep water depth of greater than 1,000m were constructed using less than 25inch diameter pipes after 1995.

Pipelines are laid using pipelaying vessels, see Fig. 1.9[12]. Pipes are welded, coated and examined on the pipelaying vessel, then installed into the sea as the vessel moves forward. There are two major installation methods: conventional S-lay method and newer J-lay method, see Fig. 1.10[11]. J-lay method reduces the stress imposed on the pipelines, and is a better choice for the installation in deep waters, in excess of 2,000m.

1.1.3.2 Offshore pipelines in Japan

In Japan, the construction of a pipeline transporting natural gas of a gas field in Niigata Prefecture to the prefecture started in the 1960s. Since then, a large-scale pipeline with the lengths of 330km, which is referred to as Tokyo pipeline, was laid, linking Niigata Prefecture to Tokyo. In



Fig. 1.6 Pipeline grids in Europe[13]



Fig. 1.7 The route of the Nord Stream[14]

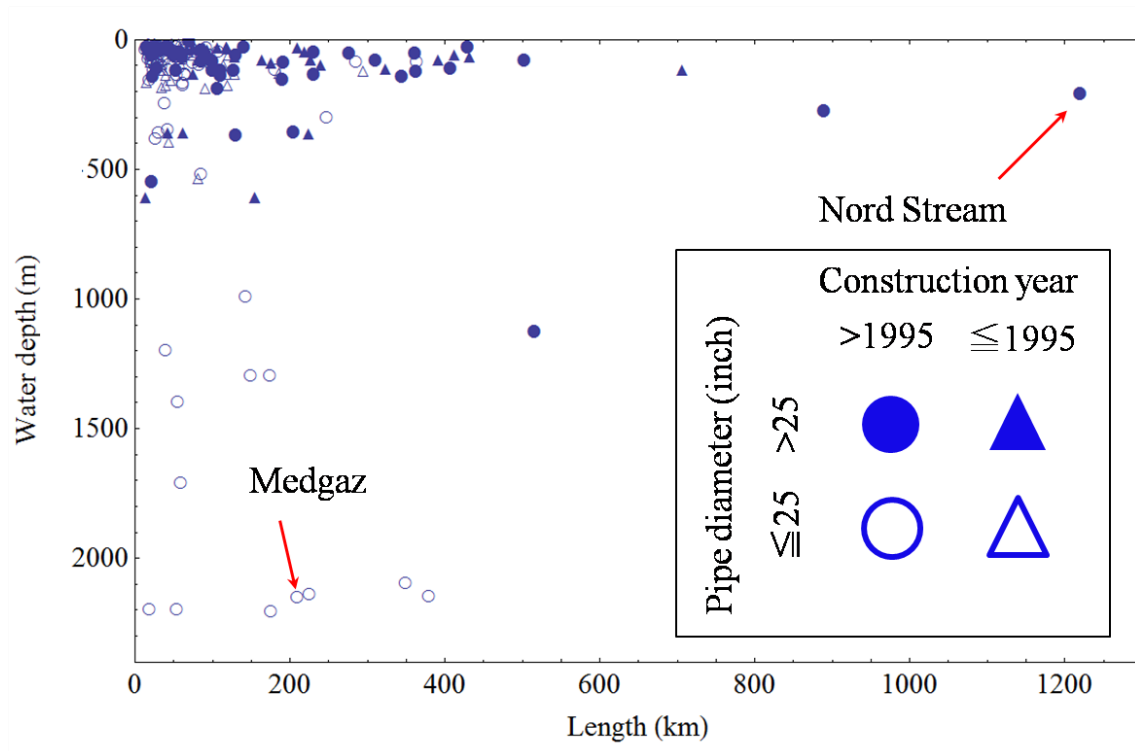


Fig. 1.8 Offshore pipeline projects from 1966 to 2012 including projects under construction, showing depth and length of each project(edited from [11])

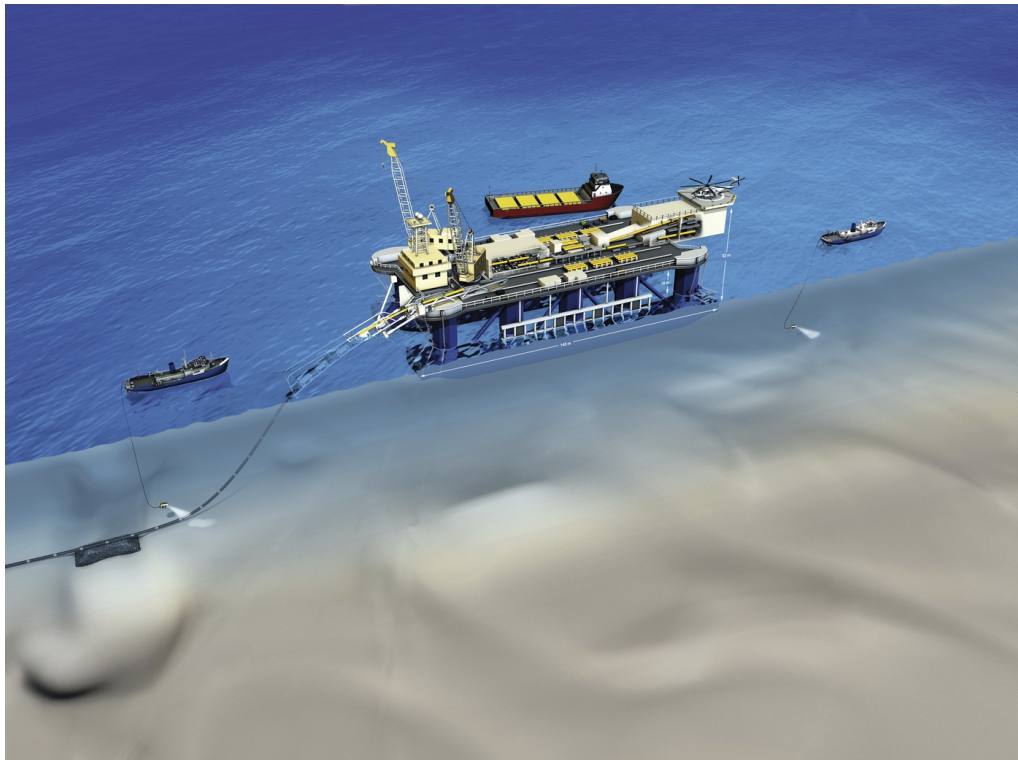


Fig. 1.9 Pipelay vessel Castoro Sei[12]

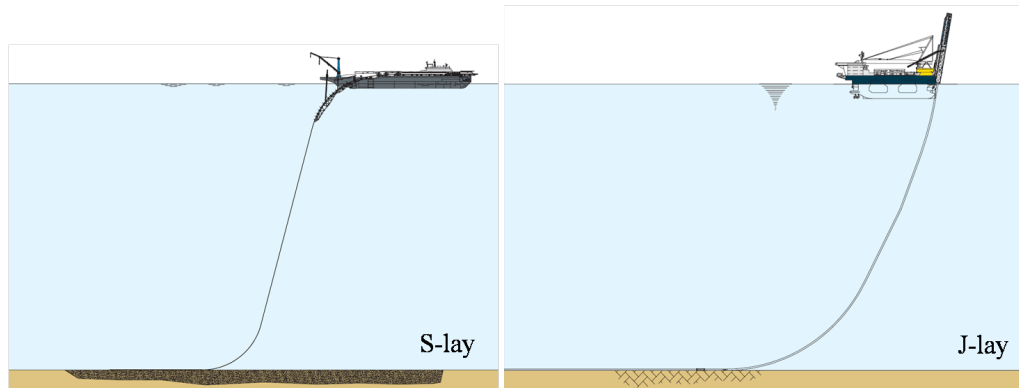


Fig. 1.10 Pipe installation methods: S-lay and J-lay[11]

the 1980s, small-scale pipeline grids within prefectures were constructed around LNG receiving terminals. The Tohoku natural gas pipeline with the lengths of 261km, linking the LNG receiving terminal in Niigata Prefecture to Sendai Prefecture, was completed in 1996.

On the other hand, there is no large-scale offshore pipeline in Japan. In the early 2000s, Sakhalin pipeline project, which transports natural gas in Sakhalin, Russia to Japanese major cities such as Tokyo by offshore pipelines, was under review, see Fig. 1.11[15]. However, the project failed not only because there is no standard for offshore pipeline design but also because power and gas industry stick to the transportation by liquefied natural gas carriers. Also, the offshore pipeline project, linking the LNG terminal in Niigata Prefecture to Iwaki City, Fukushima Prefecture via Sendai Prefecture, failed in 2008 due to increasing price of steels although some demonstration experiments were conducted to propose design standard.

However, the needs for large-scale offshore pipelines are now being reviewed because drastic increase of the demand of natural gas is anticipated as a substitution for nuclear power after the Fukushima nuclear accident in 2011. In 2013, Tokyo Gas officially announced the construction of an offshore pipeline linking Hitachi to Kashima in Ibaraki Prefecture, which is expected to be completed by 2015.

1.1.4 Fracture in pipelines

1.1.4.1 Fracture types

There are generally four types of fractures in pipelines. Characteristics of each type are briefly described below.

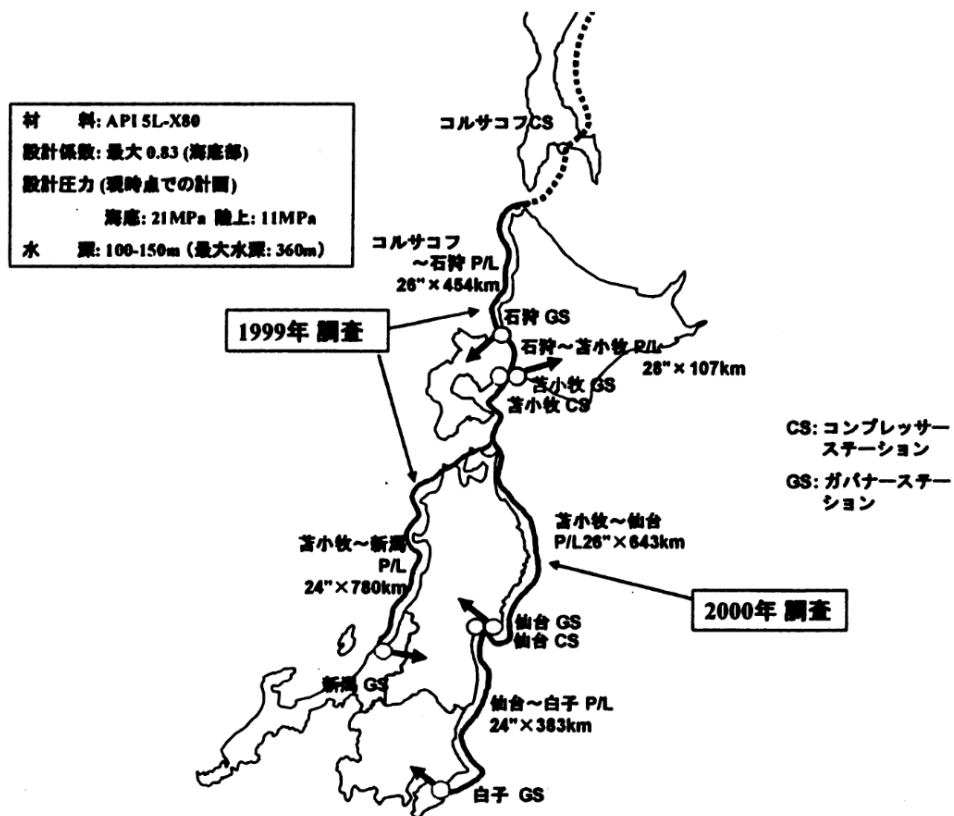


Fig. 1.11 Sakhalin project in Japan[15]

- Unstable ductile fracture

The present study focuses on this fracture type. A crack propagates with the velocity of less than 400m/s, and generates large plastic deformation ahead of a crack tip. If a crack velocity is equal to gas decompression velocity, a crack becomes unstable and might result in crucial accidents. The safety design for the fracture is usually determined by Charpy absorbed energy.

- Brittle fracture

A crack is initiated at lower temperature, and propagates with the velocity of about 400 to 1,000m/s. Small plastic deformation is exhibited ahead of a crack tip. The safety design for the fracture is determined by shear area fraction in the drop weight tear tests or Charpy impact tests.

- Fatigue fracture

A fatigue crack is initiated and grows by fluctuating internal pressure of a pipe. A fatigue crack with a particular length might lead occurrences of unstable ductile crack and brittle crack. For preventing this fracture, avoiding pressure fluctuation is crucially important.

- Stress corrosion cracking

A crack, which is subjected to tensile stress in a corrosive environment, grows unexpectedly. The crack might lead occurrences of unstable ductile crack and brittle crack. Pipe coating and cathodic protection are one of the methods for preventing stress corrosion cracking.

1.1.4.2 Unstable ductile fracture

The present study focuses on the unstable ductile fracture. The unstable ductile crack propagation occurs at higher temperature at which almost existing pipelines are now operated, and its velocity is usually smaller than 400 m/s which is comparable to gas decompression velocity. The crack is described as a competition between crack velocity and gas decompression velocity; if the two velocities are the same, constant pressure at a crack tip is kept as shown in Fig. 1.12, which leads pipeline fracture by unstable crack propagation, see Fig. 1.13. Therefore, investigations on the unstable crack propagation in pipelines have been conducted focusing on the two velocities. Previous studies are introduced in the next section.

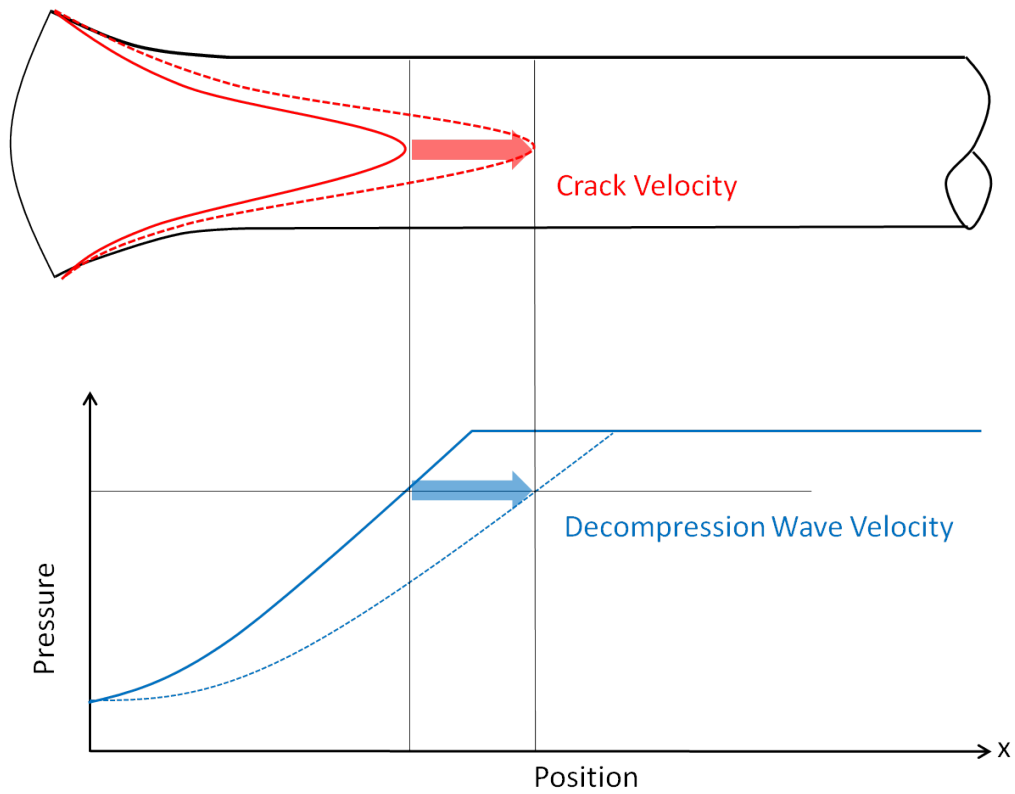


Fig. 1.12 Mechanism of unstable ductile crack propagation



Fig. 1.13 Photo of unstable ductile crack propagation[16]

1.2 Previous studies on unstable ductile fracture

Previous studies regarding unstable ductile crack propagation/arrest are briefly explained below.

1.2.1 Methods for evaluating unstable ductile crack propagation

1.2.1.1 Battelle Two-Curve method

It had been a mystery why ductile crack propagates long unsteadily although crack velocity is smaller than decompression velocity at initial pressure. In 1960s and 1970s, Battelle Memorial Institute conducted a series of full-scale burst tests on natural gas pipe and proposed the Battelle Two-Curve (BTC) method that has been most widely used in pipeline industry[17]. In the method, crack resistance curve, which is regarded as fracture velocity curve dependent on pressure at a crack tip, and gas decompression curve, which is regarded as decompression velocity curve dependent on pressure, are compared: unstable ductile crack is judged to occur if the two curves have intersections, if not, the crack is judged to decelerate rapidly and be arrested, see Fig. 1.14. The two curves are considered independently, which means that the interaction between crack propagation and gas decompression is neglected. Moreover, the equation for crack resistance curve was determined empirically based on the experimental data of the full-scale burst tests. Meanwhile, Mimura pointed out that because both decompression velocity and crack velocity decrease with decreasing pressure at a crack tip, comparison between both velocities leads to the evaluation for unstable ductile crack propagation/arrest[18].

1.2.1.2 HLP method

In Japan, HLP committee which consists of Japanese major steel companies started to investigate unstable ductile fracture since 1978 and conducted a series of full-scale burst tests on controlled rolled X70 pipe[19, 20, 21]. Meanwhile, HLP committee proposed the HLP method that is based on the BTC method and improved by incremental formulation which enables calculation for the history of crack length and velocity[22]. In the HLP method, the empirical equation for crack resistance curve was somewhat modified from that of BTC method based on the data of the full-scale burst tests on X70 pipes. Makino et al. proposed a modified HLP method

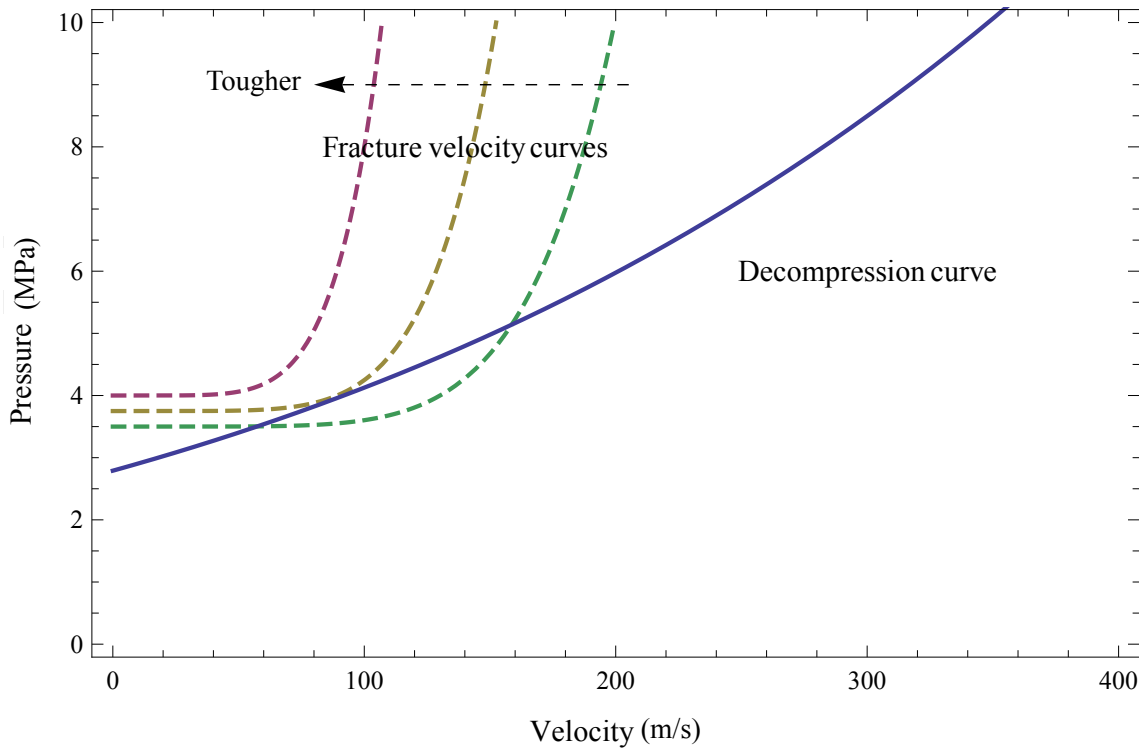


Fig. 1.14 Battelle two-curve method

by changing parameters of the equation of crack resistance curve in order to extend applicability of the method to higher grade pipe, X100[23, 24].

1.2.1.3 Finite element based model and other models

The BTC method and the HLP method have the same problem that the interaction between crack propagation and gas decompression is neglected and the empirical equation for crack resistance curve is determined based on limited data of full-scale burst tests. To overcome these disadvantages, some physically-based model was proposed. Emery et al. proposed the numerical model with the assumption that a pipe is an assembly of rings and crack propagation is regarded as cutting of the rings[25]. O'Donoghue et.al. first proposed a finite element based model where gas flow, pipe deformation and crack propagation are coupled and the judgement for crack propagation/arrest is done by crack tip opening angle (CTOA)[26]. In Japan, Yoshimura et al. developed one-way coupled 3D finite element simulation model, where the interaction among pipe deformation and gas decompression is not considered[27]. Although some full finite element based models were proposed[28, 29], they inevitably consume long CPU

time and require arbitrary parameters, e.g. critical CTOA.

Therefore, numerical models that are not based on 3D finite element model have been proposed. One of these is 1D finite difference based model developed by Misawa et al. , where the interaction between pipe deformation, gas decompression and crack propagation is incorporated[30]. The model is called the UT model. Pipe deformation is described by using a single shape parameter based on the Freund model[31], and gas flow is assumed to be one-dimensional flow where gas leakage from crack opening is considered. Crack propagation criterion is based on dynamic energy balance considering accumulated plastic strain energy, kinetic energy of pipe wall movement, work done by gas on pipe wall and resistance for crack propagation dependent on crack velocity. Because the model is achieved by simple formulation and solved by finite difference method, it consumes shorter CPU time as compared to 3D FE based models.

The UT model incorporates the soil backfill effect as an added mass effect. The author reformulated the soil backfill effect together with some improvements on gas decompression and pipe deformation modeling, then applied to the full-scale natural gas pipeline burst tests[32]. Figure 1.15 shows an example of the calculated results with experimental results shown by blue arrows, where there are generally good agreements between the calculated and experimental results for the cases with and without soil backfill. Figure 1.16 shows the dependence of soil backfill depth on unstable crack propagation; increasing soil backfill depth makes a crack more likely to be arrested.

1.2.2 Methods for offshore pipelines

There is no established method for unstable ductile fracture in offshore pipelines. W. A. Maxey surveyed offshore pipeline burst tests conducted ever, and proposed the modified crack resistance curve in BTC method for offshore pipelines[33], see Fig. 1.17 and Fig. 1.18. However, the applicability of the modified curve is definitely limited because there were only four full-scale offshore pipeline burst tests, which is not enough to propose an empirical method. Also, Inoue incorporated dynamic external pressure changes, which is generated by rapid bubble growth at pipe burst underwater, into the HLP method, and calculated unstable crack propagation in offshore pipelines[34]. However, dynamic pressure changes was formu-

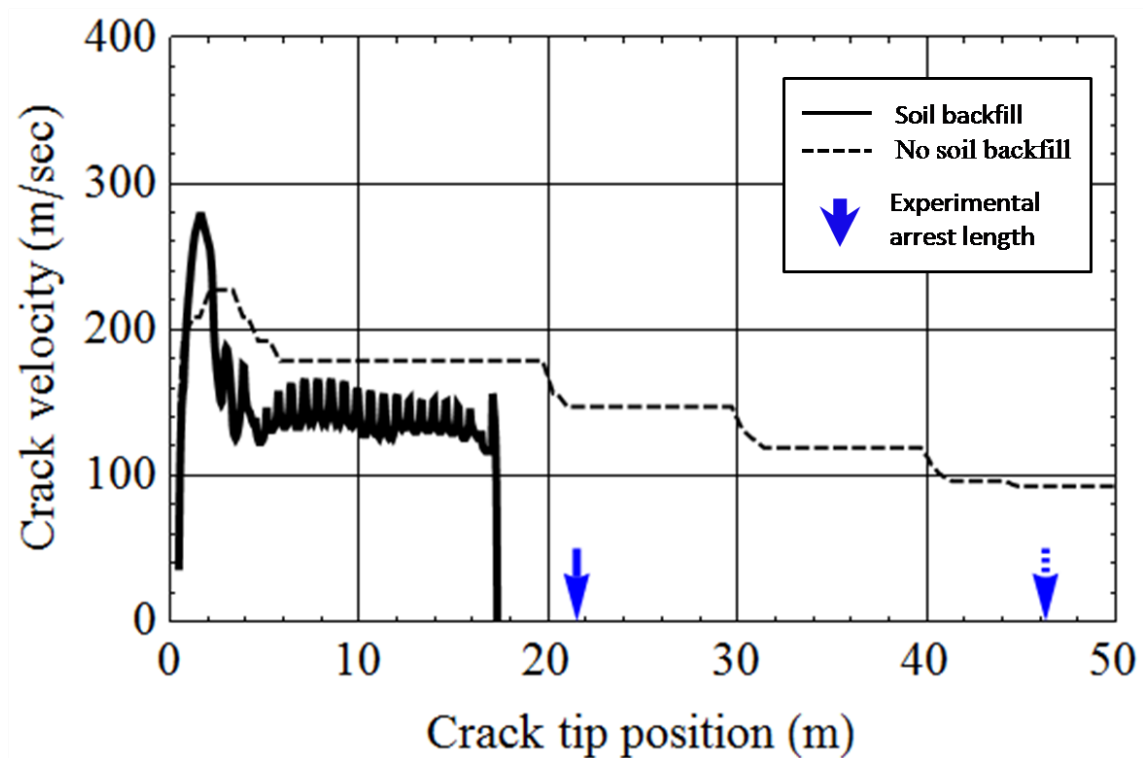


Fig. 1.15 An example calculated result for the full-scale natural gas pipeline burst tests with and without soil backfill[32]

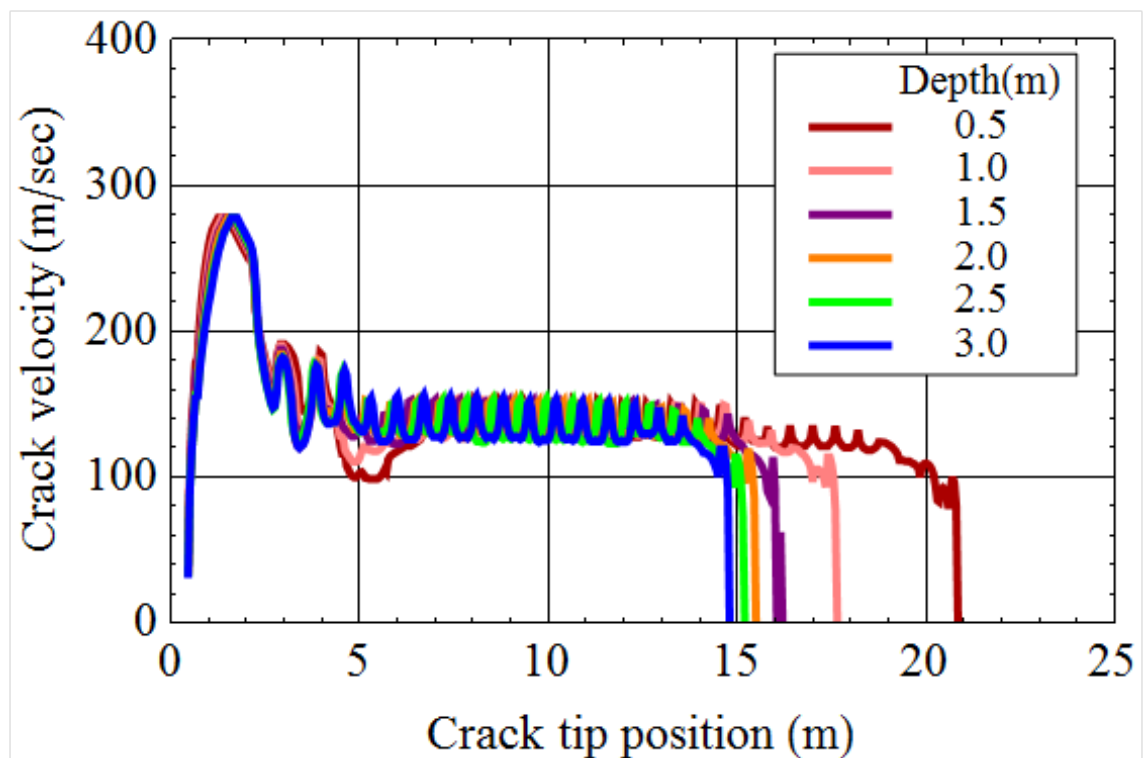


Fig. 1.16 The effect of soil backfill depth on unstable ductile crack propagation[32]

lated based on the limited data of full-scale offshore pipeline burst tests.

In addition, there is no FE based or other model, where coupling phenomenon among gas decompression, bubble growth, pipe deformation and crack propagation are incorporated. Therefore, coupled numerical model without empirical parameters is necessary for the safety design against unstable ductile crack propagation in offshore pipelines.

The author developed simplified bubble growth model in master's thesis[35], where a crack propagation is not considered and the bubble is assumed to be sphere. The author clarified that gas decompression delays due to the bubble generation/growth underwater as compared with gas decompression in onshore pipelines.

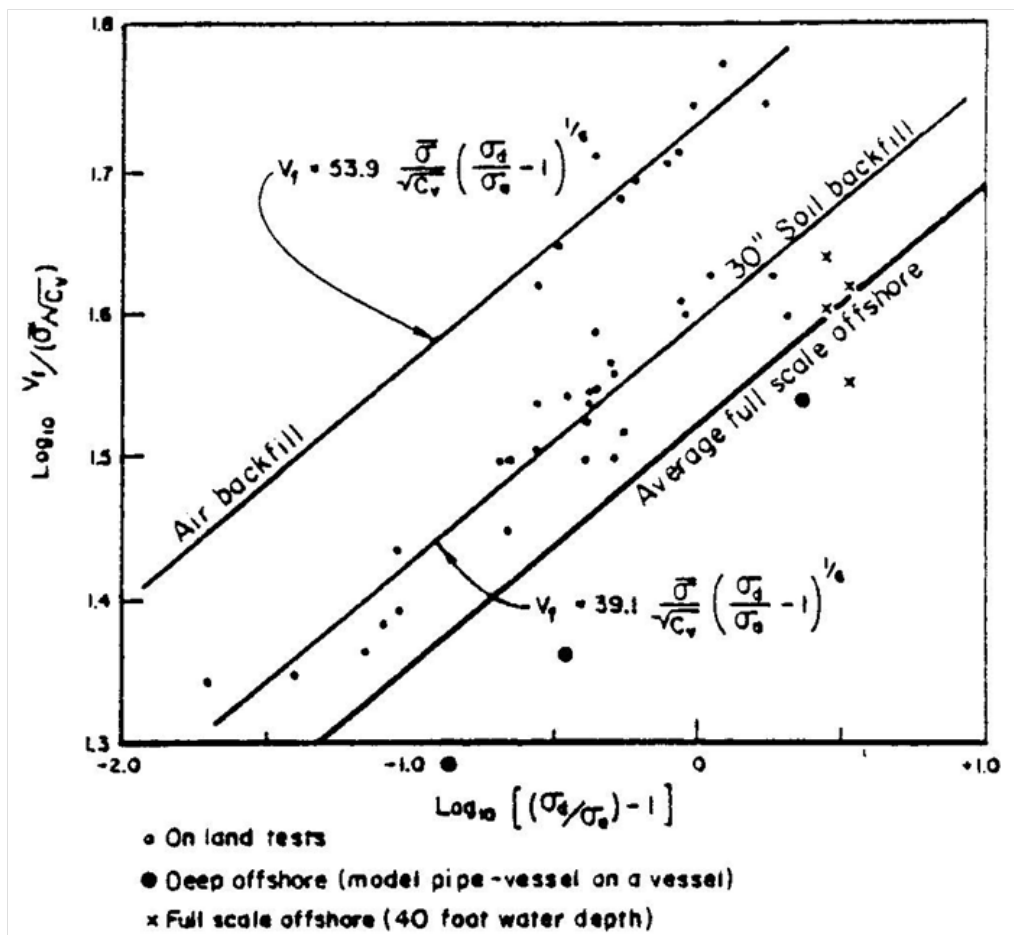


Fig. 1.17 Ductile fracture correlations between air, sand and water backfill[33]

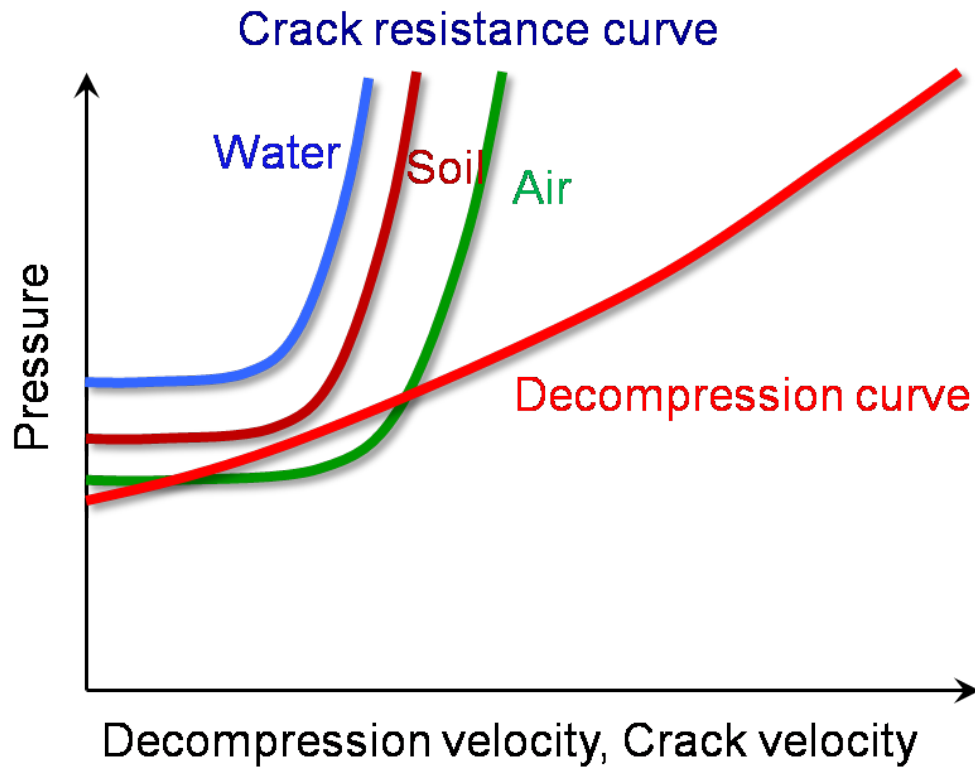


Fig. 1.18 Dependence of kinds of backfill on crack resistance curve in BTC

1.2.3 Existing full-scale offshore pipeline burst tests

There are only four published full-scale offshore pipeline burst tests conducted by C.S.M and Battelle Memorial Institute in the late 1980s[33, 36], see Fig. 1.19. The reasons for few number of the tests are that testing cost is so high and high-tech equipments are required. Although the data obtained from the tests are valuable, the amount of the data is not enough to discuss the effects of parameters such as water depth, pipe geometry and kinds of gas on unstable ductile fracture behavior. For example, the test performed by C.S.M was conducted in water depth of 30m, which is far shallower than water depth of several thousand meters where existing offshore pipelines are now in operation.

Due to the difficulties of full-scale offshore pipeline burst tests, there is no doubt that the development of a numerical model which is able to discuss parameters such as water depth is strongly necessary.

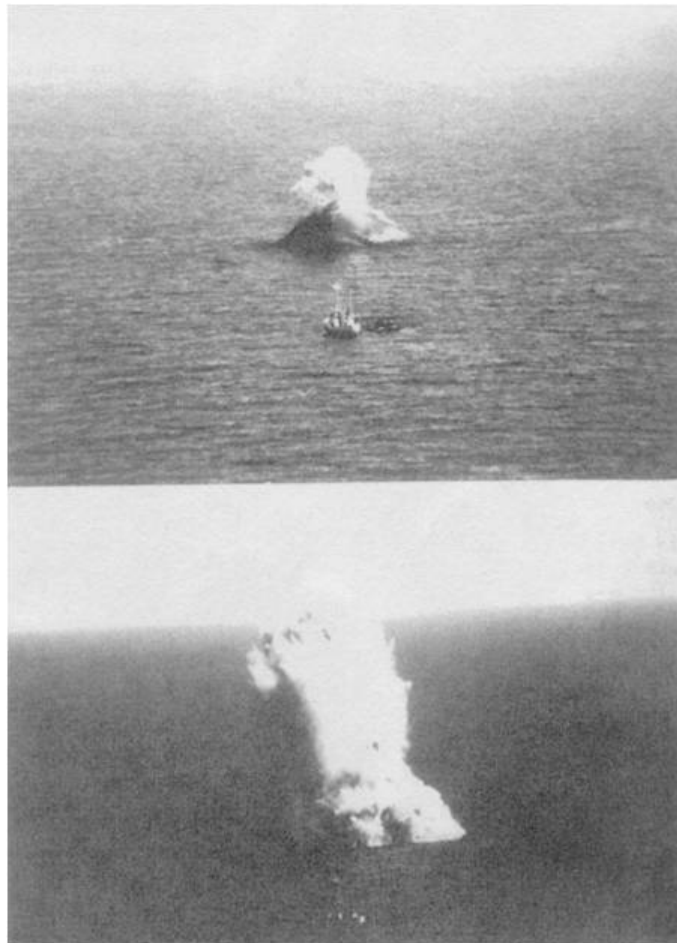


Fig. 1.19 A photo of full-scale offshore pipeline burst test[36]

1.3 Objectives of the present study

In the present study, the author developed a numerical model, which is called "UT offshore model" hereafter, to predict unstable ductile crack propagation/arrest in offshore pipelines. As the name suggests, the UT offshore model is based on the UT model, and improved so that it can be applied to offshore pipelines. The features of the model are as follows:

- water effects such as delayed gas decompression by bubble generation/growth and constrained pipe deformation by surrounding water are incorporated in the model.
- pipe deformation, gas decompression and bubble growth are formulated based on one-dimensional partial differential equations which are solved by finite difference method.
- the interaction among pipe deformation, gas decompression, bubble growth and crack propagation is considered.
- the model has a potential as an engineering tool for offshore pipeline design due to its low CPU cost as compared with three-dimensional finite element based models.

The author also conducted underwater rupture tests especially to validate the bubble growth model in the UT offshore model by observing bubble growth behavior using high-speed camera. In addition, the model is applied to the published full-scale offshore pipeline burst test. Also, parametric studies were conducted using the UT offshore model to clarify the effects of the parameters such as water depth and pipe geometry on the behavior of unstable ductile fracture in offshore pipelines,

1.4 Structure of the thesis

The present thesis consists of seven chapters.

- Chapter 2 introduces basic theories related to the present study.
- Chapter 3 describes the detail of the UT offshore model.
- Chapter 4 explains underwater rupture tests and presents calculation results for the validation of bubble growth model.
- Chapter 5 presents calculation results for the full-scale offshore pipeline

burst tests.

- Chapter 6 introduces results of parametric studies and discusses the effects of water depth, pipe geometry and mechanical properties on the behavior of unstable ductile crack in offshore pipelines.
- Chapter 7 describes the conclusions and future works of the present study.

Chapter 2

Basic theories

The present chapter introduces basic theories related to the present study.

2.1 Compressible fluid mechanics

The theories of compressible fluid mechanics is presented below[37][38][39].

2.1.1 State equation

If pressure p , density ρ and temperature T are given, the state equation for the ideal gas is as follows;

$$p = \rho RT \quad (2.1)$$

where, R is specific gas constant which is referred to as a value of gas constant divided by molecular weight of a gas.

2.1.2 Mass conservation in one-dimensional flow

Suppose for one-dimensional compressible gas flow inside a pipe with cross sectional area A , pressure p , density ρ and flow rate u , where viscosity is neglected, see Fig. 2.1. Mass conservation inside a cross sectional volume with thickness of δx during infinitesimal time δt leads to the following equation;

$$\begin{aligned} (\rho u A) \delta t &= \frac{\partial(\rho A \delta x)}{\partial t} \delta t + \left[\rho u A + \frac{\partial(\rho u A)}{\partial x} \right] \delta t \\ \therefore \frac{\partial(\rho A)}{\partial t} + \frac{\partial(\rho u A)}{\partial x} &= 0 \end{aligned} \quad (2.2)$$

This equation is the equation for mass conservation.

2.1.3 Momentum conservation in one-dimensional flow

Suppose for one-dimensional compressible gas flow inside a pipe with cross sectional area A , pressure p , density ρ and flow rate u as well as mass conservation, see Fig. 2.2. By considering impulse by pressure and momentum of fluid, momentum conservation inside a cross sectional volume with thickness of δx during infinitesimal time δt leads to the following equation;

$$\begin{aligned} \frac{\partial(\rho u A \delta x)}{\partial t} \delta t &= p A \delta t + \left(p + \frac{\partial p}{\partial x} \frac{\delta x}{2} \right) \frac{\partial A}{\partial x} \delta t \delta x - \left[p A \delta t + \frac{\partial(p A \delta t)}{\partial x} \delta x \right] \\ &\quad + \rho u^2 A \delta t - \left[\rho u^2 A \delta t + \frac{\partial(\rho u^2 A \delta t)}{\partial x} \delta x \right] \\ \therefore \frac{\partial(\rho u A)}{\partial t} + \frac{\partial(\rho u^2 A)}{\partial x} &= -A \frac{\partial p}{\partial x} \end{aligned} \quad (2.3)$$

This equation is the equation for momentum conservation.

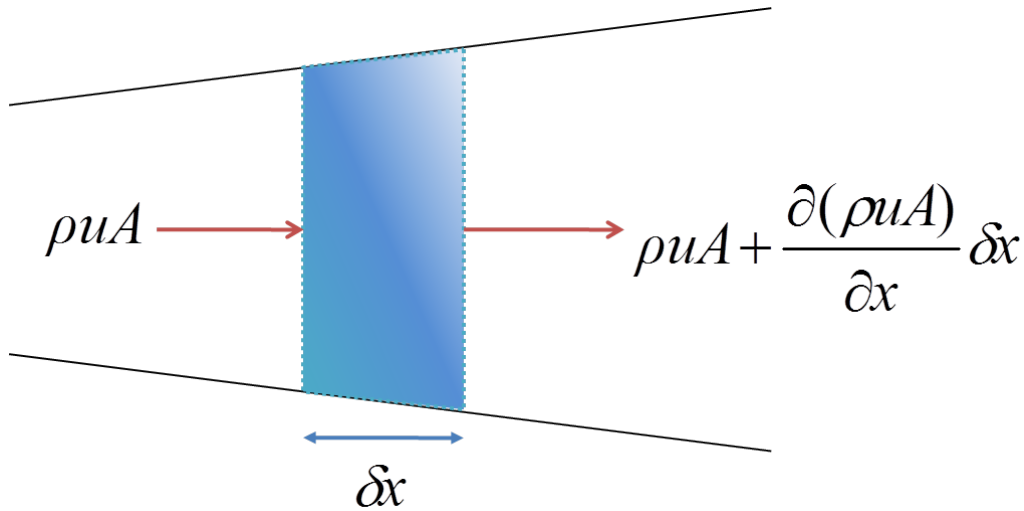


Fig. 2.1 Mass conservation in one-dimensional compressible gas flow

2.1.4 Energy conservation law(isentropic process)

If adiabatic and reversible change of gas is assumed, entropy inside the system is kept constant. For the ideal gas, the relationship between pressure p

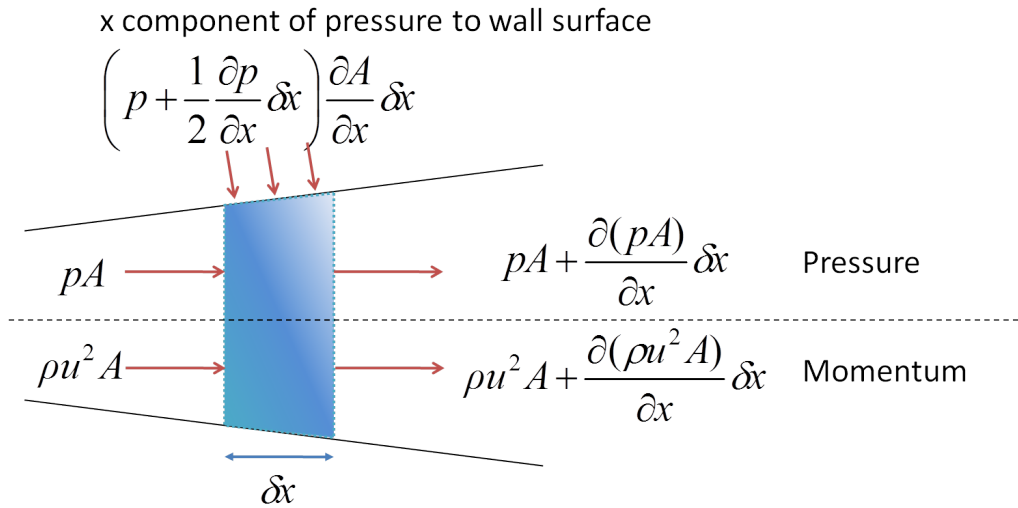


Fig. 2.2 Momentum conservation in one-dimensional compressible gas flow

and density ρ under adiabatic change is given by

$$p\rho^{-\gamma} = \text{const} \quad (2.4)$$

where γ is specific heat ratio. Eq. (2.4) can be rewritten using the state equation of (2.1);

$$pT^{-\frac{\gamma}{\gamma-1}} = \text{const} \quad (2.5)$$

Use of Eq. (2.4) and Eq. (2.5) leads to the relationship under isentropic change as follows;

$$\rho = \rho_0 \left(\frac{p}{p_0} \right)^{\frac{1}{\gamma}} \quad (2.6)$$

$$T = T_0 \left(\frac{p}{p_0} \right)^{\frac{\gamma-1}{\gamma}} \quad (2.7)$$

where p_0 and ρ_0 is pressure and density at an initial condition, respectively. If isentropic change is assumed, general relationships between pressure p , density ρ and temperature T are expressed as follows, irrespective of whether the gas is ideal or not;

$$\rho = \rho(p) \quad (2.8)$$

$$T = T(p) \quad (2.9)$$

2.1.5 Acoustic velocity

If cross sectional area A is constant and changes in flow rate u is neglected in one-dimensional flow, Eq. (2.2) and Eq. (2.3) can be rewritten as follows;

$$\frac{\partial \rho}{\partial t} + \frac{\partial(\rho u)}{\partial x} = 0 \quad (2.10)$$

$$\frac{\partial(\rho u)}{\partial t} = -\frac{\partial p}{\partial x} \quad (2.11)$$

In addition, an assumption of isentropic change, where pressure p is a function of density ρ , leads to the following equation;

$$\frac{\partial p}{\partial x} = \frac{dp}{d\rho} \frac{\partial \rho}{\partial x} \quad (2.12)$$

Equation (2.10), Eq. (2.11) and Eq. (2.12) lead to the partial differential equation in terms of density ρ as follows;

$$\frac{\partial^2 \rho}{\partial t^2} = \frac{dp}{d\rho} \frac{\partial^2 \rho}{\partial x^2} \quad (2.13)$$

This is the equation of wave motion. Because the velocity of density wave represents the velocity of acoustic wave, the acoustic velocity is expressed as;

$$a = \sqrt{\frac{dp}{d\rho}} \quad (2.14)$$

2.1.6 Choked flow

Suppose for compressible gas inside a substantially large tank with pressure p_0 , flow rate $u_0 = 0$, density ρ_0 and temperature T_0 , and the gas is flowing out through a hole with cross sectional area of A , see Fig. 2.3.

If cross sectional area A is constant and the flow is steady, Bernouli's law leads to the following equation;

$$\frac{u^2}{2} + \int \frac{dp}{\rho} = const \quad (2.15)$$

By considering initial conditions, the above equation is rewritten as follows;

$$\frac{u^2}{2} + \int_0^p \frac{dp}{\rho} = \int_0^{p_0} \frac{dp}{\rho}$$

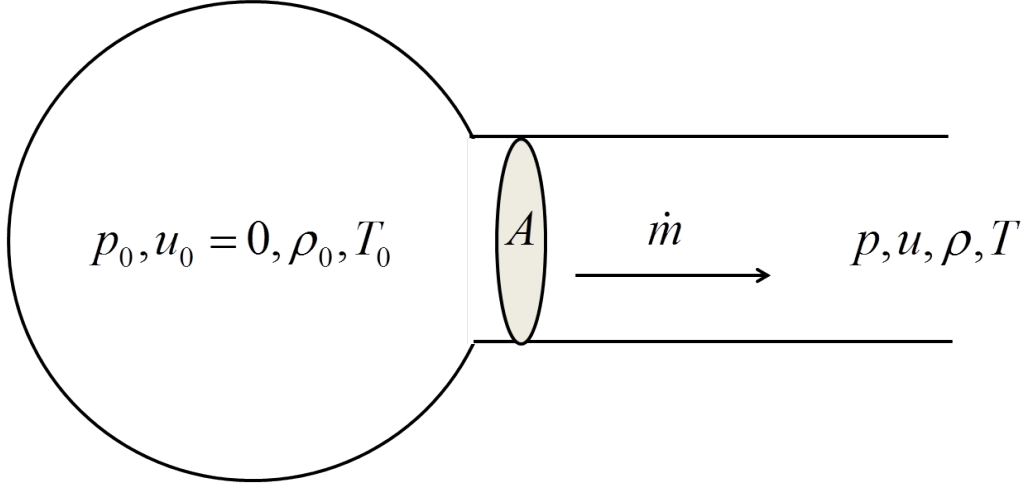


Fig. 2.3 One-dimensional choked flow

$$\therefore u = \sqrt{2 \int_p^{p_0} \frac{dp}{\rho}} \quad (2.16)$$

Mass flow rate \dot{m} is expressed as;

$$\dot{m} = \rho u A = \rho A \sqrt{2 \int_p^{p_0} \frac{dp}{\rho}} \quad (2.17)$$

Moreover, if the ideal gas changes its state under isentropic change, substituting Eq. (2.1) and Eq. (2.8) into Eq. (2.17) leads to the following equation;

$$\begin{aligned} \dot{m} &= A \rho_0 \left(\frac{p}{p_0} \right)^{\frac{1}{\gamma}} \sqrt{2 \int_p^{p_0} \frac{1}{\rho_0} \left(\frac{p}{p_0} \right)^{-\frac{1}{\gamma}} dp} \\ &= A \rho_0 \left(\frac{p}{p_0} \right)^{\frac{1}{\gamma}} \sqrt{\frac{2\gamma}{\gamma-1} \frac{p_0}{\rho_0} \left[1 - \left(\frac{p}{p_0} \right)^{\frac{\gamma-1}{\gamma}} \right]} \\ &= \frac{p_0 A}{\sqrt{RT_0}} \sqrt{\frac{2\gamma}{\gamma-1} \left[\left(\frac{p}{p_0} \right)^{\frac{2}{\gamma}} - \left(\frac{p}{p_0} \right)^{\frac{\gamma+1}{\gamma}} \right]} \end{aligned} \quad (2.18)$$

When the following equation hold, \dot{m} reaches the maximum value.

$$\frac{p}{p_0} = \left(\frac{2}{\gamma+1} \right)^{\frac{\gamma}{\gamma-1}} \quad (2.19)$$

The maximum value, where gas flow is said to be choked, is expressed as;

$$\dot{m}_{max} = \frac{p_0 A}{\sqrt{RT_0}} \sqrt{\gamma \left(\frac{2}{\gamma + 1} \right)^{\frac{\gamma+1}{\gamma-1}}} \quad (2.20)$$

Because the maximum value of mass flow rate is proportional to cross sectional area A and determined by pressure p_0 and temperature T_0 at the initial condition, the maximum value of mass flow rate for the actual gas is generally expressed as;

$$\dot{m}_{max} = A \dot{m}(p_0, T_0) \quad (2.21)$$

2.2 Bubble growth equation

Formulation of the bubble growth is explained in the present section[40]. Suppose for a spherical bubble surrounded by non-compressible liquid, see Fig. 2.4. $R(t)$ is bubble radius, and density and temperature substantially far from the bubble are $p_\infty(t)$ and T_∞ , respectively. T_∞ is assumed to be constant. In addition, it is assumed that density ρ_L and viscosity coefficient μ_L of the liquid are constant, and pressure p_B and temperature T_B inside the bubble are uniform.

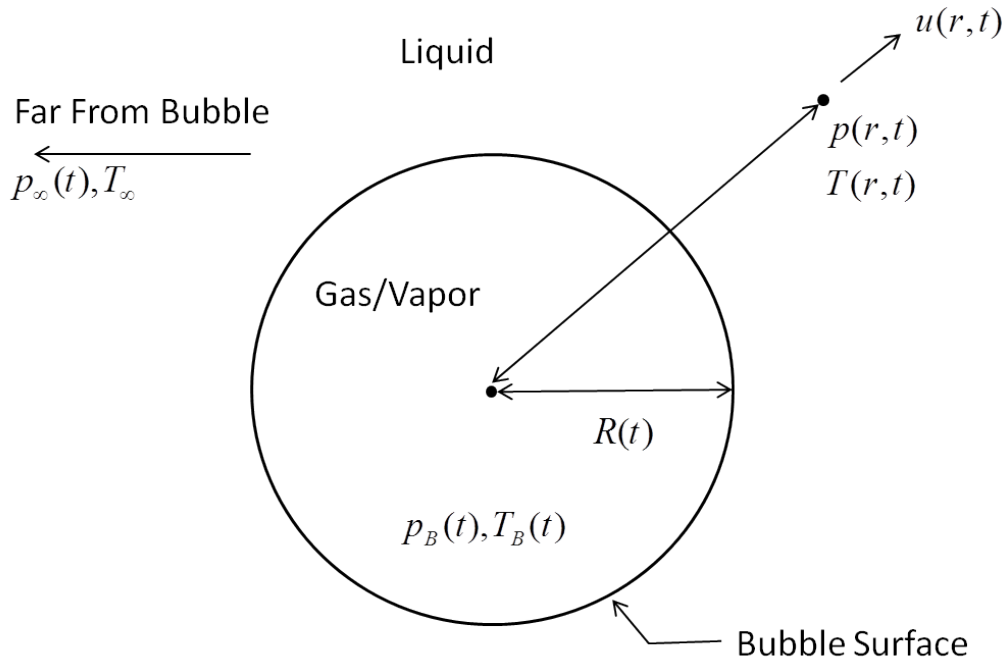


Fig. 2.4 A bubble in non-compressible liquid

Pressure $p(r, t)$, flow rate $u(r, t)$ and temperature $T(r, t)$ in the liquid are expressed as a function of distance from the bubble center r and time t . Mass conservation leads to the following equation;

$$u(r, t) = \frac{F(t)}{r^2} \quad (2.22)$$

If no mass transfer through the bubble surface is assumed, $u(R, t) = dR/dt$ holds. Therefore, $F(t)$ is given by;

$$F(t) = R^2 \frac{dR}{dt} \quad (2.23)$$

Even if mass transfer by evaporation and condensation happens, Eq. (2.23) gives good approximation. Suppose for a bubble with water vapor. Growth rate of volume of water vapor, which is equal to growth rate of volume of bubble, is expressed as $4\pi R^2 dR/dt$. Therefore, growth rate of mass of water vapor is given by $\rho_V(T_B)4\pi R^2 dR/dt$, where ρ_V is saturated density of water vapor. Because the growth rate of mass of water vapor is equal to mass flow rate coming into the bubble through the surface, it is expressed as $\rho_V(T_B)(dR/dt)/\rho_L$. From the above discussion, the following equation holds;

$$u(R, t) = \frac{dR}{dt} - \frac{\rho_V(T_B)}{\rho_L} \frac{dR}{dt} = \left[1 - \frac{\rho_V(T_B)}{\rho_L} \right] \frac{dR}{dt} \quad (2.24)$$

$$F(t) = \left[1 - \frac{\rho_V(T_B)}{\rho_L} \right] R^2 \frac{dR}{dt} \quad (2.25)$$

In practical cases, $\rho_V(T_B) \ll \rho_L$ holds. Therefore, Eq. (2.23) is proven to be good approximate equation. Eq. (2.23) is used in the discussion hereafter.

If Newtonian fluid is assumed, Navier-Stokes equation to the direction of r is given by;

$$-\frac{1}{\rho_L} \frac{\partial p}{\partial r} = \frac{\partial u}{\partial t} + u \frac{\partial u}{\partial r} - \nu_L \left[\frac{1}{r^2} \frac{\partial}{\partial r} \left(r^2 \frac{\partial u}{\partial r} \right) - \frac{2u}{r^2} \right] \quad (2.26)$$

Substituting $u = F(t)/r^2$ leads to the following equation;

$$-\frac{1}{\rho_L} \frac{\partial p}{\partial r} = \frac{1}{r^2} \frac{dF}{dt} - \frac{2F^2}{r^5} \quad (2.27)$$

where, the viscosity term is neglected because the contribution of viscosity is incorporated into the boundary condition explained below.

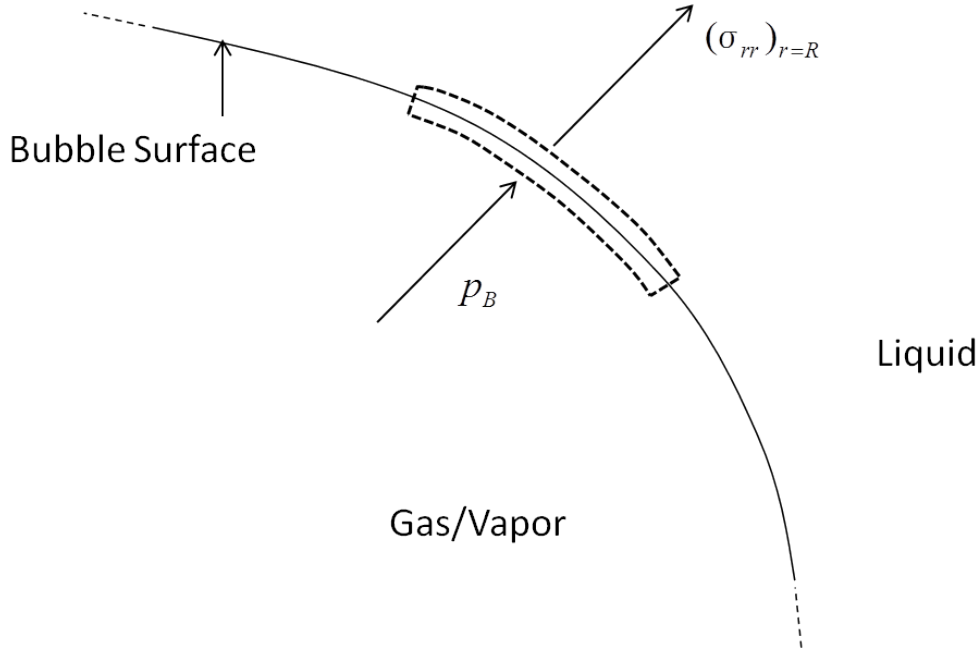


Fig. 2.5 Bubble surface

Because $p \rightarrow p_\infty$ when $r \rightarrow \infty$, integrating Eq. (2.27) leads to the following equation;

$$\frac{p - p_\infty}{\rho_L} = \frac{1}{r} \frac{dF}{dt} - \frac{1}{2} \frac{F^2}{r^4} \quad (2.28)$$

Finally, supposed for an infinitesimally thin film containing the bubble surface for derivation of the boundary condition, see Fig. 2.5. Net force per unit area acting on the film is expressed as;

$$(\sigma_{rr})_{r=R} + p_B - \frac{2S}{R} \quad (2.29)$$

Because $\sigma_{rr} = -p + 2\mu_L \partial u / \partial r$ holds, the net force per unit area is rewritten as;

$$p_B - (p)_{r=R} - \frac{4\nu_L}{R} \frac{dR}{dt} - \frac{2S}{R} \quad (2.30)$$

If there is no mass transfer by evaporation and condensation through the surface, the net force should be zero. Substituting $(p)_{r=R}$ of Eq. (2.30) into Eq. (2.28) leads to the Rayleigh-Plesset equation as follows;

$$\frac{p_B(t) - p_\infty(t)}{\rho_L} = R \frac{d^2 R}{dt^2} + \frac{3}{2} \left(\frac{dR}{dt} \right)^2 + \frac{4\nu_L}{R} \frac{dR}{dt} + \frac{2S}{\rho_L R} \quad (2.31)$$

2.3 Relationship between displacements and strains of a shell element in a thin cylinder under finite deformation

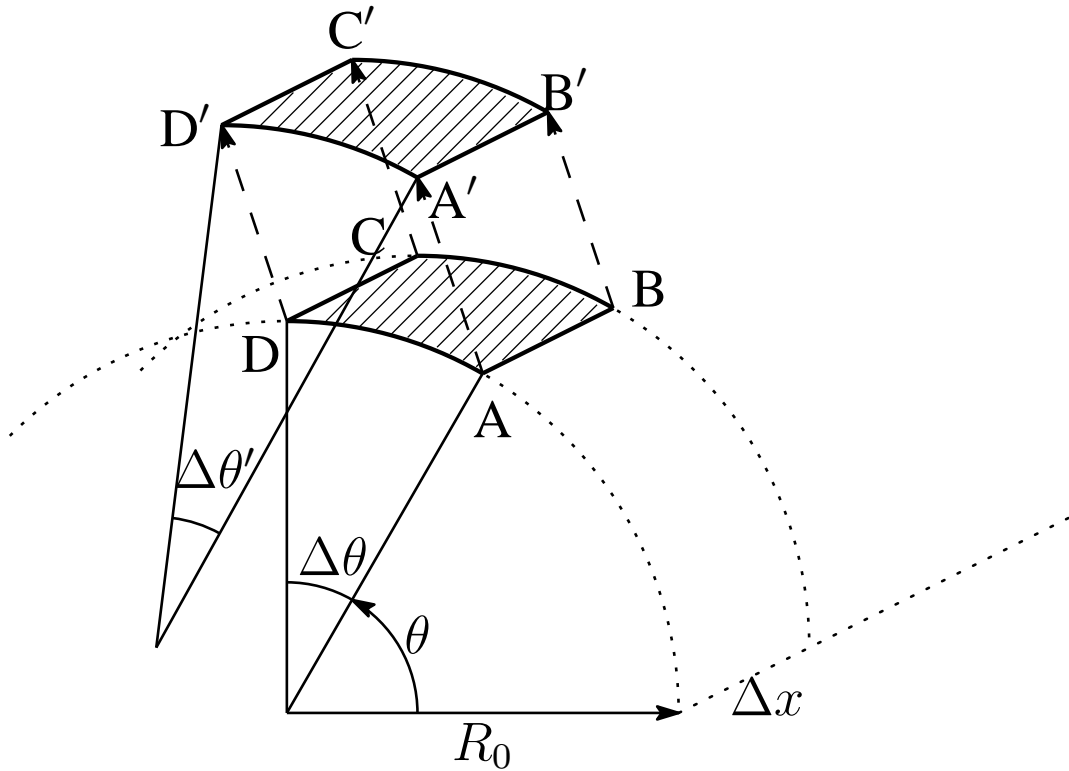


Fig. 2.6 Deformation of thin cylindrical shell element

The relationship between displacements and strains, which are generated by pipe deformation, is described below[41]. Suppose for an infinitesimal shell element deforms from $ABCD$ to $A'B'C'D'$, see Fig. 2.6. Cylindrical coordinates of point A, point B, point C and point D are given by;

$$A(x, \theta, R_0,) \quad (2.32)$$

$$B(x + \Delta x, \theta, R_0) \quad (2.33)$$

$$C(x + \Delta x, \theta + \Delta\theta, R_0) \quad (2.34)$$

$$D(x, \theta + \Delta\theta, R_0) \quad (2.35)$$

where, x , θ and r represent axial direction, circumferential direction and radial direction, respectively. After the deformation, coordinates of each

point is given by;

$$A' \left(x + u, \theta + \frac{v}{R_0}, R_0 + w \right) \quad (2.36)$$

$$B' \left(x + u + \frac{\partial u}{\partial x} \Delta x, \theta + \frac{v}{R_0} + \frac{1}{R_0} \frac{\partial v}{\partial x} \Delta x, R_0 + w + \frac{\partial w}{\partial x} \Delta x \right) \quad (2.37)$$

$$C' \left(x + u + \frac{\partial u}{\partial x} \Delta x + \frac{\partial u}{\partial \theta} \Delta \theta, \theta + \frac{v}{R_0} + \frac{1}{R_0} \frac{\partial v}{\partial x} \Delta x + \frac{1}{R_0} \frac{\partial v}{\partial \theta} \Delta \theta, R_0 + w + \frac{\partial w}{\partial x} \Delta x + \frac{\partial w}{\partial \theta} \Delta \theta \right) \quad (2.38)$$

$$D' \left(x + u + \frac{\partial u}{\partial \theta} \Delta \theta, \theta + \frac{v}{R_0} + \frac{1}{R_0} \frac{\partial v}{\partial \theta} \Delta \theta, R_0 + w + \frac{\partial w}{\partial \theta} \Delta \theta \right) \quad (2.39)$$

where, u , v and w represent axial displacement, circumferential displacement and radial displacement, respectively. In addition, higher order terms than the second order term are neglected. Axial strain, circumferential strain, engineering shear strain and change in circumferential curvature are expressed as follows;

$$\varepsilon_x = \lim_{\Delta x \rightarrow 0} \frac{A'B'}{AB} - 1 \quad (2.40)$$

$$\varepsilon_\theta = \lim_{\Delta \theta \rightarrow 0} \frac{A'D'}{AD} - 1 \quad (2.41)$$

$$\gamma_{x\theta} = \lim_{\Delta x \rightarrow 0} \lim_{\Delta \theta \rightarrow 0} \frac{\overrightarrow{A'D'} \cdot \overrightarrow{AD}}{R_0 \Delta x \Delta \theta} \quad (2.42)$$

$$\kappa_\theta = \lim_{\Delta \theta \rightarrow 0} \left[\frac{\Delta \theta'}{A'D'} - \frac{\Delta \theta}{AD} \right] \quad (2.43)$$

Geometric calculation leads to the following equation;

$$\Delta \theta' = \Delta \theta + \frac{1}{R_0} \frac{\partial v}{\partial \theta} + \frac{1}{R_0 + w} \frac{R_0}{R_0 + \frac{\partial v}{\partial \theta}} \frac{\partial w}{\partial \theta} - \frac{1}{R_0 + w + \frac{\partial w}{\partial \theta} \Delta \theta} \frac{R_0}{R_0 + \frac{\partial v}{\partial \theta} + \frac{\partial^2 v}{\partial \theta^2} \Delta \theta} \quad (2.44)$$

From the above discussions, the relationships between displacements and strains of a shell element in thin cylinder under finite deformation are given by;

$$\varepsilon_x = \sqrt{\left(\frac{\partial u}{\partial x} + 1 \right)^2 + \left(\frac{w}{R_0} + 1 \right)^2 \left(\frac{\partial v}{\partial x} \right)^2 + \left(\frac{\partial w}{\partial x} \right)^2} - 1 \quad (2.45)$$

$$\varepsilon_\theta = \sqrt{\left(\frac{w}{R_0} + 1\right)^2 \left(\frac{1}{R_0} \frac{\partial v}{\partial \theta} + 1\right)^2 + \left(\frac{1}{R_0} \frac{\partial u}{\partial \theta}\right)^2 + \left(\frac{1}{R_0} \frac{\partial w}{\partial \theta}\right)^2} - 1 \quad (2.46)$$

$$\gamma_{x\theta} = \left(\frac{w}{R_0} + 1\right)^2 \frac{\partial v}{\partial x} \left(\frac{1}{R_0} \frac{\partial v}{\partial \theta} + 1\right) + \frac{1}{R_0} \left(\frac{\partial u}{\partial x} + 1\right) \frac{\partial u}{\partial \theta} + \frac{1}{R_0} \frac{\partial w}{\partial x} \frac{\partial w}{\partial \theta} \quad (2.47)$$

$$\kappa_\theta = \frac{1}{R_0} \left[\left(1 + \frac{1}{R_0} \frac{\partial v}{\partial \theta}\right)^2 \left(1 + \frac{w}{R_0}\right)^2 + \left(\frac{1}{R_0} \frac{\partial u}{\partial \theta}\right)^2 + \left(\frac{1}{R_0} \frac{\partial w}{\partial \theta}\right)^2 \right]^{-\frac{1}{2}} \left\{ 1 + \frac{\partial v}{\partial \theta} + \frac{R_0 \left[\left(R_0 + \frac{\partial v}{\partial \theta}\right) \left(\frac{\partial w}{\partial \theta}\right)^2 + \left(R_0 + w\right) \frac{\partial w}{\partial \theta} \frac{\partial^2 v}{\partial \theta^2} - \left(R_0 + \frac{\partial v}{\partial \theta}\right) \left(R_0 + w\right) \frac{\partial^2 w}{\partial \theta^2} \right]}{\left(R_0 + w\right)^2 \left(R_0 + \frac{\partial v}{\partial \theta}\right)^2} \right\} - \frac{1}{R_0} \quad (2.48)$$

Moreover, if ratios of displacements, u , v , w , to radius R_0 are assumed to be infinitesimal, the relationships between displacements and strains under infinitesimal deformation are given by;

$$\varepsilon_x = \frac{\partial u}{\partial x} \quad (2.49)$$

$$\varepsilon_\theta = \frac{1}{R_0} \frac{\partial v}{\partial \theta} + \frac{w}{R_0} \quad (2.50)$$

$$\gamma_{x\theta} = \frac{1}{R_0} \frac{\partial u}{\partial \theta} + \frac{\partial v}{\partial x} \quad (2.51)$$

$$\kappa_\theta = \frac{1}{R_0^2} \left(\frac{\partial v}{\partial x} - \frac{\partial^2 w}{\partial x \partial \theta} \right) \quad (2.52)$$

2.4 Summary

· Basic theories of compressible fluid mechanics and material mechanics are described.

· Mass and momentum conservation equations in one-dimensional compressible gas flow are derived.

· Choked flow which has limited maximum mass flow rate is explained.

· The Rayleigh-Plesset equation describing bubble growth is derived.

· The relationships between displacements and strains of a shell element in a thin cylinder under finite deformation are derived.

Chapter 3

The UT offshore model description

The present chapter introduces the UT offshore model in detail. The UT offshore model is the first model to describe unstable ductile fracture in offshore pipelines where coupling phenomenon between gas decompression, bubble growth, pipe deformation and crack propagation. The model is based on the UT model developed by Misawa et al.[30], and improved by the author so that the model can be applied to offshore pipelines. The model is developed by Mathematica which are well-known formula manipulation language.

3.1 Overview of the UT offshore model

Fig. 3.1 shows the fracture behavior in offshore pipelines. The features of the fracture behavior as follows:

- Gas decompression delays due to the bubble formation/growth, as compared with free gas decompression in onshore pipelines. Delayed decompression keeps higher pressure at a crack tip, which makes a crack more likely to propagate.
- Pipe deformation is constrained by surrounding water, which makes a crack more likely to be arrested.
- Hydrostatic pressure also constrains pipe deformation, which makes a crack more likely to be arrested.
- External dynamic pressure generated by bubble growth also constrains pipe deformation, which makes a crack more likely to be arrested.

The UT offshore model incorporates the features explained above other than the effect of external dynamic pressure. The velocity of pressure wave generated by bubble formation/growth, which is around 1,500m/s is far faster than ductile crack velocity which is slower than 400m/s. Therefore, the effect of external dynamic pressure on unstable ductile fracture is reasonably neglected.

The UT offshore model consists of four sub models: gas decompression model, bubble growth model, pipe deformation model and crack propagation model. Each model is described in detail below.

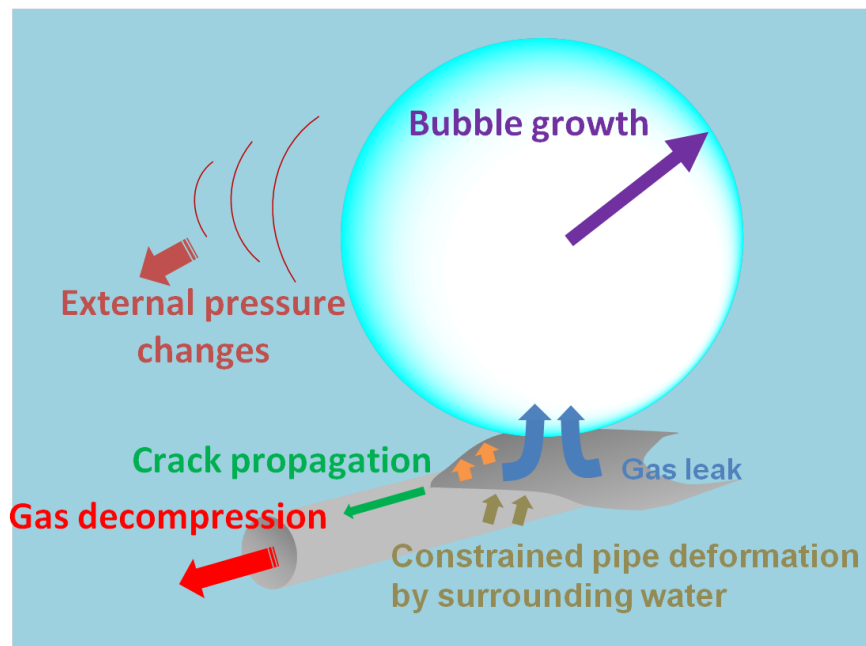


Fig. 3.1 Overview of the fracture behavior in offshore pipelines

3.2 Pipe deformation model

3.2.1 Governing equation

Pipe deformation modeling is based on the Freund model, where governing equation of pipe deformation is reduced to one-dimensional time-dependent partial differential equation with regard to single parameter[31].

Displacement components are defined as shown in Fig. 3.2: v and w are circumferential and radial displacements, and we assumed that axial displacement u can be neglected. According to the finite deformation theory, strain components are given by;

$$\varepsilon_x = \sqrt{\left(\frac{w}{R_0} + 1\right)^2 \left(\frac{\partial v}{\partial x}\right)^2 + \left(\frac{\partial w}{\partial x}\right)^2} - 1 \quad (3.1)$$

$$\varepsilon_\theta = \sqrt{\left(\frac{w}{R_0} + 1\right)^2 \left(\frac{1}{R_0} \frac{\partial v}{\partial \theta} + 1\right)^2 + \left(\frac{1}{R_0} \frac{\partial w}{\partial \theta}\right)^2} - 1 \quad (3.2)$$

$$\gamma_{x\theta} = \left(\frac{w}{R_0} + 1\right)^2 \frac{\partial v}{\partial x} \left(\frac{1}{R_0} \frac{\partial v}{\partial \theta} + 1\right) + \frac{1}{R_0} \frac{\partial w}{\partial x} \frac{\partial w}{\partial \theta} \quad (3.3)$$

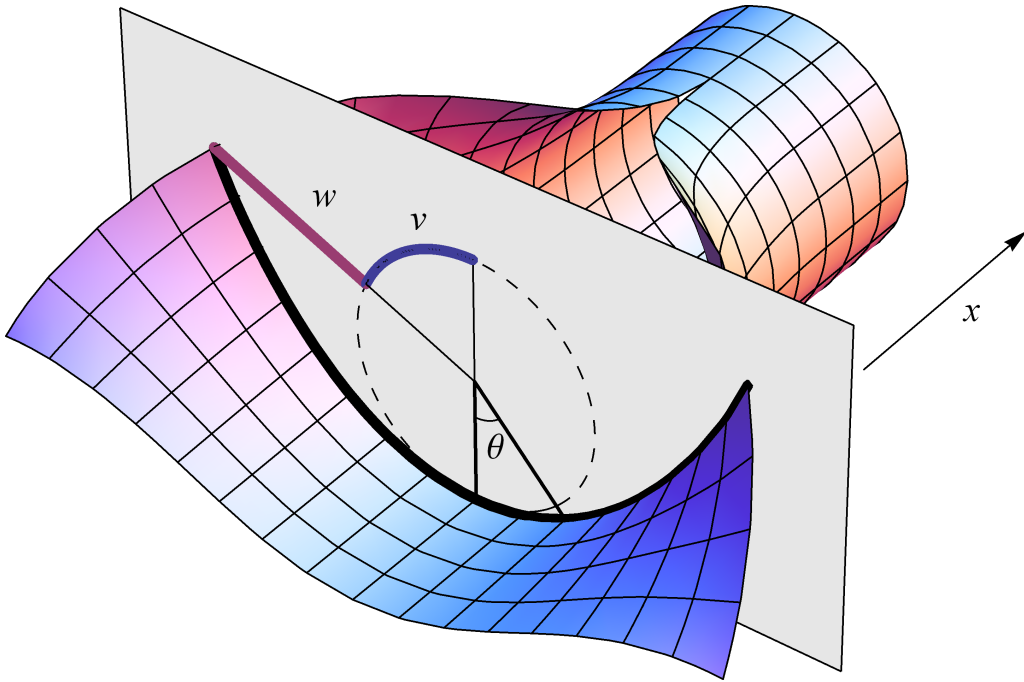


Fig. 3.2 Coordinates and displacements of deformed pipe

where R_0 is pipe radius. From the experimental measurements[30], circumferential strain ε_θ is so small that we assumed that $\varepsilon_\theta = 0$. Thus, Eq. (3.2) can be rewritten as;

$$\begin{aligned} \varepsilon_\theta &= \sqrt{\left(\frac{w}{R_0} + 1\right)^2 \left(\frac{1}{R_0} \frac{\partial v}{\partial \theta} + 1\right)^2 + \left(\frac{1}{R_0} \frac{\partial w}{\partial \theta}\right)^2} - 1 = 0 \\ \therefore \left(\frac{w}{R_0} + 1\right)^2 \left(\frac{1}{R_0} \frac{\partial v}{\partial \theta} + 1\right)^2 + \left(\frac{1}{R_0} \frac{\partial w}{\partial \theta}\right)^2 &= 1 \end{aligned} \quad (3.4)$$

A change in circumferential curvature κ_θ is expressed as follows using

Eq. (2.48) and Eq. (3.4);

$$\kappa_{\theta} = \frac{1}{R_0^2} \frac{\partial v}{\partial \theta} + \frac{\left(R_0 + \frac{\partial v}{\partial \theta}\right) \left(\frac{\partial w}{\partial \theta}\right)^2 + (R_0 + w) \frac{\partial w}{\partial \theta} \frac{\partial^2 v}{\partial \theta^2} - \left(R_0 + \frac{\partial v}{\partial \theta}\right) (R_0 + w) \frac{\partial^2 w}{\partial \theta^2}}{(R_0 + w)^2 \left(R_0 + \frac{\partial v}{\partial \theta}\right)^2} \quad (3.5)$$

Equation (3.4) means that if either w or v is determined, the other one is determined. According to the experimental measurements[30], radial displacement w can be expressed as a function of shape parameter ψ , see Fig. 3.3;

$$w(\psi, \theta) = 2R_0\psi \left(1 - \cos \frac{\theta}{2}\right) \quad (3.6)$$

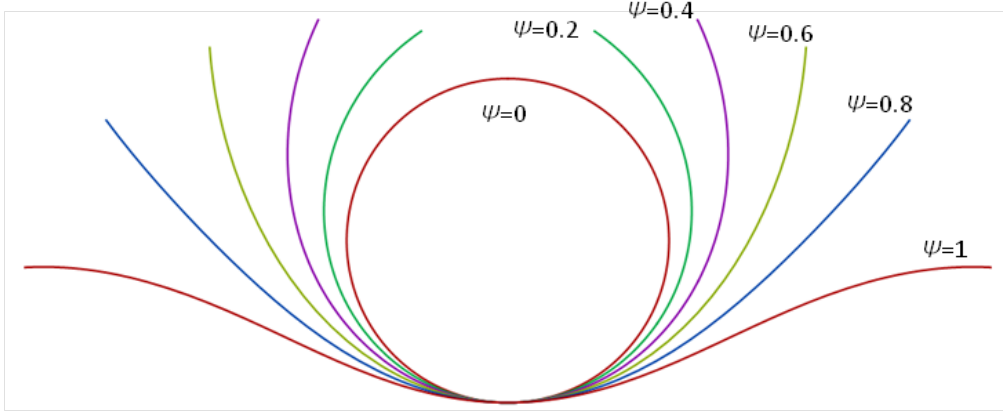


Fig. 3.3 Shape parameter ψ determining pipe deformation

Because circumferential displacement v can also be expressed as a function of ψ , strain components and a change in circumferential curvature in Eq. (3.1), Eq. (3.3) and Eq. (3.5) are expressed by using shape parameter ψ as follows;

$$\varepsilon_x = \varepsilon_x \left(\psi, \frac{\partial \psi}{\partial x}, \theta \right) \quad (3.7)$$

$$\gamma_{x\theta} = \gamma_{x\theta} \left(\psi, \frac{\partial \psi}{\partial x}, \theta \right) \quad (3.8)$$

$$\kappa_{\theta} = \kappa_{\theta} (\psi, \theta) \quad (3.9)$$

For the derivation of the governing equation, suppose for a thin-shell element of a pipe where axial force N_x , shear force $Q_{x\theta}$ and circumferential

bending moment M_θ are acting, see Fig. 3.4. Axial force N_x , shear force $Q_{x\theta}$ and circumferential bending moment M_θ are expressed as;

$$N_x(\psi, \psi, x) = \int_{-h/2}^{h/2} \sigma(\varepsilon_x(\psi, \psi, x)) dz = h\sigma(\varepsilon_x(\psi, \psi, x)) \quad (3.10)$$

$$Q_{x\theta}(\psi, \psi, x) = \int_{-h/2}^{h/2} \tau(\gamma_{x\theta}(\psi, \psi, x)) dz = h\tau(\gamma_{x\theta}(\psi, \psi, x)) \quad (3.11)$$

$$M_\theta(\psi) = \int_{-h/2}^{h/2} z\sigma(z\kappa_\theta(\psi)) dz \quad (3.12)$$

where h is pipe wall thickness and distribution along the thickness direction of stress and strain are assumed as shown in Fig. 3.5. In addition, it is assumed that axial force N_x , shear force $Q_{x\theta}$ and circumferential bending moment M_θ are yielded separately.

In the present study, for considering non-linearity, the author assumed that materials of interest follow the power hardening law;

$$\sigma(\varepsilon) = \begin{cases} E\varepsilon & \text{for } |\varepsilon| < \varepsilon_{YS} \\ E\sigma_{YS} \left(\frac{\varepsilon}{\varepsilon_{YS}}\right)^n & \text{for } \varepsilon_{YS} \leq \varepsilon \\ -E\sigma_{YS} \left(\frac{-\varepsilon}{\varepsilon_{YS}}\right)^n & \text{for } \varepsilon \leq -\varepsilon_{YS} \end{cases} \quad (3.13)$$

$$\tau(\gamma) = \begin{cases} G\gamma & \text{for } |\gamma| < \gamma_{YS} \\ G\tau_{YS} \left(\frac{\gamma}{\gamma_{YS}}\right)^n & \text{for } \gamma_{YS} \leq \gamma \\ -G\tau_{YS} \left(\frac{-\gamma}{\gamma_{YS}}\right)^n & \text{for } \gamma \leq -\gamma_{YS} \end{cases} \quad (3.14)$$

where σ is tensile stress, τ is shear stress, G is shear modulus, σ_{YS} is tensile yield stress, τ_{YS} is shear yield stress which is assumed to be equal to $0.5\sigma_{YS}$ from the Tresca yield criterion, ε_{YS} is tensile yield strain and γ_{YS} is shear yield strain. Tensile yield stress σ_{YS} is calculated by substituting $\dot{\varepsilon} = 10^2$ (/sec) into Eq. (3.15) which determine the tensile yield stress depending on strain rate $\dot{\varepsilon}$ empirically[42].

$$\sigma_{YS} = \sigma_{YS0} \exp \left[(497.5 - 68.90 \ln \sigma_{YS0}) \left(\frac{1}{T} \frac{28.32}{18.42 - \ln \dot{\epsilon}} - \frac{1}{293} \right) \right] \quad (3.15)$$

where σ_{YS0} (MPa) is tensile yield stress at the quasi-static condition and T (K) is temperature. n is strain hardening exponent which is determined from the empirical equation as follows[43];

$$n = -0.11097 + \frac{169.63}{\sigma_{YS}} - \frac{19580}{\sigma_{YS}^2} \quad (3.16)$$

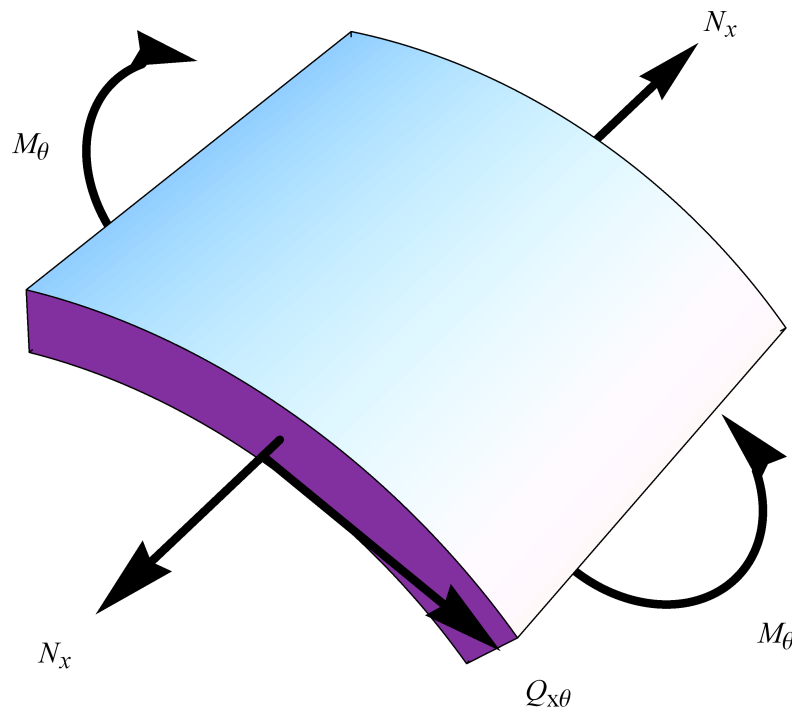


Fig. 3.4 Thin-shell element receiving forces and bending moment

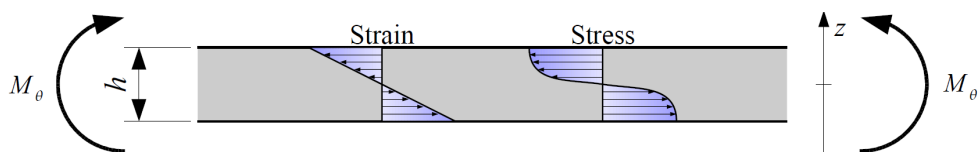


Fig. 3.5 Distribution of stress and strain generated by bending moment in thickness direction

Finally, the governing equation for pipe deformation is obtained using the principle of virtual work. Internal work W_{int} and external work W_{ext} in a thin shell element of a pipe as shown Fig. 3.5 in are given by;

$$W_{\text{int}} = \iint_S (N_x \delta \varepsilon_x + Q_{x\theta} \delta \gamma_{x\theta} + M_\theta \delta \kappa_\theta) dS \quad (3.17)$$

$$W_{\text{ext}} = \iint_S \left\{ (p - p_{\text{static}}) \delta w - \rho_{\text{pipe}} h \left[\left(\frac{\partial^2 v}{\partial t^2} \right) \delta v + \left(\frac{\partial^2 w}{\partial t^2} \right) \delta w \right] \right\} dS \quad (3.18)$$

where p is internal pressure, p_{static} is hydrostatic pressure, ρ_{pipe} is density of a pipe steel, and S covers whole mid-surface of a pipe. Note that increasing water depth which increases hydrostatic pressure decreases the internal work; the fact that increasing water depth constrains pipe deformation is considered in the pipe deformation model. By using virtual displacement $\delta \psi$, increments of strain components and displacement components are given by;

$$\delta \varepsilon_x = \frac{\partial \varepsilon_x}{\partial \psi} \delta \psi + \frac{\partial \varepsilon_x}{\partial \psi_{,x}} \delta \psi_{,x} \quad (3.19)$$

$$\delta \gamma_{x\theta} = \frac{\partial \gamma_{x\theta}}{\partial \psi} \delta \psi + \frac{\partial \gamma_{x\theta}}{\partial \psi_{,x}} \delta \psi_{,x} \quad (3.20)$$

$$\delta \kappa_\theta = \frac{\partial \kappa_\theta}{\partial \psi} \delta \psi \quad (3.21)$$

$$\delta v = \frac{\partial v}{\partial \psi} \delta \psi \quad (3.22)$$

$$\delta w = \frac{\partial w}{\partial \psi} \delta \psi \quad (3.23)$$

where $\psi_{,x} \equiv \frac{\partial \psi}{\partial x}$. Also, secondary partial derivatives of the displacement components with respect to time t are given by;

$$\frac{\partial^2 v}{\partial t^2} = \frac{\partial v}{\partial \psi} \frac{\partial^2 \psi}{\partial t^2} + \frac{\partial^2 v}{\partial \psi^2} \left(\frac{\partial \psi}{\partial t} \right)^2 \quad (3.24)$$

$$\frac{\partial^2 w}{\partial t^2} = \frac{\partial w}{\partial \psi} \frac{\partial^2 \psi}{\partial t^2} + \frac{\partial^2 w}{\partial \psi^2} \left(\frac{\partial \psi}{\partial t} \right)^2 \quad (3.25)$$

Setting $W_{\text{int}} = W_{\text{ext}}$ leads to the following equation;

$$\int_0^L \int_{-\pi}^{\pi} \left\{ N_x \frac{\partial \varepsilon_x}{\partial \psi} + Q_{x\theta} \frac{\partial \gamma_{x\theta}}{\partial \psi} + M_\theta \frac{\partial \kappa_\theta}{\partial \psi} - \frac{\partial}{\partial x} \left(N_x \frac{\partial \varepsilon_x}{\partial \psi_{,x}} + Q_{x\theta} \frac{\partial \gamma_{x\theta}}{\partial \psi_{,x}} \right) - (p - p_{\text{static}}) \frac{\partial w}{\partial \psi} \right. \\ \left. + \rho_{\text{pipe}} h \left[\left(\frac{\partial v}{\partial \psi} \right)^2 + \left(\frac{\partial w}{\partial \psi} \right)^2 \right] \frac{\partial^2 \psi}{\partial t^2} + \rho_{\text{pipe}} h \left[\frac{\partial v}{\partial \psi} \frac{\partial^2 v}{\partial \psi^2} + \frac{\partial w}{\partial \psi} \frac{\partial^2 w}{\partial \psi^2} \right] \left(\frac{\partial \psi}{\partial t} \right)^2 \right\} \delta \psi d\theta dx = 0 \quad (3.26)$$

where L is pipe length. Because virtual displacement $\delta \psi$ is an arbitrary function with respect to x , the following equation should hold;

$$F_1(\psi, \psi_{,x}) + (p - p_{\text{static}})(x, t) F_2(\psi) + \frac{\partial}{\partial x} F_3(\psi, \psi_{,x}) + F_4(\psi) \left(\frac{\partial \psi}{\partial t} \right)^2 + F_5(\psi) \frac{\partial^2 \psi}{\partial t^2} = 0 \quad (3.27)$$

where,

$$F_1(\psi, \psi_{,x}) = \int_{-\pi}^{\pi} \left(N_x \frac{\partial \varepsilon_x}{\partial \psi} + Q_{x\theta} \frac{\partial \gamma_{x\theta}}{\partial \psi} + M_\theta \frac{\partial \kappa_\theta}{\partial \psi} \right) d\theta \quad (3.28)$$

$$F_2(\psi) = \int_{-\pi}^{\pi} \frac{\partial w}{\partial \psi} d\theta \quad (3.29)$$

$$F_3(\psi, \psi_{,x}, \psi_{,xx}) = - \int_{-\pi}^{\pi} \left(N_x \frac{\partial \varepsilon_x}{\partial \psi_{,x}} + Q_{x\theta} \frac{\partial \gamma_{x\theta}}{\partial \psi_{,x}} \right) d\theta \quad (3.30)$$

$$F_4(\psi) = \int_{-\pi}^{\pi} \rho_{\text{pipe}} h \left(\frac{\partial v}{\partial \psi} \frac{\partial^2 v}{\partial \psi^2} + \frac{\partial w}{\partial \psi} \frac{\partial^2 w}{\partial \psi^2} \right) d\theta \quad (3.31)$$

$$F_5(\psi) = \int_{-\pi}^{\pi} \rho_{\text{pipe}} h \left[\left(\frac{\partial v}{\partial \psi} \right)^2 + \left(\frac{\partial w}{\partial \psi} \right)^2 \right] d\theta \quad (3.32)$$

Equation (3.27) is the governing equation for pipe deformation, which is time dependent one-dimensional partial differential equation with respect to axial direction x . After the discretization with respect to x and t , solving Eq. (3.27) using finite difference method gives pipe deformation profile along to axial direction at each time step. Equation (3.28) to Eq. (3.32) can be calculated preliminarily. Because these term need not be calculated time step by time step, CPU cost is reduced.

Initial conditions and boundary conditions are given by;

$$\psi(t = 0, x) = \frac{\partial \psi}{\partial t}(t = 0, x) = 0 \quad (3.33)$$

$$\psi(t, x = x_{ct}) = \frac{\partial \psi}{\partial x}(t, x = 0) = 0 \quad (3.34)$$

where, x_{ct} is the position of a crack tip. Equation (3.27) is solved between $x = 0$ and x_{ct} . In the present study, a half of a pipe is calculated using symmetry conditions. Therefore, the position of $x = 0$ is located at the center of a initial crack.

3.2.2 Water backfill effect

When a pipe is laid underwater, pipe deformation is constrained by the surrounding water. In the present study, the water backfill effect is considered as an added density by calculating kinetic energy of surrounding water that is forced to move by pipe deformation. Formulation of the water backfill effect is explained below.

Suppose for a pipe buried to the water depth of h_b , see Fig. 3.6. In order to evaluate the water backfill effect, three assumptions with regard to the water movement are considered as follows:

- the water is continuum with constant volume and density: non-compressible fluid
- the water has velocity only in the radial direction
- shear force does not act in the water

From these assumptions, radial velocity of the water, which is located r away from the pipe center, is given by;

$$\dot{w}_{\text{water}} = \frac{R_0}{r} \frac{\partial w}{\partial r} \quad (3.35)$$

Thus, the whole kinetic energy of the water ranging from the pipe surface to the water surface is given by;

$$2 \int_0^{\pi - \theta_{\text{open}}(\psi)} \int_{R_0 + w(\psi, \theta)}^{R_0 + h_b} \frac{1}{2} \rho_{\text{water}} \left(\frac{R_0 + w(\psi, \theta)}{r} \frac{\partial w}{\partial t} \right)^2 r dr d\theta \quad (3.36)$$

where, ρ_{water} is density of the water. θ_{open} is the angle where a pipe is opening, see Fig. 3.6. It is assumed that the water inside the angle of θ_{open} is moved by the leaked gas.

On the other hand, if it is assumed that the water is condensed toward the pipe surface and has the same thickness h as a pipe wall, kinetic energy of the condensed water is given by;

$$2 \int_0^{\pi} \int_{R_0}^{R_0 + h} \frac{1}{2} \rho_{\text{add}} \left(\frac{\partial w}{\partial t} \right)^2 r dr d\theta \quad (3.37)$$

where, ρ_{add} is added density of a pipe.

Setting Eq. (3.36) equal to Eq. (3.37) leads to the equation of added density as a function of pipe radius R_0 , pipe thickness h , water depth h_b , density of the water ρ_{water} and shape parameter ψ ;

$$\rho_{\text{add}} = \rho_{\text{add}}(R_0, h, h_b, \rho_{\text{water}}, \psi) \quad (3.38)$$

The dependence of added density on shape parameter and depth for $\rho_{\text{water}} = 1,000 \text{kg/m}^3$, $R_0 = 12 \text{inches}$ and $h = 30 \text{mm}$ is shown in Fig. 3.7.

In order to take into account the water backfill effect of the pipe deformation model, $F_4(\psi)$ and $F_5(\psi)$ in Eq. (3.31) and Eq. (3.32) are modified by adding the term of the added density ρ_{add} with regard to radial direction;

$$\bar{F}_4(\psi) = \int_{-\pi}^{\pi} \left[\rho_{\text{pipe}} h \left(\frac{\partial v}{\partial \psi} \frac{\partial^2 v}{\partial \psi^2} + \frac{\partial w}{\partial \psi} \frac{\partial^2 w}{\partial \psi^2} \right) + \rho_{\text{add}} h \frac{\partial w}{\partial \psi} \frac{\partial^2 w}{\partial \psi^2} \right] d\theta \quad (3.39)$$

$$\bar{F}_5(\psi) = \int_{-\pi}^{\pi} \left\{ \rho_{\text{pipe}} h \left[\left(\frac{\partial v}{\partial \psi} \right)^2 + \left(\frac{\partial w}{\partial \psi} \right)^2 \right] + \rho_{\text{add}} h \left(\frac{\partial w}{\partial \psi} \right)^2 \right\} d\theta \quad (3.40)$$

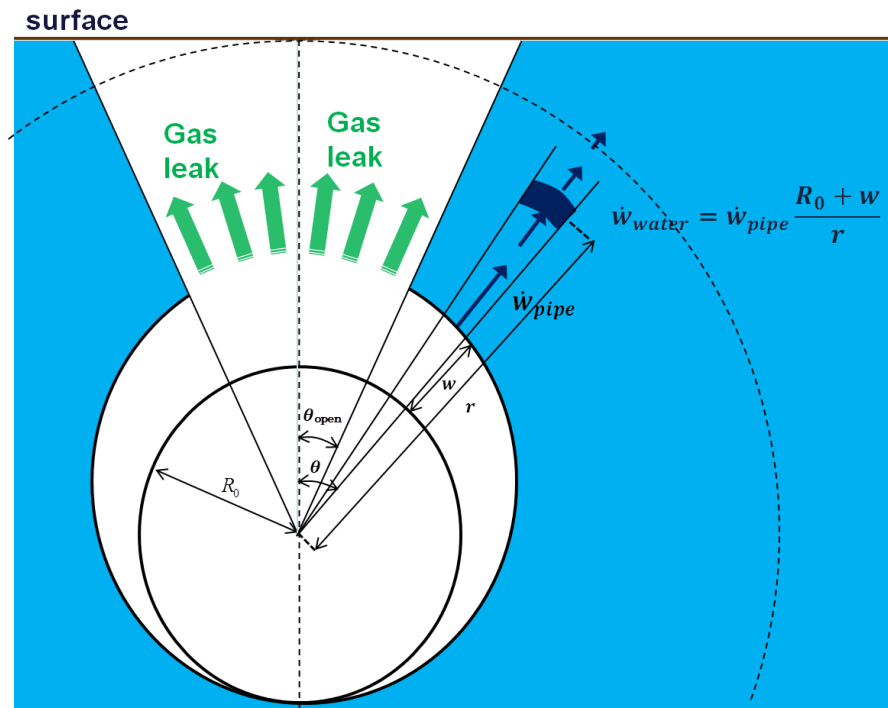


Fig. 3.6 Water backfill around a pipe

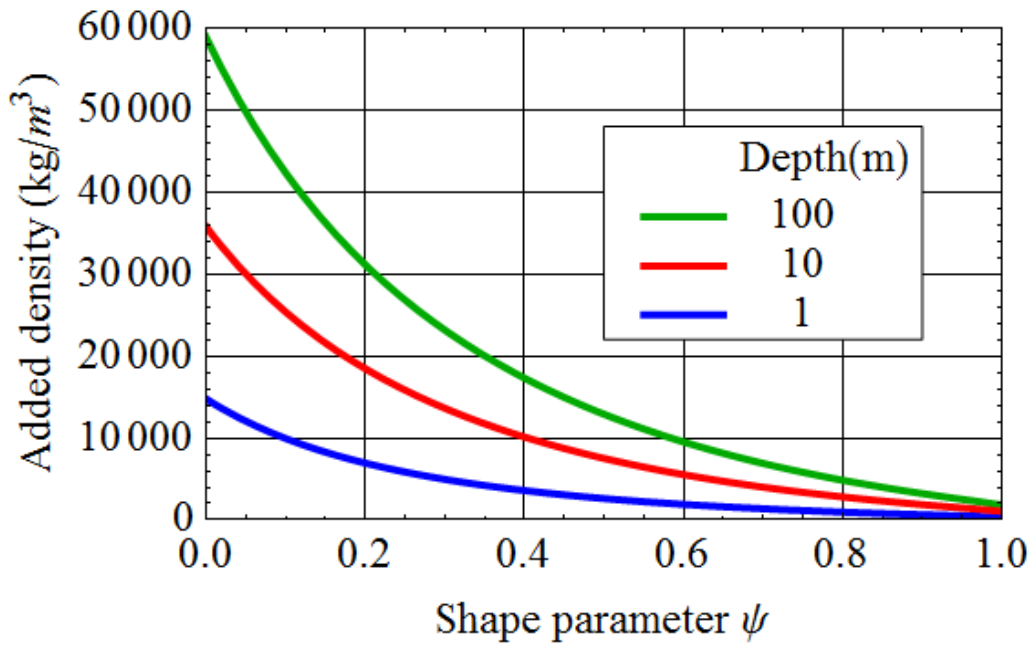


Fig. 3.7 Dependence of shape parameter and water depth on added density, $\rho_{water} = 1,000\text{kg/m}^3$, $R_0 = 12\text{inch}$ and $h = 30\text{mm}$

3.3 Gas decompression model

3.3.1 Governing equations

In the present study, it is assumed that gas flow is one-dimensional and thermodynamic behavior is based on isentropic change. In order to consider the gas leak from the crack opening as shown in Fig. 3.8, the mass conservation equation of Eq. (2.2) is modified as follows;

$$\begin{aligned}
 (\rho u A) \Delta t &= \frac{\partial (\rho A \Delta x)}{\partial t} \Delta t + \left[\rho u A + \frac{\partial (\rho u A)}{\partial x} \Delta x \right] \Delta t + \dot{m} \Delta t \\
 \therefore \frac{\partial (\rho A)}{\partial t} + \frac{\partial (\rho u A)}{\partial x} + \frac{\dot{m}}{\Delta x} &= 0
 \end{aligned} \tag{3.41}$$

where, \dot{m} is mass flow rate which is going out from the crack opening to the bubble. By using crack opening length ϕ as shown in Fig. 3.9, \dot{m} is expressed as;

$$\dot{m} = \Delta x \phi \underline{\dot{m}}(p, T) \tag{3.42}$$

where, $\underline{\dot{m}}$ is mass flow rate per unit area of the crack opening.

Therefore, the mass conservation equation of a cracked pipe is given by;

$$\frac{\partial (\rho A)}{\partial t} + \frac{\partial (\rho u A)}{\partial x} + \phi \underline{\dot{m}}(p, T) = 0 \tag{3.43}$$

To summarize, the governing equations of gas decompression in a cracked pipe is as follows using Eq. (2.3), Eq. (2.8) and Eq. (2.9);

$$\frac{\partial (\rho A)}{\partial t} + \frac{\partial (\rho u A)}{\partial x} + \phi \underline{\dot{m}}(p, T) = 0 \tag{3.44}$$

$$\frac{\partial (\rho u A)}{\partial t} + \frac{\partial (\rho u^2 A)}{\partial x} = -A \frac{\partial p}{\partial x} \tag{3.45}$$

$$\rho = \rho(p) \tag{3.46}$$

$$T = T(p) \tag{3.47}$$

In the present study, cross sectional area A of a pipe is assumed to be constant, which is equal to πR_0^2 . Crack opening length ϕ is calculated from the pipe deformation model. Equation (3.46) and Eq. (3.47) are obtained using commercial software such as GASDECOM and REFPROP; GASDECOM predicts state change of natural gas well, on the other hand, REFPROP is suitable especially for gas containing carbon dioxide[44, 45].

Equation (3.44) and Eq. (3.45) are time dependent one-dimensional partial differential equations with respect to axial direction x . After discretization with respect to x and t , solving Eq. (3.44) and Eq. (3.45) using finite difference method gives the distributions of pressure, density, gas flow rate and temperature along to axial direction at each time step.

Initial conditions and boundary conditions are as follows;

$$p(t = 0, x) = p_0 \quad (3.48)$$

$$T(t = 0, x) = T_0 \quad (3.49)$$

$$u(t = 0, x) = 0 \quad (3.50)$$

$$\frac{\partial p}{\partial x}(t, x = 0) = 0 \quad (3.51)$$

$$u(t, x = x_L) = 0 \quad (3.52)$$

where, p_0 , T_0 and L are initial pressure, initial temperature and pipe length, respectively.

3.3.2 Gas leak

3.3.2.1 Gas leak from pipe to bubble through crack opening

When a pipe is laid underwater, gas leak might be constrained by bubble formation/growth, which leads to the delay of gas decompression. In order to incorporate this phenomena, mass flow rate per unit area from the crack opening to the bubble \dot{m} is formulated so that it depends on the pressure inside the bubble. The formulation is described in detail below.

Gas leak from the crack opening to the bubble is modeled by the leak from a substantially large tank to the exterior environment which is regarded as bubble interior in the present study, see Fig. 3.10. p_0 , p and p_B

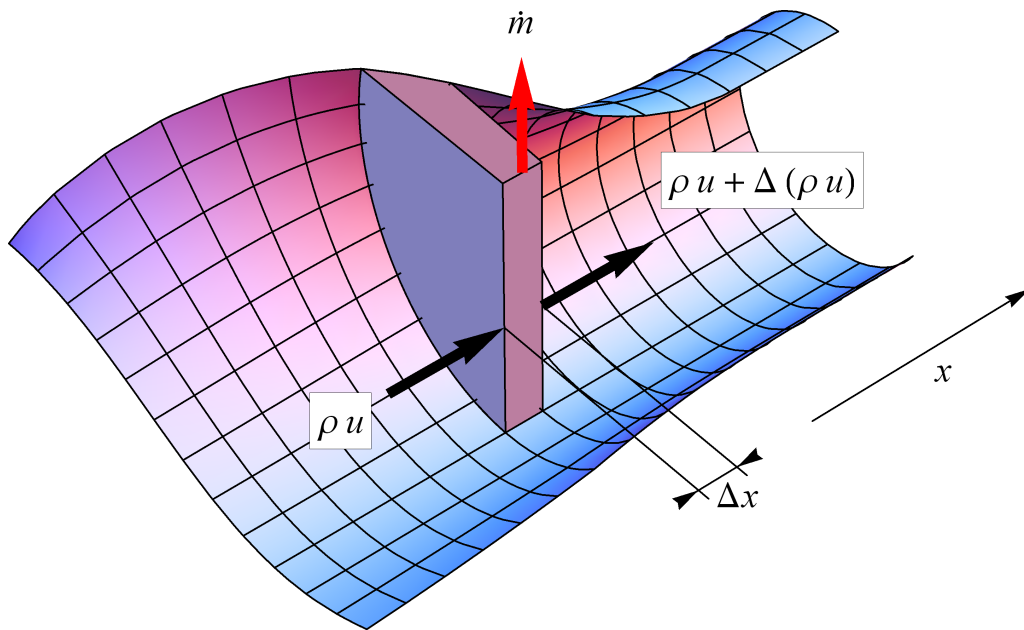


Fig. 3.8 Mass conservation of fluid with leakage from a crack opening

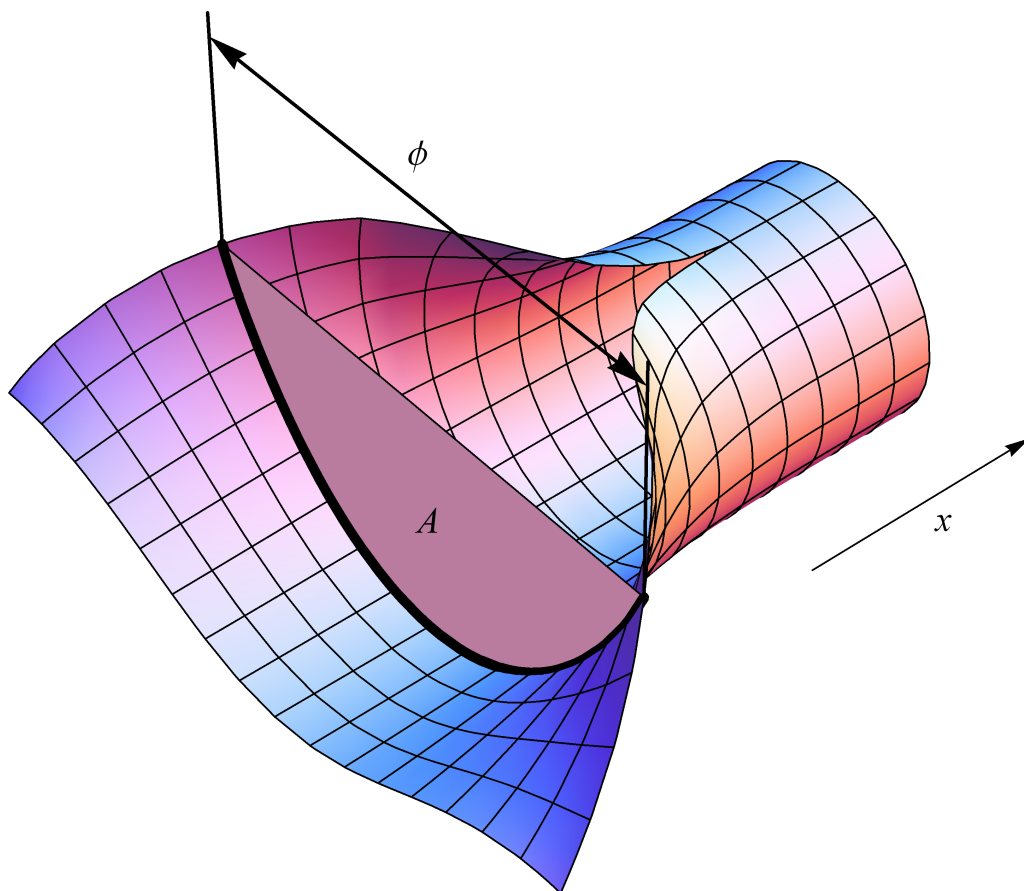


Fig. 3.9 Crack opening length of deformed pipe

is considered as pressure inside the pipe, leaking gas pressure and pressure inside the bubble, respectively.

For the ideal gas, as Eq. (2.18) indicates, mass flow rate through the cross sectional area A is given by

$$\dot{m} = \frac{p_0 A}{\sqrt{RT_0}} \sqrt{\frac{2\gamma}{\gamma-1} H(p/p_0)} \quad (3.53)$$

where,

$$H(p/p_0) = \left[\left(\frac{p}{p_0} \right)^{\frac{2}{\gamma}} - \left(\frac{p}{p_0} \right)^{\frac{\gamma+1}{\gamma}} \right] \quad (3.54)$$

The function $H(p/p_0)$ determines the value of mass flow rate. Fig. 3.11 shows the dependence of H on the pressure ratio p/p_0 for specific heat ratio $\gamma = 1.4$. As Fig. 3.11 shows, the function $H(p/p_0)$ has the maximum value for $p/p_0 \cong 0.528$, when gas flow is said to be choked. The pressure of choked leaking gas flow is referred to as p_{choked} hereafter, which is nearly equal to $0.528p_0$ for the ideal gas with γ of 1.4.

However, it is reasonably assumed that the leaking gas pressure p should be greater than the pressure in the exterior environment p_B . Therefore, if $p_B > p_{\text{choked}}$, leaking gas pressure p cannot be choked pressure p_{choked} , if not, leaking gas pressure p becomes p_{choked} . In the present study, it is assumed that leaking gas pressure p becomes p_B when $p_B > p_{\text{choked}}$, which leads the maximum value of the function H within the possible range of leaking gas pressure p .

For the actual gas, the function of $H(p/p_0)$ and the pressure of choked leaking gas flow p_{choked} also exist. Therefore, mass flow rate per unit area \dot{m} is generally given by;

$$\dot{m} = \begin{cases} \frac{p_0}{\sqrt{RT_0}} \sqrt{\frac{2\gamma}{\gamma-1} H(p_B/p_0)} & \text{for } p_B > p_{\text{choked}} \\ \frac{p_0}{\sqrt{RT_0}} \sqrt{\frac{2\gamma}{\gamma-1} H(p_{\text{choked}}/p_0)} & \text{for } p_B \leq p_{\text{choked}} \end{cases} \quad (3.55)$$

To summarize, mass flow rate per unit area \dot{m} is expressed as a function of pressure inside the bubble and the pipe when $p_B > p_{\text{choked}}$, which decreases with the increasing pressure inside the bubble. On the other hand, mass flow rate per unit area \dot{m} is determined only by the pressure inside

the pipe when $p_B \leq p_{\text{choked}}$ because p_{choked} is determined by the pressure inside the pipe. By incorporating the formulation of mass flow rate depending on the pressure inside the bubble into the model, the delay of gas decompression by bubble formation/growth is considered.

Fig. 3.12 shows a example of calculated mass flow rate depending on the pressure inside the bubble for a standard rich natural gas. Note that in the present study, density represented in the vertical axis is proportional to pressure due to the isentropic assumption.

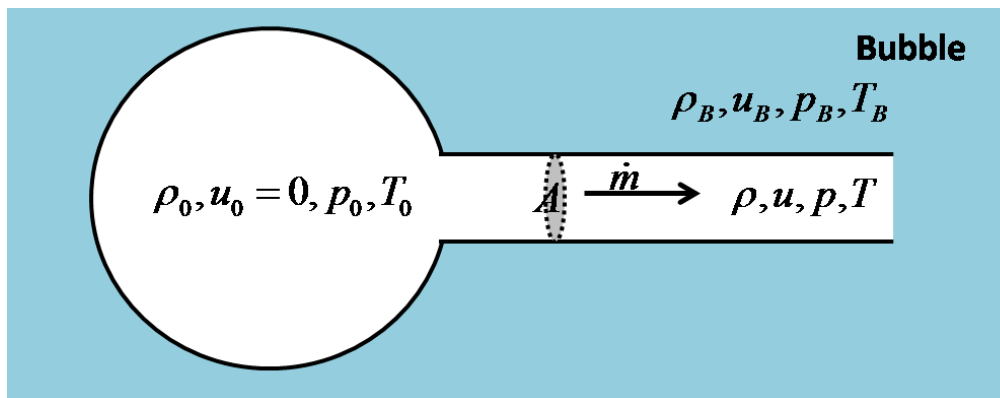


Fig. 3.10 Gas leakage from a pipe to a bubble

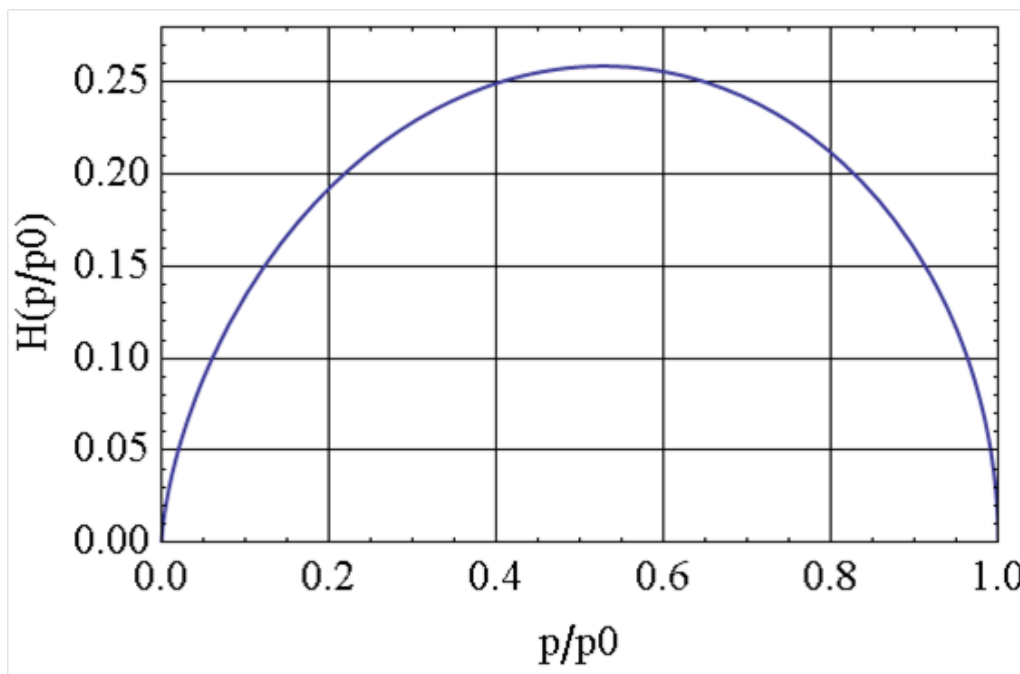


Fig. 3.11 Dependence of the ratio of leaking pressure to internal pressure on function H determining mass flow rate

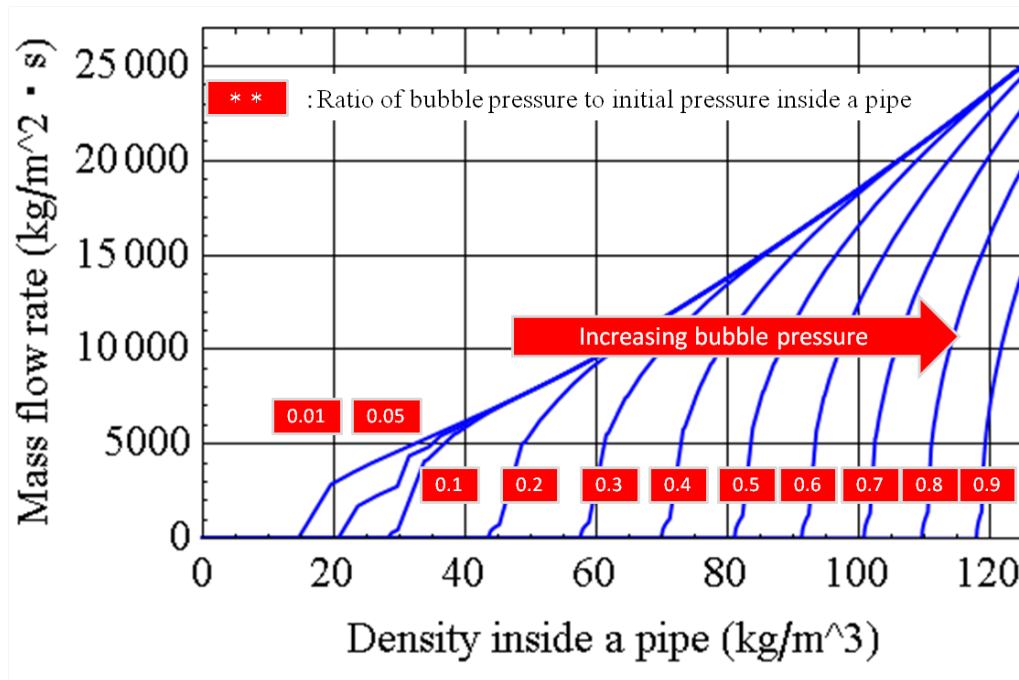


Fig. 3.12 Dependence of mass flow rate on bubble pressure and initial pressure

3.3.2.2 Gas leak in the axial direction from the full bore opening at the pipe center to the bubble

Because a half of a pipe is calculated using symmetry conditions in the present study, gas flow exists at the pipe center, which is referred to as $x = 0$ in the calculation, as shown in Fig. 3.23 which shows an example of calculated gas flow rate distribution using the present model. In order to satisfy the mass balance within the pipe and the bubble, mass flow rate of gas flow in the axial direction at the pipe center should be transformed into the leak to the bubble. Otherwise, mass flow rate at the pipe center just disappear.

In the present study, mass flow rate of gas flow in the axial direction at the pipe center, which is referred to as axial mass flow rate hereafter, is assumed to be transformed into added gas leak from the pipe to the bubble through the crack opening. Transformed axial mass flow rate is distributed linearly from the pipe center $x = 0$ to $x = 4R_0$, which corresponds to four times pipe radius, so that added mass flow rate is equal to zero at $x = 4R_0$.

The author confirmed that ways of transformation of axial mass flow rate into added mass flow rate through the crack opening does not affect calculated results strongly.

3.4 Bubble growth model

Bubble growth has been studied over the years especially focusing on the bubble growth in underwater explosions [46, 47, 48, 49]. However, there are very few models of the bubble growth in offshore pipelines where axial crack propagates, of which is a finite based model developed by A. Meleddu et al., where crack propagation is not considered[50]. In the present study, bubble growth is reduced to the one-dimensional gas flow. The detailed description is below.

3.4.1 Governing equations

In the present study, it is assumed that bubble is one-dimensional gas flow with changing cross sectional area and thermodynamic behavior is based on isentropic change. In order to consider the gas supply from the pipe to the bubble through the crack opening as shown in Fig. 3.13, the mass conservation equation is different from Eq. (3.43) of the gas decompression model in that the sign of the term regarding mass flow rate \dot{m} is opposite;

$$\frac{\partial (\rho_B A_B)}{\partial t} + \frac{\partial (\rho_B u_B A_B)}{\partial x} - \phi \dot{m}(p, T) = 0 \quad (3.56)$$

$$A_B = \pi R_B^2 \quad (3.57)$$

where, ρ_B , u_B , A_B and R are bubble density, gas flow rate inside the bubble, cross sectional area of the bubble and bubble radius, respectively. Momentum conservation equation has the form as Eq. (3.45);

$$\frac{\partial (\rho_B u_B A_B)}{\partial t} + \frac{\partial (\rho_B u_B^2 A_B)}{\partial x} = -A_B \frac{\partial p_B}{\partial x} \quad (3.58)$$

where, p_B is bubble pressure.

Because cross section of the bubble is assumed to be circular and surrounding water is assumed not to move to the axial direction, bubble growth to the radial direction can be described by the cylindrical coordinates system. Rayleigh-Plesset equation of Eq. (2.31) is extended into the cylindrical coordinates system as follows;

$$\frac{\partial v}{\partial t} = \frac{1}{R \text{Log}(R_\infty/R)} \left[\frac{p_B - p_\infty}{\rho_L} - \text{Log}(R_\infty/R) + \frac{1}{2}v^2 - \frac{4\nu}{R} - \frac{2S}{\rho_L R} \right] \quad (3.59)$$

$$\frac{\partial R}{\partial t} = v \quad (3.60)$$

where, v , p_∞ , ρ_L , ν and S are bubble growth rate to the radial direction, hydrostatic pressure, density of the water, dynamic viscosity and surface tension per unit length. R_∞ is the infinite distance where the water is static, which is assumed to be equal to the water depth in the present study.

Because the gas flow inside the bubble is assumed to be isentropic, bubble density ρ_B and bubble temperature T_B are expressed as a function of bubble pressure p_B ;

$$\rho_B = \rho_B(p_B) \quad (3.61)$$

$$T_B = T_B(p_B) \quad (3.62)$$

Equation (3.61) and Eq. (3.62) are obtained using commercial software such as GASDECOM and REFPROP as well as gas decompression modeling.

Governing equations for bubble growth consist of Eq. (3.56), Eq. (3.57), Eq. (3.58), Eq. (3.59), Eq. (3.60), Eq. (3.61) and Eq. (3.56). Equation (3.56), Eq. (3.58), Eq. (3.59) and Eq. (3.60) are time dependent one-dimensional partial differential equations with respect to axial direction x . After the discretization with respect to x and t , solving these equations using finite difference method gives the distribution of bubble parameters along to axial direction at each time step.

Initial conditions are boundary conditions are as follows;

$$p_B(t = 0, x) = p_0 \quad (3.63)$$

$$T_B(t = 0, x) = T_0 \quad (3.64)$$

$$u_B(t = 0, x) = 0 \quad (3.65)$$

$$R(t = 0, x) = R_0 \quad (3.66)$$

$$v(t = 0, x) = 0 \quad (3.67)$$

$$\frac{\partial p_B}{\partial x}(t, x = 0) = 0 \quad (3.68)$$

$$u_B(t, x = x_{ct}) = 0 \quad (3.69)$$

$$\frac{\partial R_B}{\partial x}(t, x = 0) = 0 \quad (3.70)$$

$$\frac{\partial v_B}{\partial x}(t, x = 0) = 0 \quad (3.71)$$

where, p_0 , T_0 and x_{ct} are initial pressure and temperature inside the pipe and the position of a crack tip, respectively. R_0 is initial bubble radius which is set to 1mm in the present study. The governing equations for the bubble growth are solved between $x = 0$ and x_{ct} ; A tip of the bubble is located as a tip of a crack, which means that the bubble is assumed to expand to the axial direction with moving crack tip and assumed not to expand to the axial direction beyond a crack tip. Also, the central axis of the bubble is fixed at the central axis of the pipe. Although the bubble moves up by the effect of buoyancy force in the actual phenomena, this phenomena is negligible in the present study because crack velocity is much faster than rising velocity of the bubble. In the present study, a half of a pipe is calculated using symmetry conditions. Therefore, the position of $x = 0$ is located at the center of an initial crack.

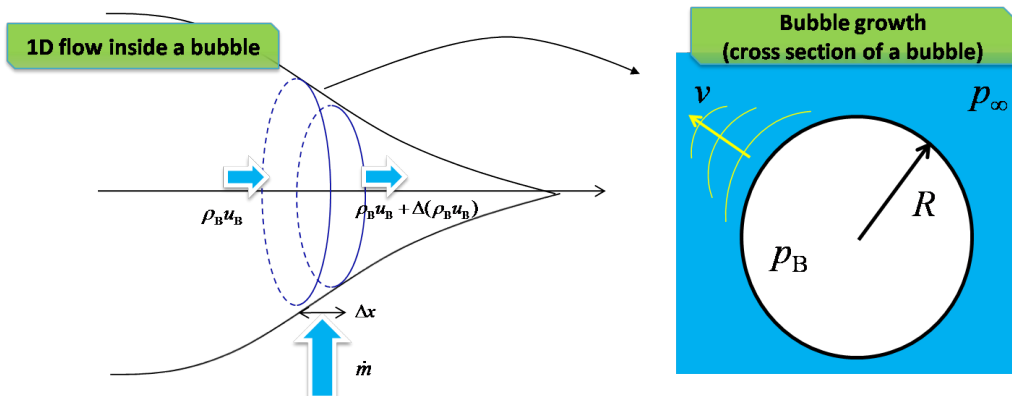


Fig. 3.13 One-dimensional compressible gas flow with increasing cross sectional area inside a bubble

3.4.2 Generation of a new node depending on crack propagation

A tip of the bubble extends as the crack propagates. Therefore, a new node is generated when the crack propagates by one incremental length Δx . Each value of a new node is set as follows;

$$p_B(t, x = x_{\text{new}}) = p(t, x = x_{\text{new}}) \quad (3.72)$$

$$T_B(t, x = x_{\text{new}}) = T(t, x = x_{\text{new}}) \quad (3.73)$$

$$u_B(t, x = x_{\text{new}}) = 0 \quad (3.74)$$

$$R(t, x = x_{\text{new}}) = R_0 \quad (3.75)$$

$$v(t, x = x_{\text{new}}) = 0 \quad (3.76)$$

To summarize, bubble pressure and temperature of a new node are set to pressure and temperature inside the pipe at the same position, and bubble radius and growth rate are set to initial bubble radius, which is 1mm through the present study, and zero, and gas flow rate inside the bubble is set to the same as the boundary condition.

3.5 Crack propagation model

A crack propagates by incremental length Δx when the propagation condition explained below is satisfied. In the present study, dynamic energy balance is applied to the crack propagation condition.

There are four kinds of energies to be considered: work done by gas to the pipe wall W_{gas} , strain energy generated by pipe deformation behind a crack tip U , Kinetic energy of the pipe wall and the surrounding water E_k and strain energy generated by crack tip singularity ahead of a crack tip U_R . Therefore, dynamic energy balance is given by;

$$\frac{dW_{\text{gas}}}{dx} - \frac{dU}{dx} - \frac{dE_k}{dx} - \frac{dU_R}{dx} = 0 \quad (3.77)$$

In the present study, dW_{gas}/dx , U/dx and dE_k/dx are calculated using the pipe deformation model with the assumption that a crack propagates by dx while pipe deformation profile is unchanged; pipe deformation profile shifts parallel by dx .

Work done by gas to the pipe wall per unit length is given by;

$$\frac{dW_{\text{gas}}}{dx} = - \int_0^{x_{\text{ct}}} \int_{-\pi}^{\pi} (p(x) - p_{\text{static}}) \frac{\partial w}{\partial x} R_0 d\theta dx \quad (3.78)$$

Strain energy generated by pipe deformation behind a crack tip per unit length is given by;

$$\begin{aligned} \frac{dU}{dx} &= \int_0^{x_{\text{ct}}} \int_{-\pi}^{\pi} \left[\left(\int_0^{\varepsilon_x} \frac{\partial N_x}{\partial x} d\varepsilon_x \right) + \left(\int_0^{\gamma_{x\theta}} \frac{\partial Q_{x\theta}}{\partial x} d\gamma_{x\theta} \right) + \left(\int_0^{\kappa_\theta} \frac{\partial M_\theta}{\partial x} d\kappa_\theta \right) \right] R_0 d\theta dx \\ &= \int_{-\pi}^{\pi} \left(\int_0^{\varepsilon_x} [N_x]_{x=0}^{x=x_{\text{ct}}} d\varepsilon_x + \int_0^{\gamma_{x\theta}} [Q_{x\theta}]_{x=0}^{x=x_{\text{ct}}} d\gamma_{x\theta} + \int_0^{\kappa_\theta} [M_\theta]_{x=0}^{x=x_{\text{ct}}} d\kappa_\theta \right) R_0 d\theta \end{aligned} \quad (3.79)$$

Because $N_x = Q_{x\theta} = M_\theta = 0$ at $x = x_{\text{ct}}$, the above equation is rewritten as;

$$\frac{dU}{dx} = \int_{-\pi}^{\pi} \left(\int_0^{\varepsilon_x} N_x \Big|_{x=0} d\varepsilon_x + \int_0^{\gamma_{x\theta}} Q_{x\theta} \Big|_{x=0} d\gamma_{x\theta} + \int_0^{\kappa_\theta} M_\theta \Big|_{x=0} d\kappa_\theta \right) R_0 d\theta \quad (3.80)$$

Kinetic energy of the pipe wall and the surrounding water per unit length is given by;

$$\begin{aligned} \frac{dE_k}{dx} &= \int_0^{x_{\text{ct}}} \int_{-\pi}^{\pi} \frac{\partial}{\partial x} \left\{ \frac{1}{2} \rho_{\text{pipe}} \left[\left(\frac{\partial v}{\partial t} \right)^2 + \left(\frac{\partial w}{\partial t} \right)^2 \right] + \frac{1}{2} \rho_{\text{add}} \left(\frac{\partial w}{\partial t} \right)^2 \right\} R_0 d\theta dx \\ &= \int_{-\pi}^{\pi} \left\{ \frac{1}{2} \rho_{\text{pipe}} \left[\left(\frac{\partial v}{\partial t} \Big|_{x=0} \right)^2 + \left(\frac{\partial w}{\partial t} \Big|_{x=0} \right)^2 \right] + \frac{1}{2} \rho_{\text{add}} \left(\frac{\partial w}{\partial t} \Big|_{x=0} \right)^2 \right\} R_0 d\theta \end{aligned} \quad (3.81)$$

Strain energy generated by crack tip singularity ahead of a crack tip per unit length dU_R/dx corresponds to J resistance which is well known in fracture mechanics. Hereafter, dU_R/dx is written as J_R . J_R is obtained from some experimental measurements conducted by Aihara et al.[51]. According to Reference [51], J_R is obtained by measuring the propagation energy of drop weight tear tests and plastic deformation exhibited on

the fractured pipes of full-scale burst tests on X65 pipes, and increases with increasing crack velocity V as follows;

$$\frac{dU_R(V)}{dx} = J_R(V) = J_R(V = 0) \left[1 + 38.8 \left(\frac{V}{250} \right)^3 \right] \quad (3.82)$$

where, $J_R(V = 0)$ is strain energy ahead of a crack tip under the quasi-static condition; in the present study, $J_R(V = 0)$ is expressed as;

$$J_R(V = 0) = h \cdot DWTT_{pre} \quad (3.83)$$

where, h is pipe thickness and $DWTT_{pre}$ is absorbed energy of pre-cracked drop weight tear test on an interested pipe. $DWTT_{pre}$ can be converted from Charpy impact energy C_V using the empirical equation[52];

$$DWTT_{pre}[J] = 3.29 (h[\text{mm}]10^3)^{1.5} C_V[\text{J}/\text{mm}^2]^{0.544} \quad (3.84)$$

In the calculation, the crack propagation condition is given by;

$$\frac{dW_{gas}}{dx} - \frac{dU}{dx} - \frac{dE_k}{dx} \geq J_R(V) \quad (3.85)$$

$$V = \frac{\Delta x}{n_0 \Delta t} \quad (3.86)$$

where, n_0 is number of time steps while the crack is judged no to propagate.

3.6 Calculation flow

Figure 3.14 shows the flowchart of the UT offshore model. First, pipe deformation is calculated, and then crack propagation by Δx is judged. Next, whether or not the crack is arrested is judged; in the present study, the crack is judged to be arrested if no further pipe deformation occurs. If the crack is judged not to be arrested, gas decompression and bubble growth are solved by using calculated pipe deformation profile which is related to gas outflow from the crack opening to the bubble. Finally, time step Δt is added. Repeating this procedure gives whole behavior of unstable ductile crack in offshore pipelines, where coupled phenomenon are considered; UT offshore model is weak two-way coupling model.

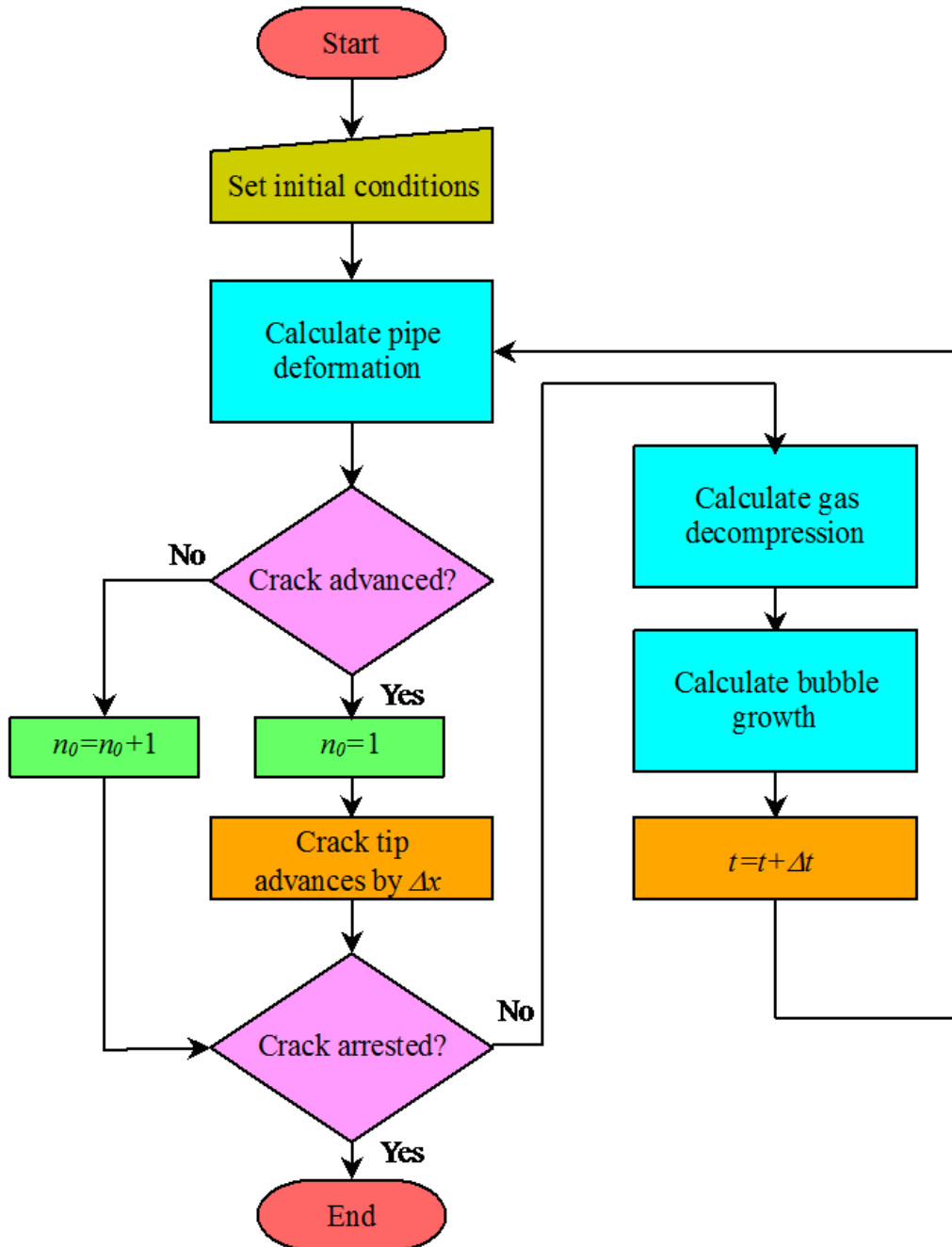


Fig. 3.14 Calculation flow chart

3.7 An example of calculation result

In the present section, in order to demonstrate how the UT offshore model works and predicts the unstable ductile crack propagation behavior in offshore pipelines briefly, an example of calculated result is presented.

Table 3.1 shows calculation conditions. Note that very low Charpy absorbed energy is assumed for realizing long propagation intentionally. Incremental length Δx and time step size Δt are set to 20mm and $5\mu s$, respectively.

Calculation time was around 1 hour. Figure 3.15 shows the calculated history of crack propagation. Figure 3.16 to Fig. 3.18 show 3D view of pipe deformation and crack propagation, showing pressure value inside the pipe by colors. Figure 3.19 to Fig. 3.21 show 3D view of bubble growth, showing bubble pressure value by colors. Note that the tip of the bubble moves as the crack tip propagates. Figure 3.22 to Fig. 3.23 show histories of pressure and flow rate distribution inside a pipe. Figure 3.24 to Fig. 3.25 show histories of pressure and flow rate distribution inside a bubble. Figure 3.26 to Fig. 3.27 show histories of bubble radius and growth rate distribution.

The UT offshore model is able to calculate time histories of pipe deformation, gas decompression, bubble growth and crack propagation considering the interactions among them. The validation of the UT offshore model is described in the Chap.4 and Chap.5.

Table 3.1 Calculation condition

Medium	Air
Initial pressure (MPa)	15.7
Temperature (° C)	15
Outer diameter (inch)	36
Pipe thickness (mm)	20.8
Pipe density (kg/m ³)	7860
Pipe length (m)	108
Tensile yield strength (MPa)	413
Grade	X60
Charpy absorbed energy (J/cm ²)	6
Initial crack length (inch)	36
Water depth (m)	30
Water density (kg/m ³)	1000
Water dynamic viscosity (m ² /s)	1.0×10^{-6}
Water surface tension (N/m)	72.75×10^{-3}
Software for isentropic process	GASDECOM
Δx (mm)	20
Δt (μ s)	5

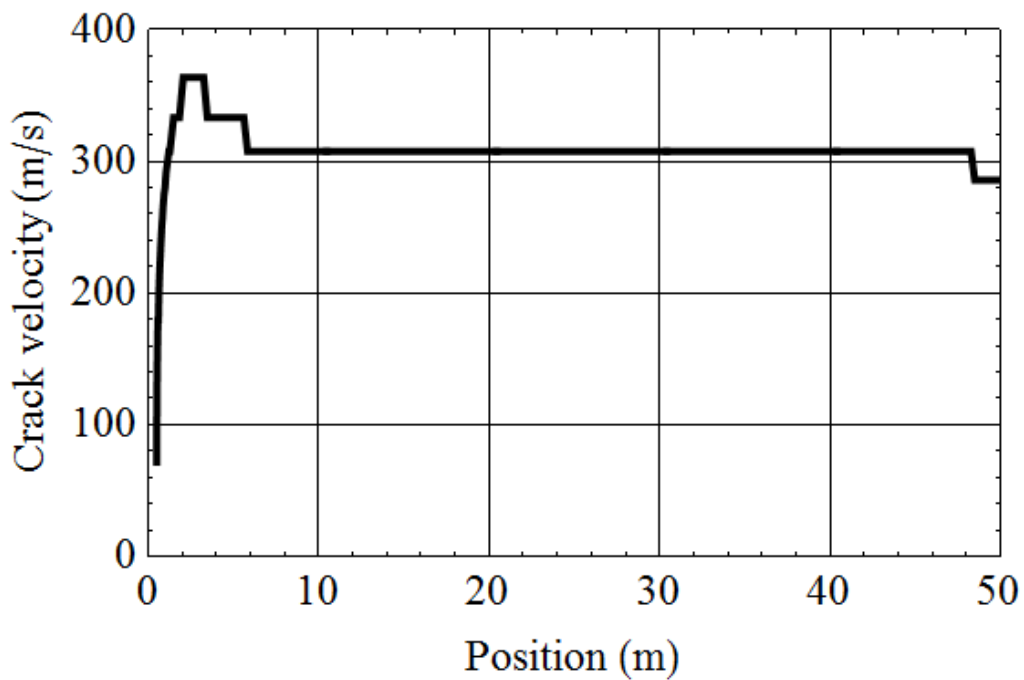


Fig. 3.15 Crack tip position versus crack velocity

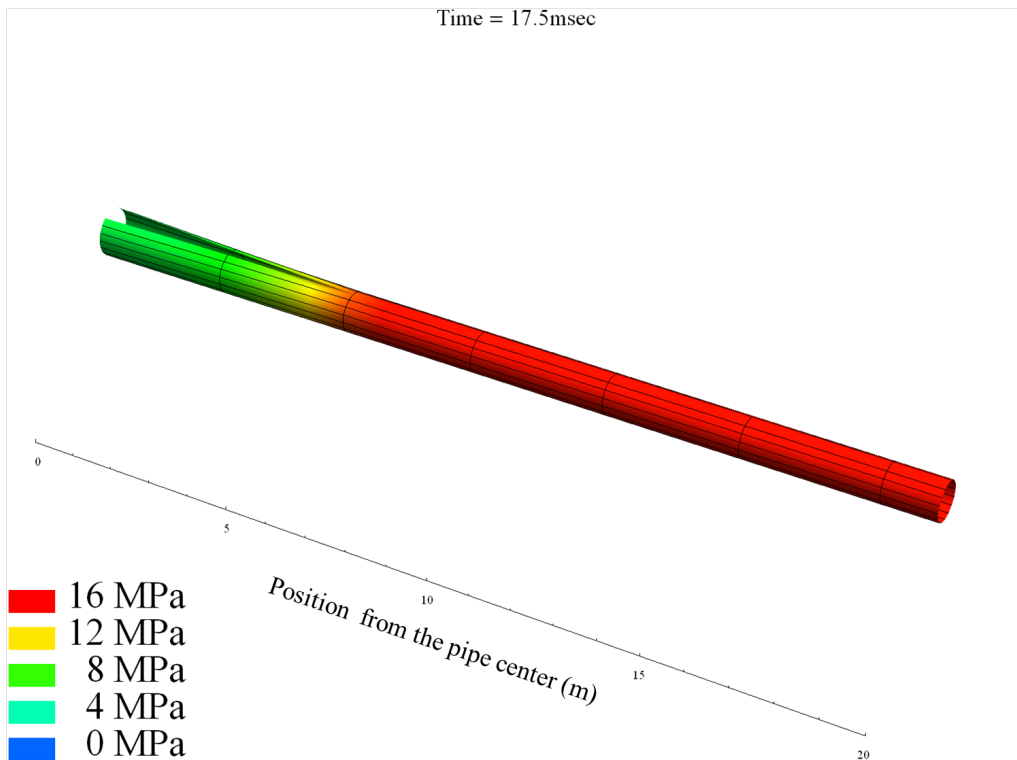


Fig. 3.16 3D pipe view at 17.5ms

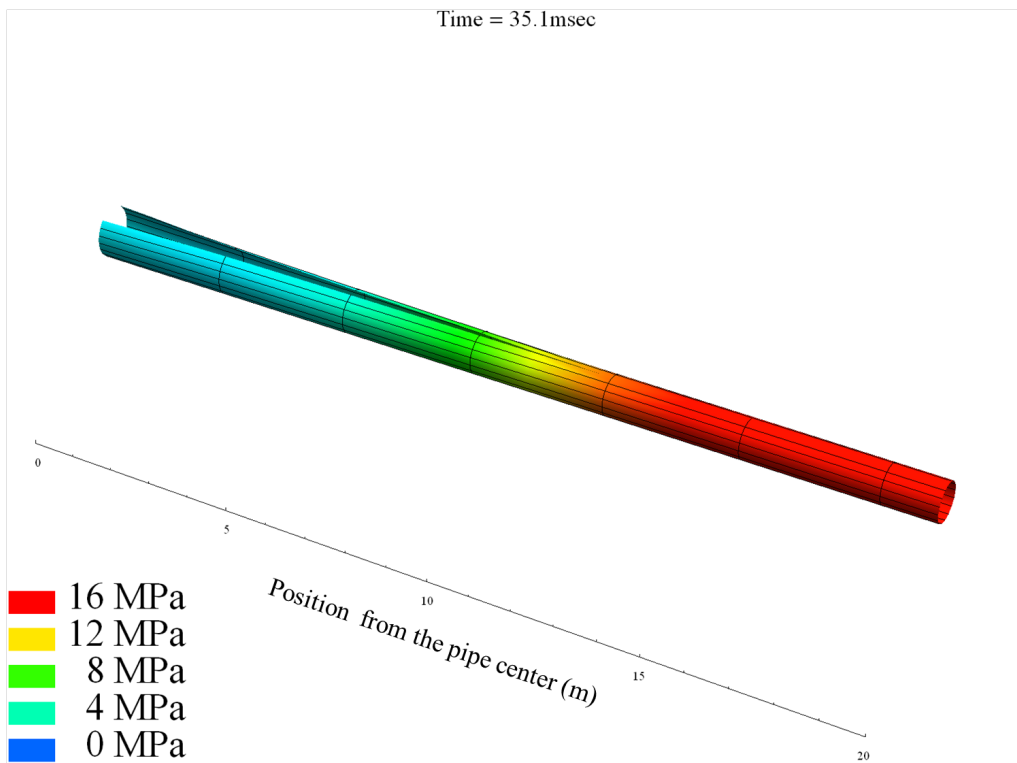


Fig. 3.17 3D pipe view at 35.1ms

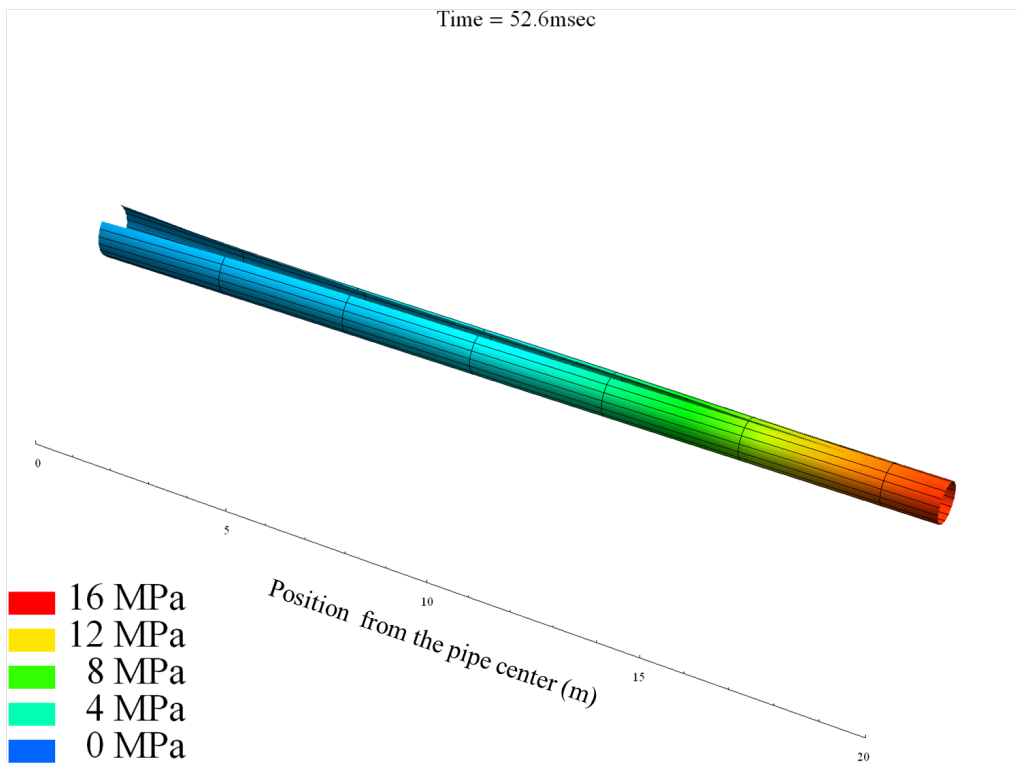


Fig. 3.18 3D pipe view at 52.6ms

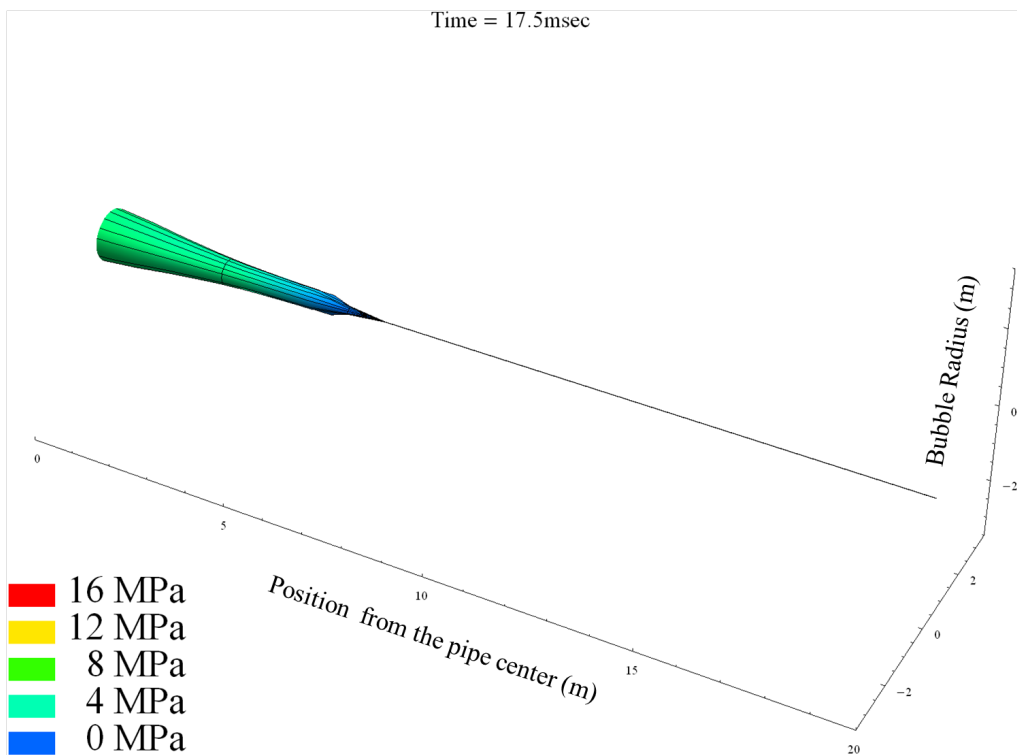


Fig. 3.19 3D bubble view at 17.5ms

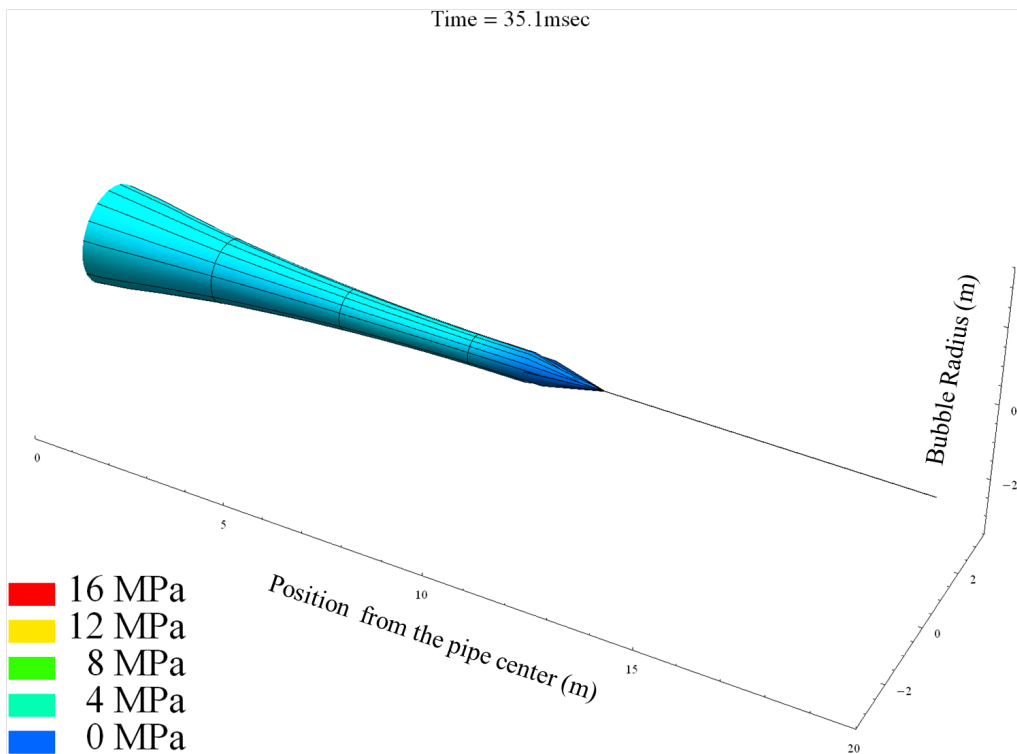


Fig. 3.20 3D bubble view at 35.1ms

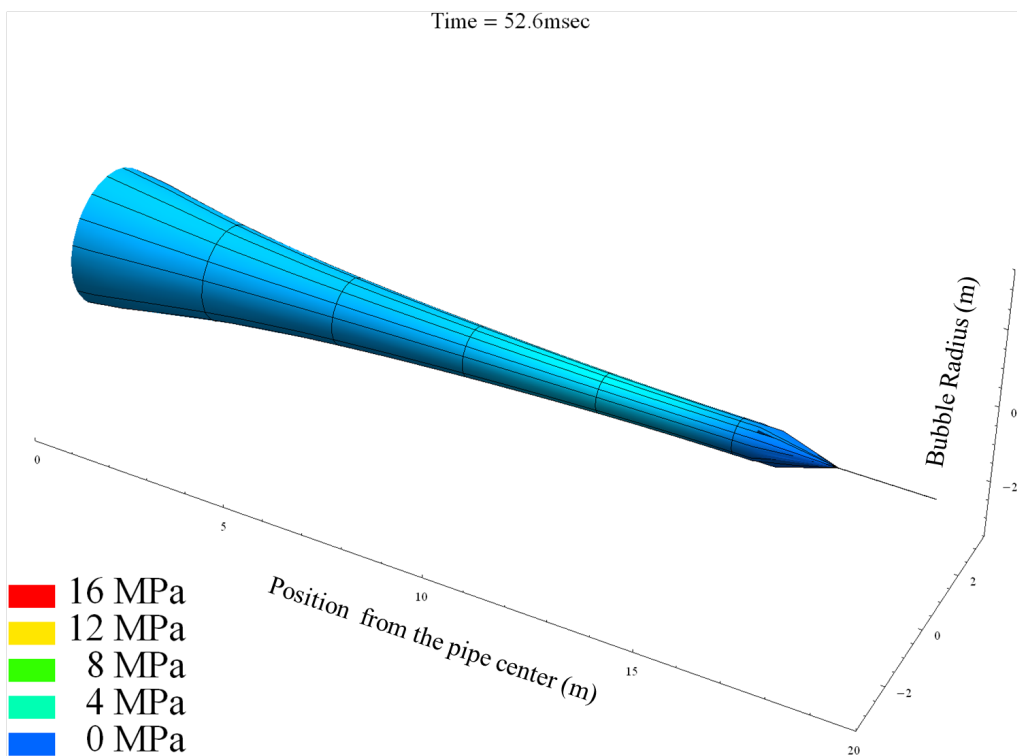


Fig. 3.21 3D bubble view at 52.6ms

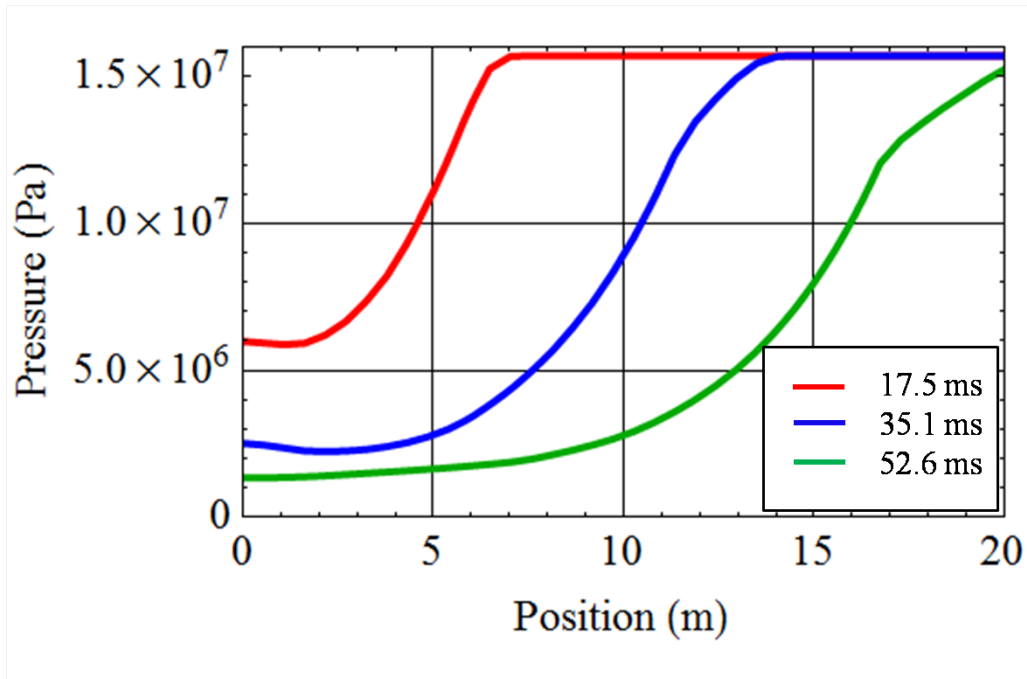


Fig. 3.22 History of pressure distribution inside a pipe at each time

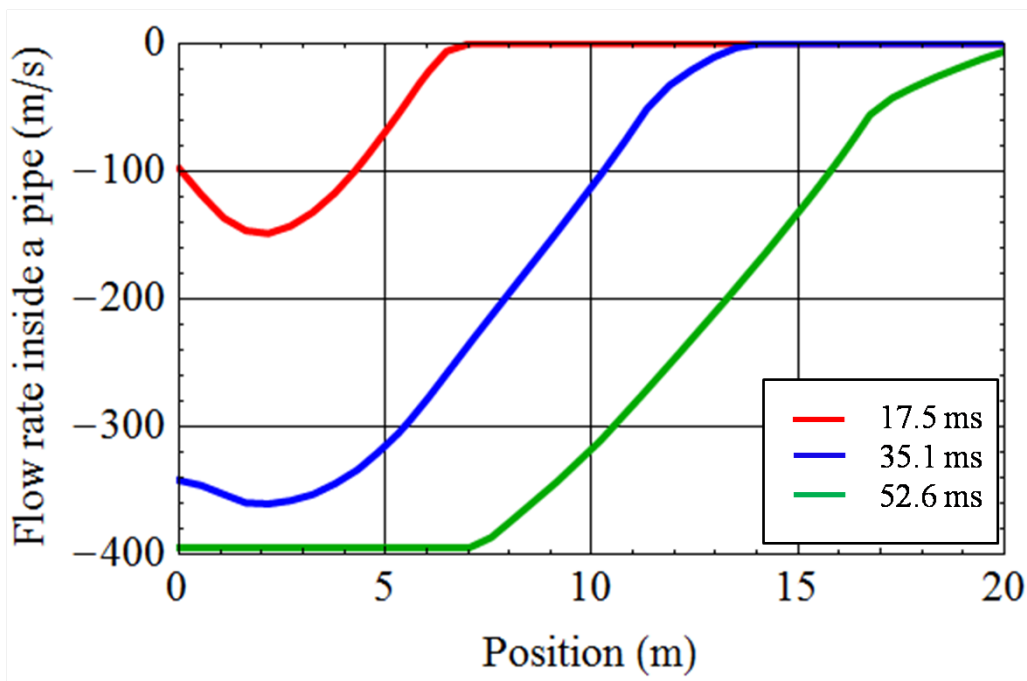


Fig. 3.23 History of flow rate distribution inside a pipe at each time

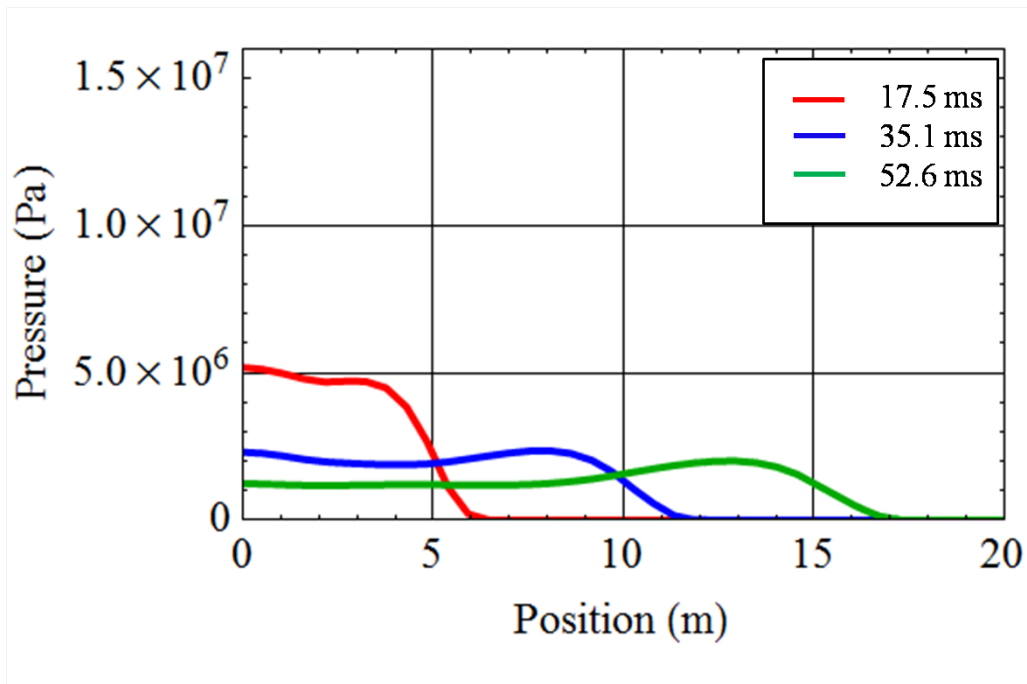


Fig. 3.24 History of bubble pressure distribution at each time

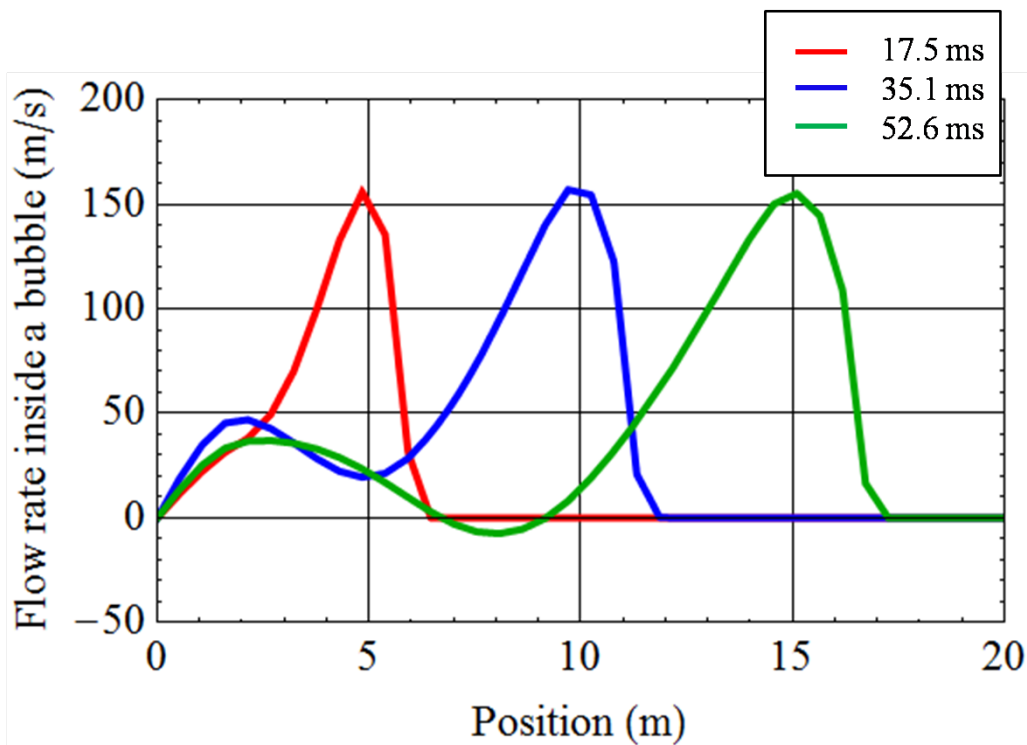


Fig. 3.25 History of flow rate distribution in a bubble at each time

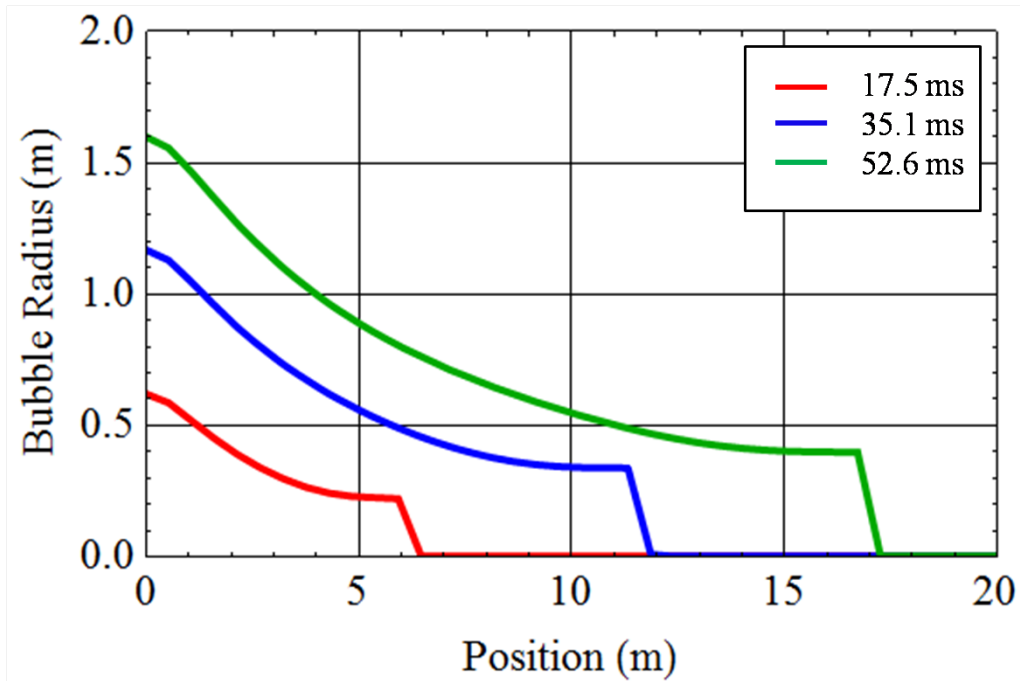


Fig. 3.26 History of bubble radius distribution at each time

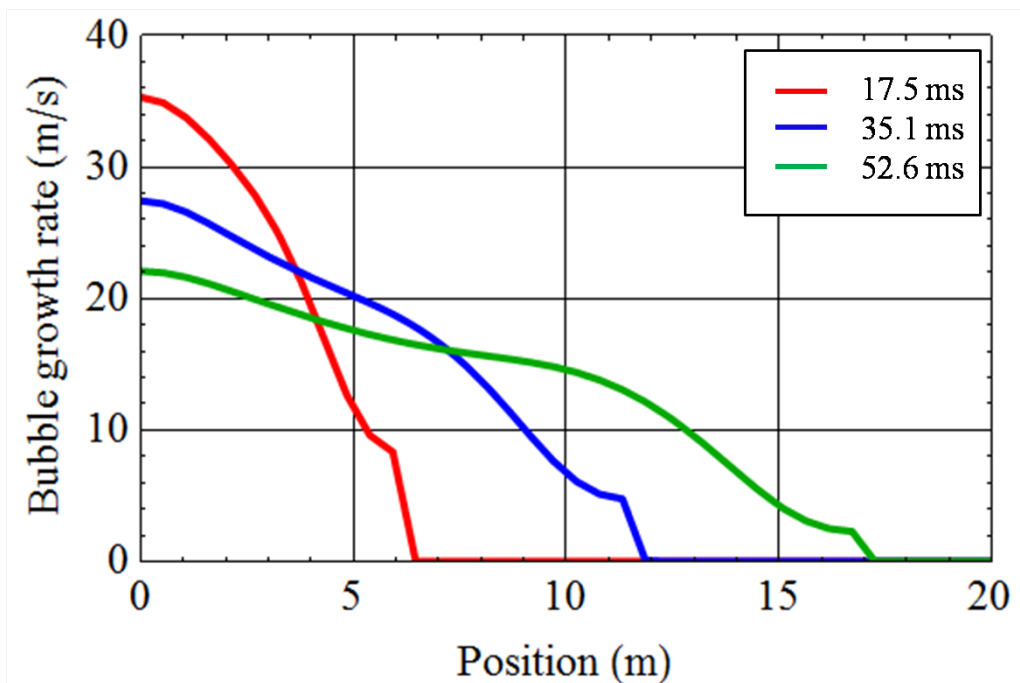


Fig. 3.27 History of bubble growth rate distribution at each time

3.8 Summary

- Pipe deformation model described by a single parameter is presented.
- Water backfill effect is formulated as an added density effect
- Gas decompression is modeled as one-dimensional compressible gas flow under isentropic condition
- Bubble growth is modeled as one-dimensional compressible gas flow with increasing cross sectional area under isentropic condition
- Crack propagation condition is based on the dynamic energy balance, where strain energy behind and ahead of a crack tip, work done by gas to the pipe wall and kinetic energy of the pipe wall are considered.
- Calculation flow is introduced.
- An example of calculation result is presented.

Chapter 4

Underwater rupture tests

For the validation of the bubble growth model in the UT offshore model, the author conducted underwater rupture test using aluminum pipes with water depth of 1m. In the tests, bubble growth behavior was observed by high-speed camera which filmed with 5,000fps. Also, history of internal and external pressure were measured by pressure transducers. The detailed description of the tests is below.

4.1 Testing conditions

Table 4.1 shows the testing conditions. Two pure aluminum pipes, whose grade are AL1070 according to JIS-Z3232, with surface notch were pressurized by pure nitrogen until the pipes bursted at particular pressure. Note that the notch length for No.1 was longer than that for No.2. The thickness of the pipes were originally 3mm, but was reduced to particular thickness as shown in Fig. 4.1. Geometry of surface notches is shown in Fig. 4.2. The depth of surface notches was determined by the following empirical equation so that the pipes burst at around 1MPa.

$$\sigma_{hc} = \sigma_0 \frac{1 - d/h}{1 - d/(hM_T)} \quad (4.1)$$

$$M_T = (1 + 1.255\lambda^2 - 0.0135\lambda^4)^{1/2} \quad (4.2)$$

$$\lambda = \frac{c}{\sqrt{Rh}} \quad (4.3)$$

where, σ_{hc} is critical circumferential stress at the leak, h is pipe thickness, d is surface notch depth and c is half notch length. M_T is referred to as

bulging factor[17]. σ_0 is yield stress, which is assumed to be 100MPa in the present calculation.

The pipes were laid inside the water tank, see Fig. 4.3 and Fig. 4.4. The bottom of the water tank is 2m by 1.5m, and the height is 2m. Four circular windows were designed for high-speed cameras and lighting, see Fig. 4.5. The water tank with stiffeners was designed based on elastic design against pressure waves generated by the burst using finite element analysis. The water depth was set to 1m throughout the present tests. Tested pipes were fixed on the mount as shown in Fig. 4.6 so that the pipes should be stable during the burst.

The two high-speed cameras were set close to the windows to capture both of side and axial view, see Fig. 4.7 and Fig. 4.8. Filming rate was 5,000fps throughout the tests.

Three pressure transducers were introduced to measure the histories of static and dynamic internal pressure and the history of dynamic external pressure. Their locations are shown in Fig. 4.1.

The summary of the pressurizing system and measurement instruments is shown in Fig. 4.9.

Figure 4.10 to Fig. 4.12 are photographs during the tests.

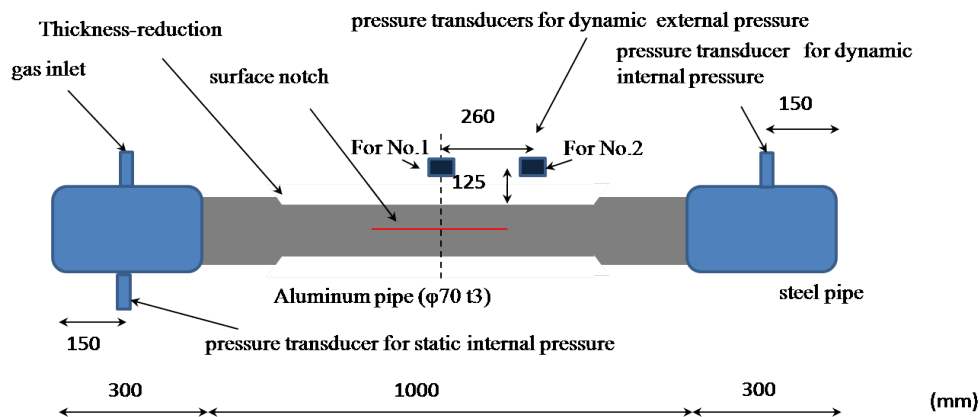


Fig. 4.1 Tested pipe arrangement, top view

surface notch



Inside a pipe

Fig. 4.2 Surface notch geometry

Table 4.1 Testing condition

No.	Grade	Diameter (mm)	Original thickness (mm)	Reduced thickness (mm)	Notch length (mm)	Notch depth (mm)	Gas	Water depth (m)
1	AL1070	70	3	1.00	300	0.75	N ₂	1
2				0.45	100	0.15		



Fig. 4.3 Water tank



Fig. 4.4 Water tank

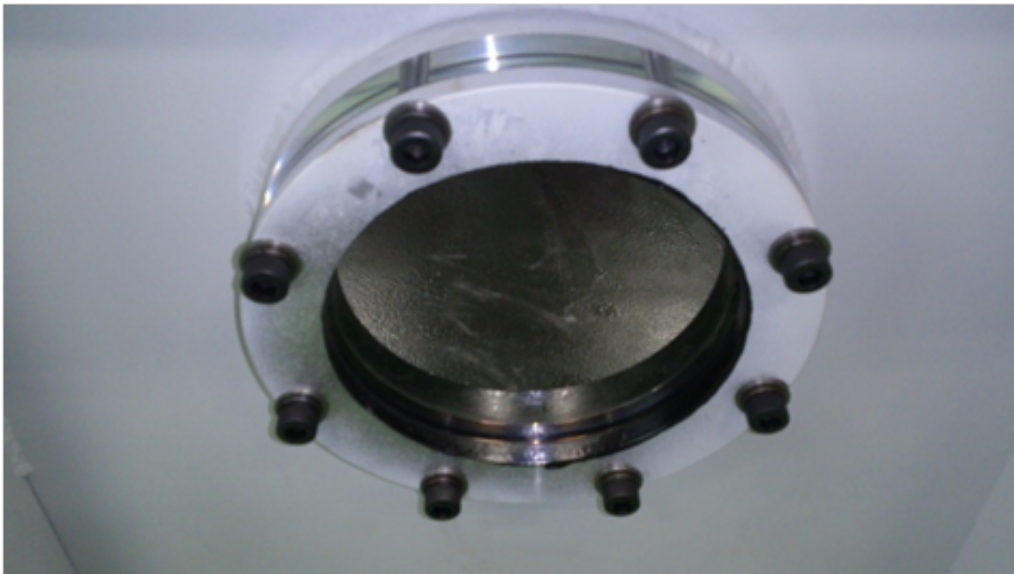


Fig. 4.5 Window for high-speed camera and lighting

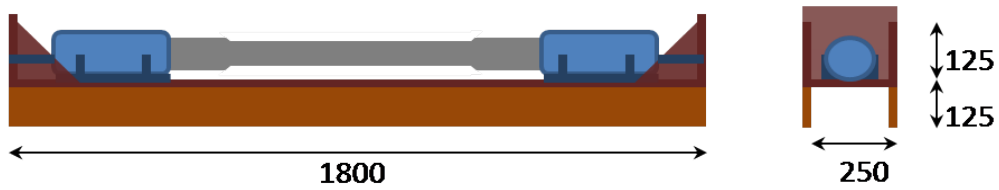


Fig. 4.6 Tested pipe setting



Fig. 4.7 High-speed camera and lighting



Fig. 4.8 Photo of the test

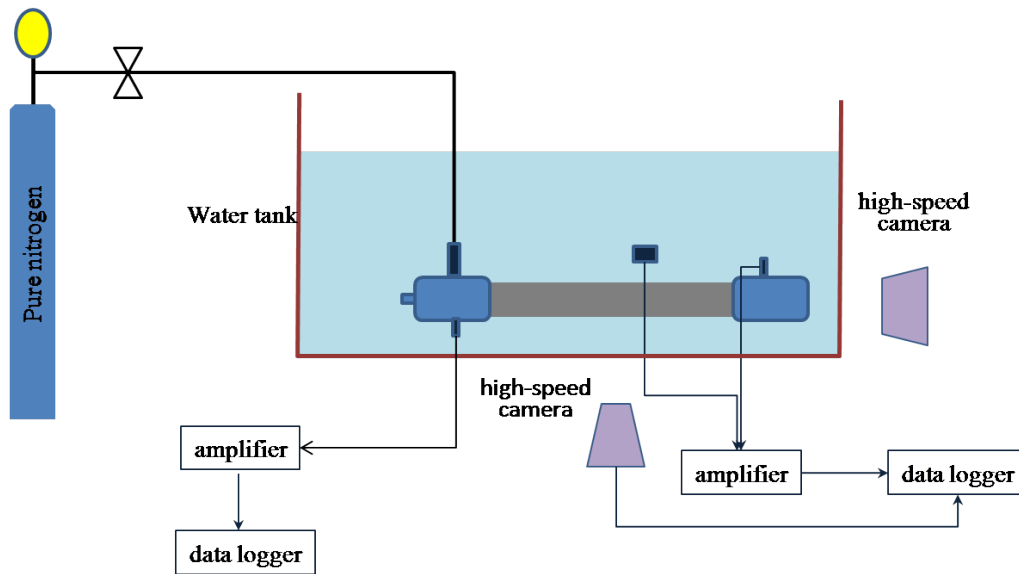


Fig. 4.9 Pressurizing system and instruments for measurements

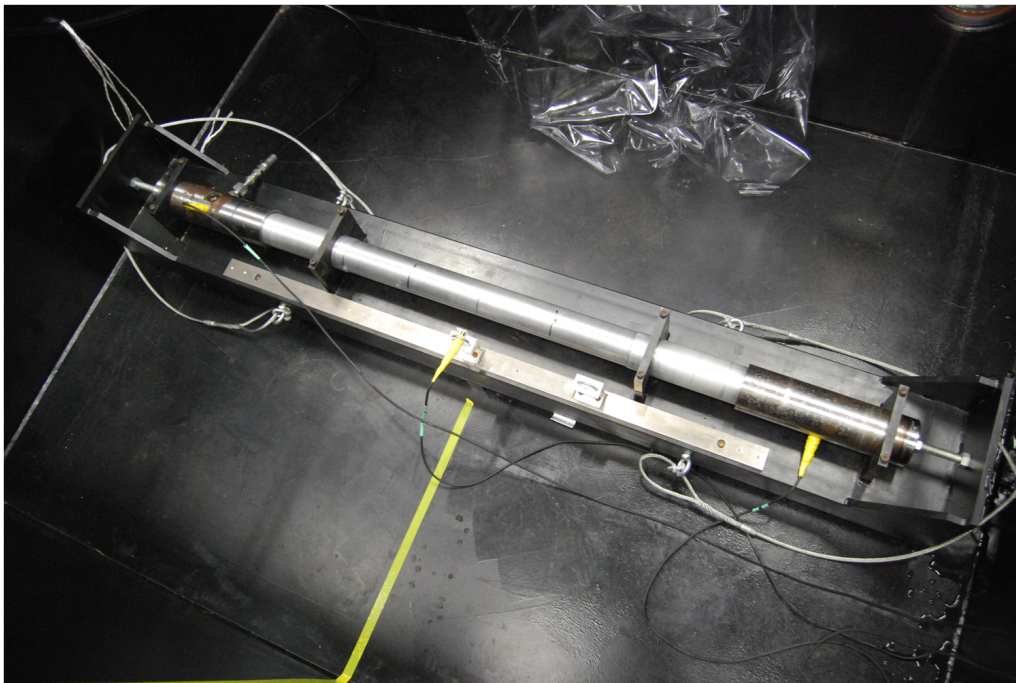


Fig. 4.10 Photo of pipe setting

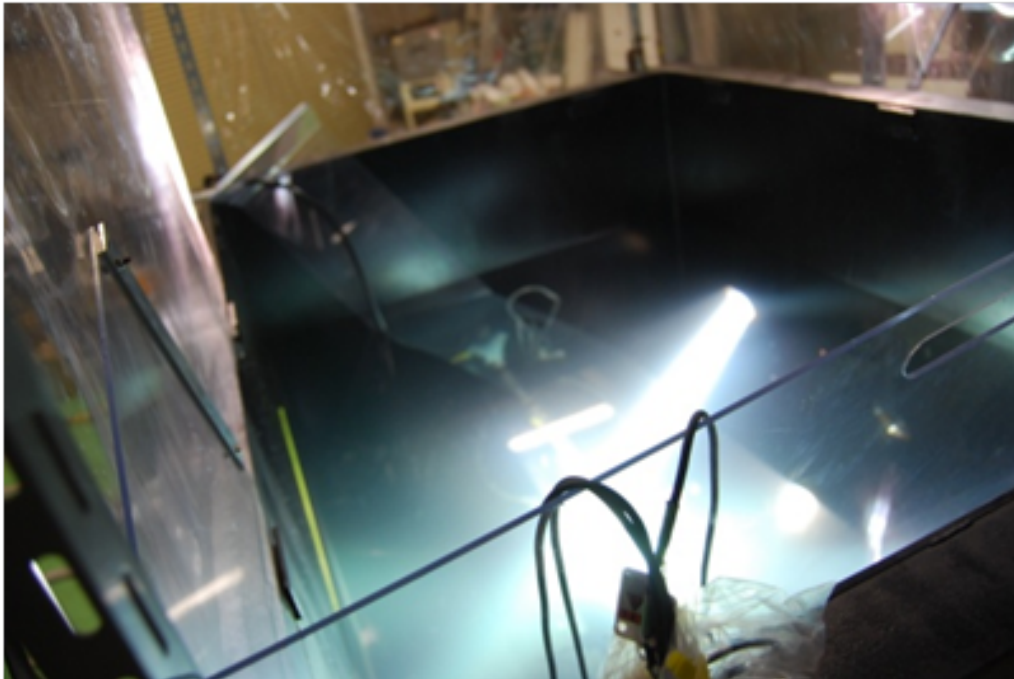


Fig. 4.11 Photo during the test

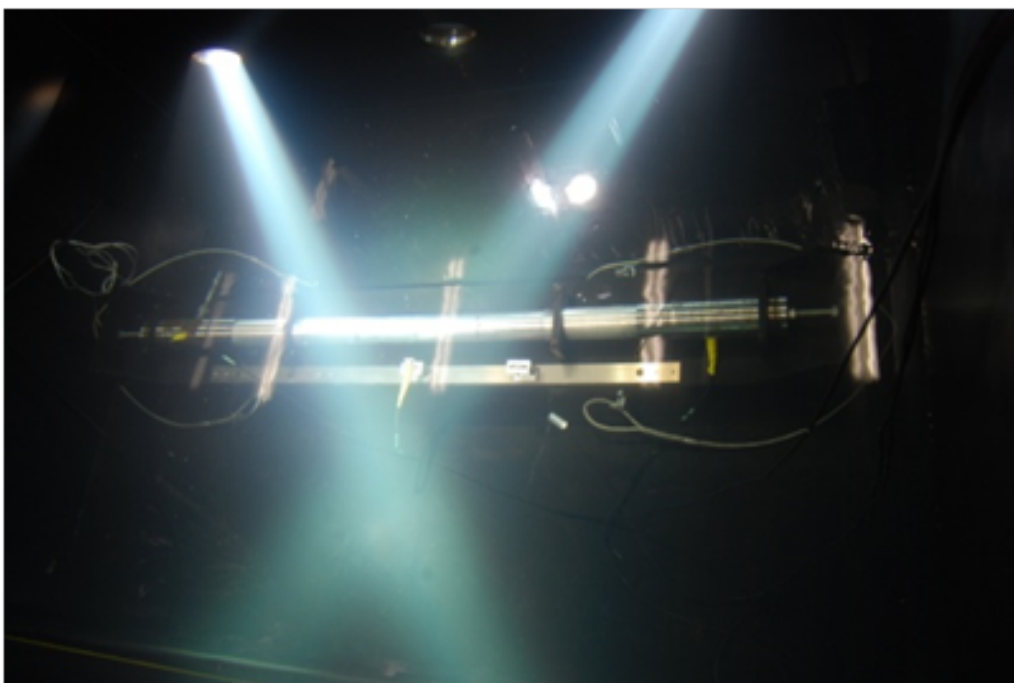


Fig. 4.12 Photo of the tested pipe in the water

4.2 Test results

4.2.1 Overview of the results

Figure 4.13 shows fractured pipe in the water for No.1. The fractured pipes after the burst are shown in Fig. 4.14 and Fig. 4.15. For the both tests, the cracks deviated to the circumferential direction at the tip of the surface notches; the cracks did not propagate to the axial direction beyond the tip of the surface notches.

The burst pressures were 0.95MPa and 1.31MPa as shown in Table 4.2, respectively, which were around the intended pressure, 1MPa. The histories of dynamic internal and external pressures were successfully measured and are shown in Fig. 4.16 and Fig. 4.17. For the test No.1, external pressure transducer was attached at closer position to the pipe center shown in Fig. 4.1. On the other hand, for the test No.2, external pressure transducer was attached at farther position from the pipe center shown in Fig. 4.1. Sudden increase in internal pressure as shown in Fig. 4.16 is regarded as measurement error.

The behaviors of the bubble growth were also successfully captured by high-speed camera. Fig. 4.18 to Fig. 4.41 show side and axial views of the bubble profile at each time. Because the cross sectional shape is circular as seen in axial views, the assumption that the bubble growth can be described by cylindrical coordinate system in the bubble growth modeling is reasonable. The detailed understandings on the histories of the bubble growth are described in the next subsection.

Table 4.2 Pressure(MPa) at the rupture

No.1	0.95
No.2	1.31

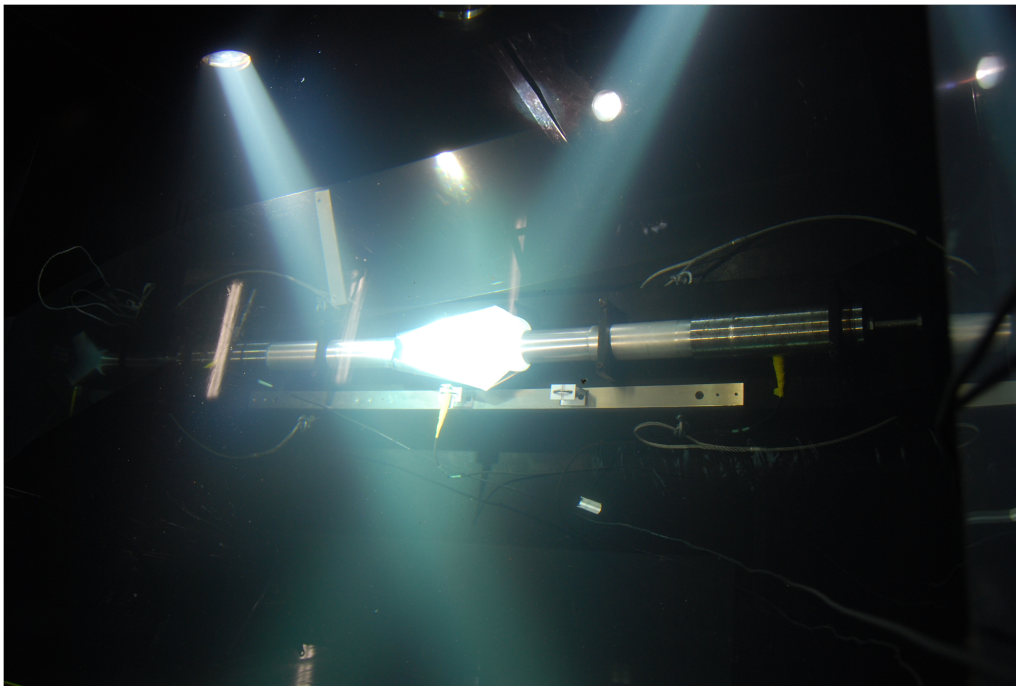


Fig. 4.13 Photo of tested pipe after the burst for No.1

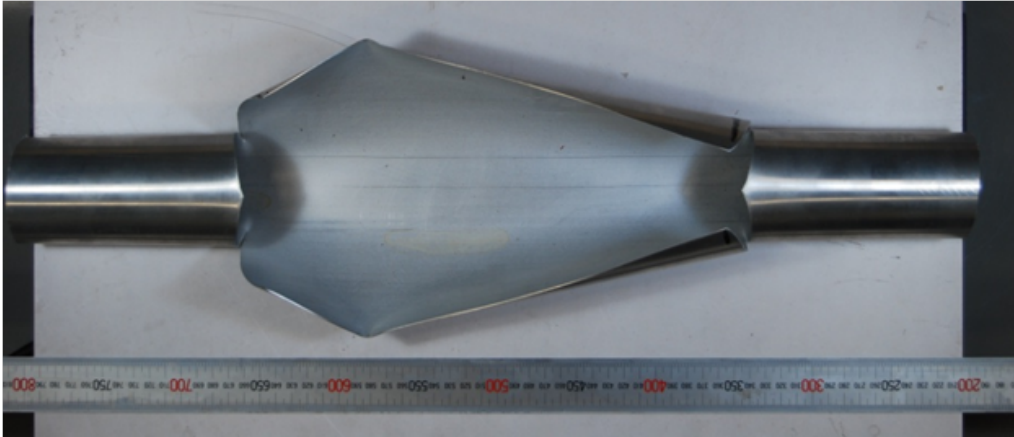


Fig. 4.14 Fractured tested pipe for No.1



Fig. 4.15 Fractured tested pipe for No.2

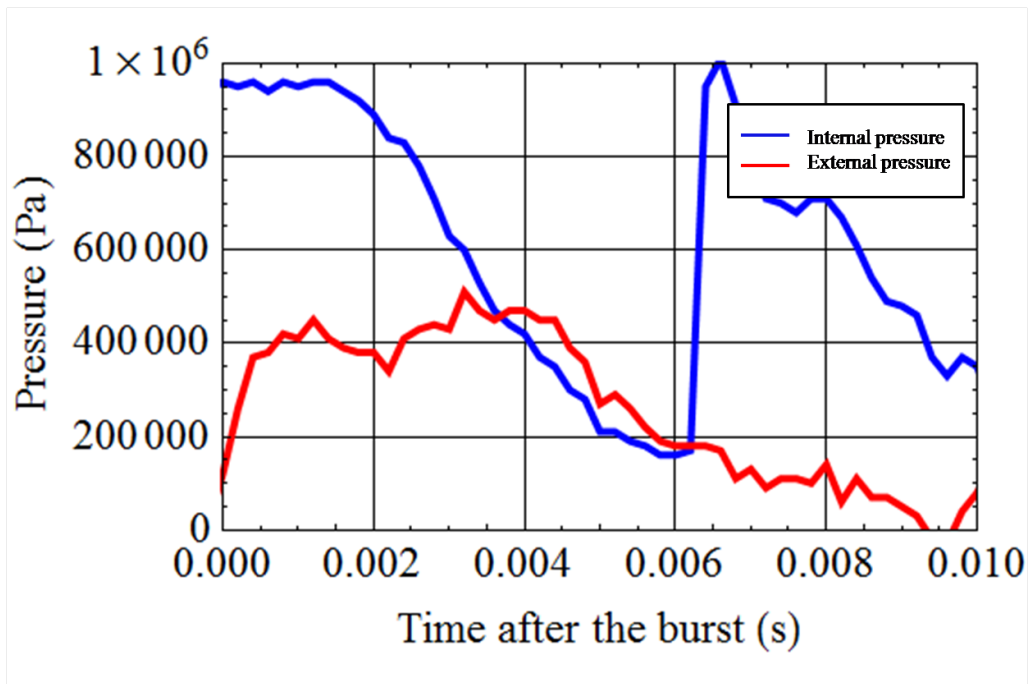


Fig. 4.16 Time histories of dynamic internal and external pressure for No.1

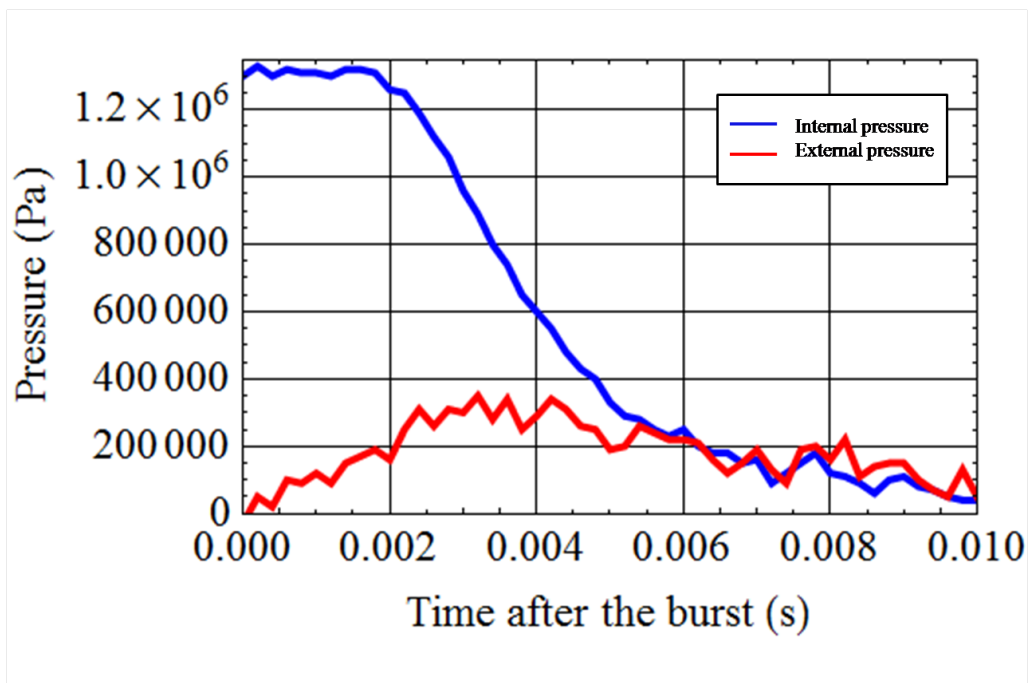


Fig. 4.17 Time histories of dynamic internal and external pressure for No.2

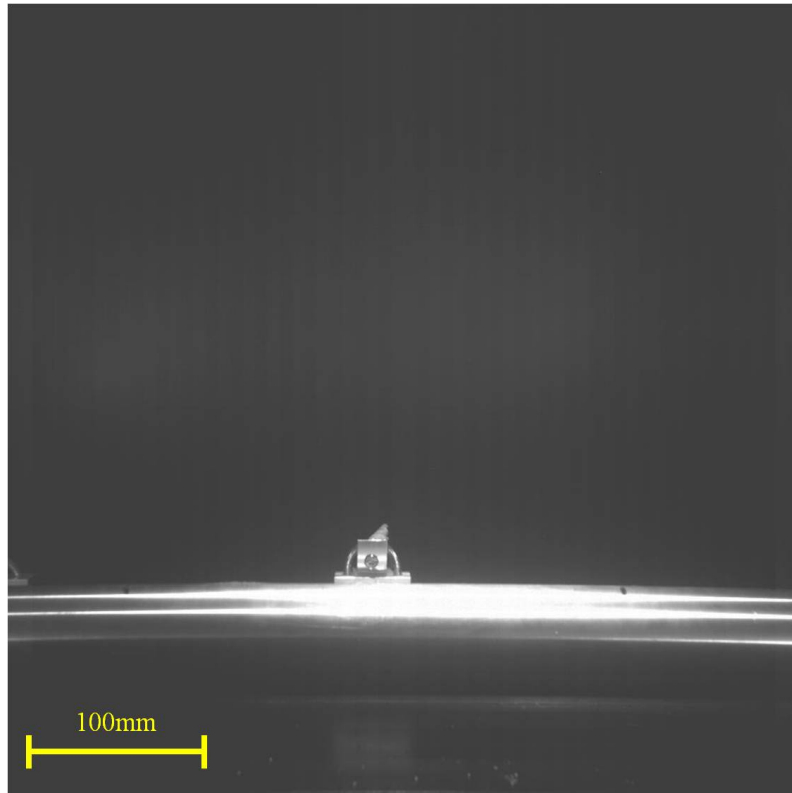


Fig. 4.18 Bubble profile at 0ms after the burst for No.1, side view

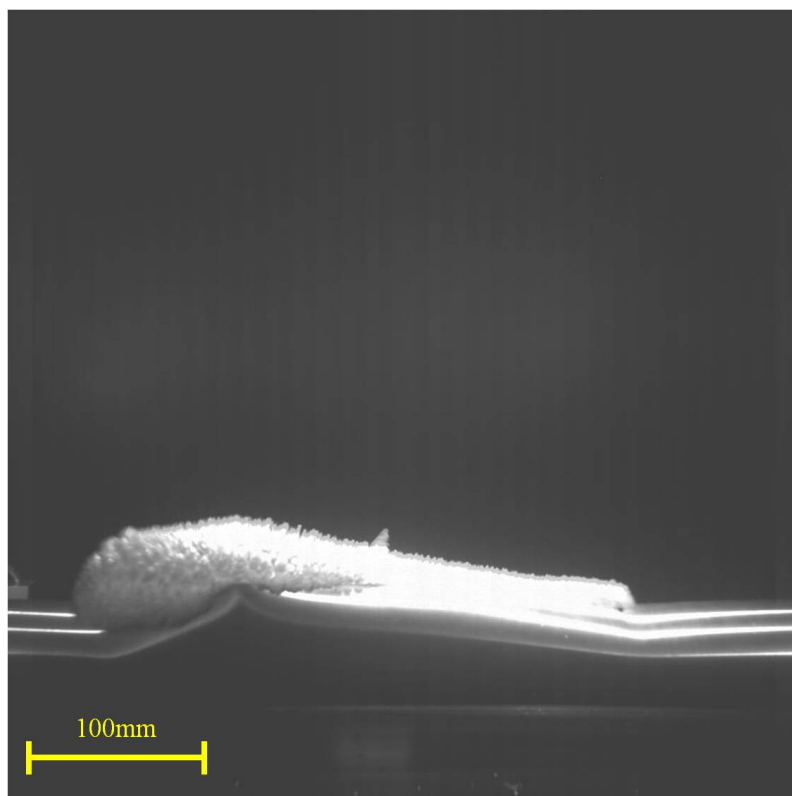


Fig. 4.19 Bubble profile at 2ms after the burst for No.1, side view

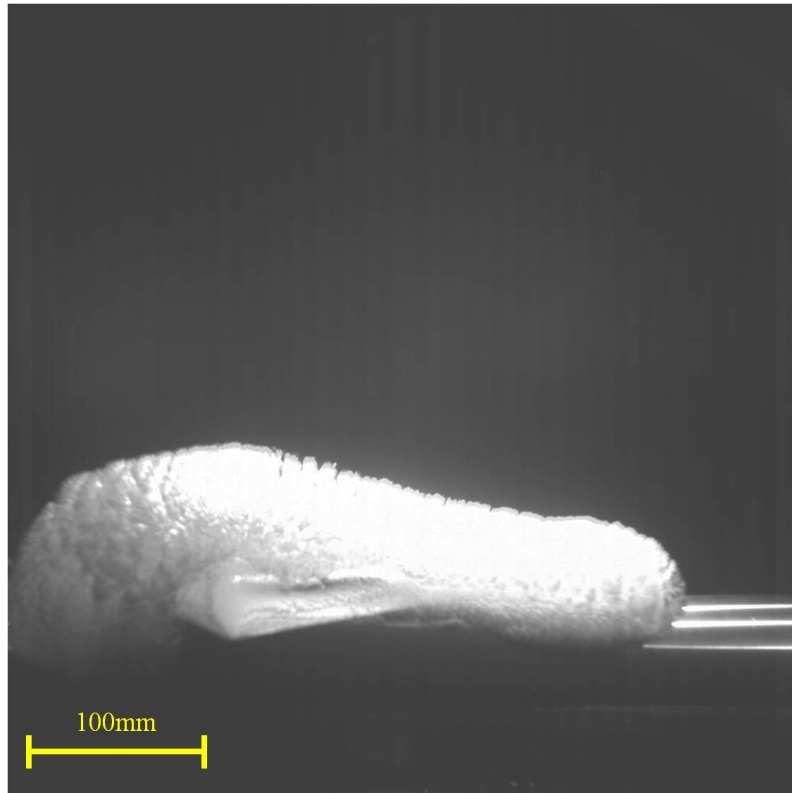


Fig. 4.20 Bubble profile at 4ms after the burst for No.1, side view

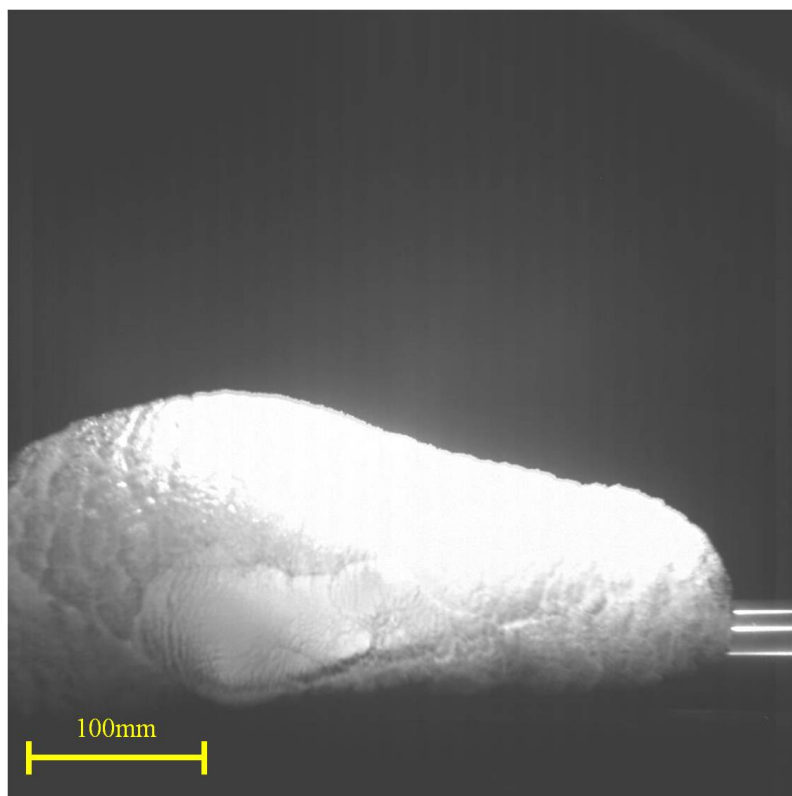


Fig. 4.21 Bubble profile at 6ms after the burst for No.1, side view

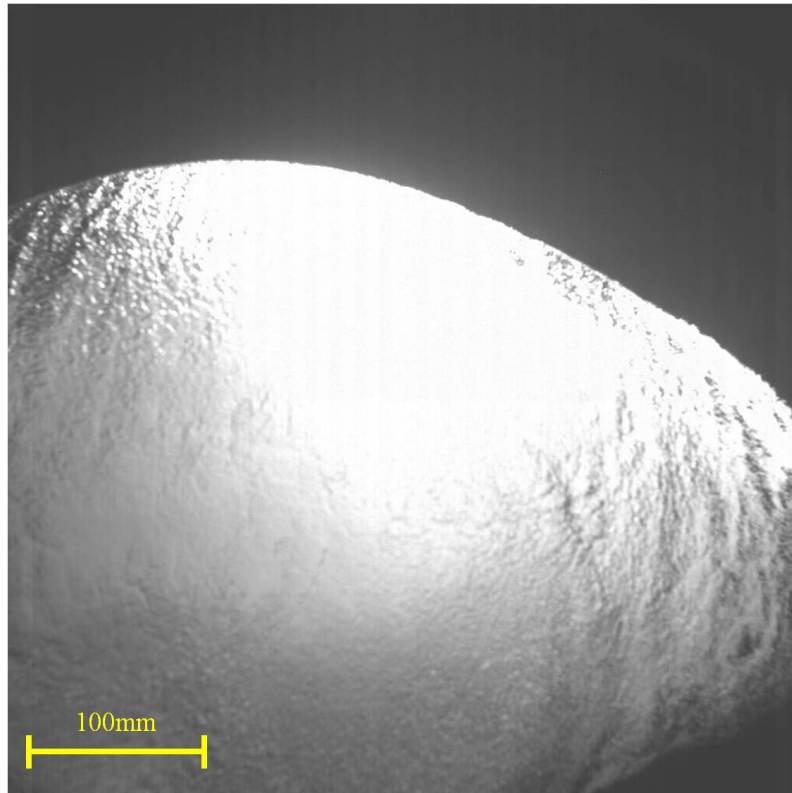


Fig. 4.22 Bubble profile at 20ms after the burst for No.1, side view

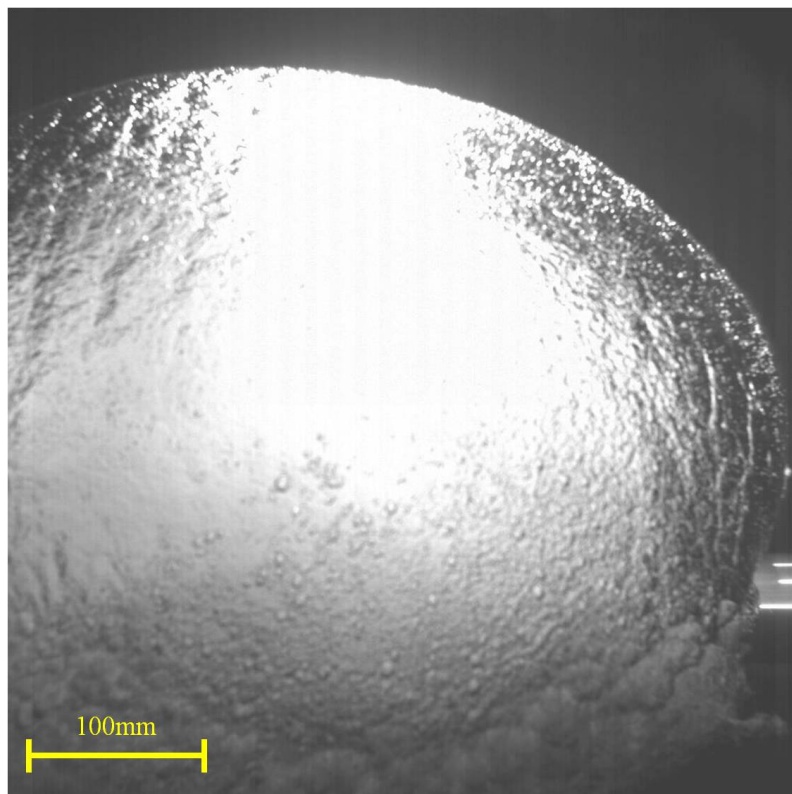


Fig. 4.23 Bubble profile at 40ms after the burst for No.1, side view

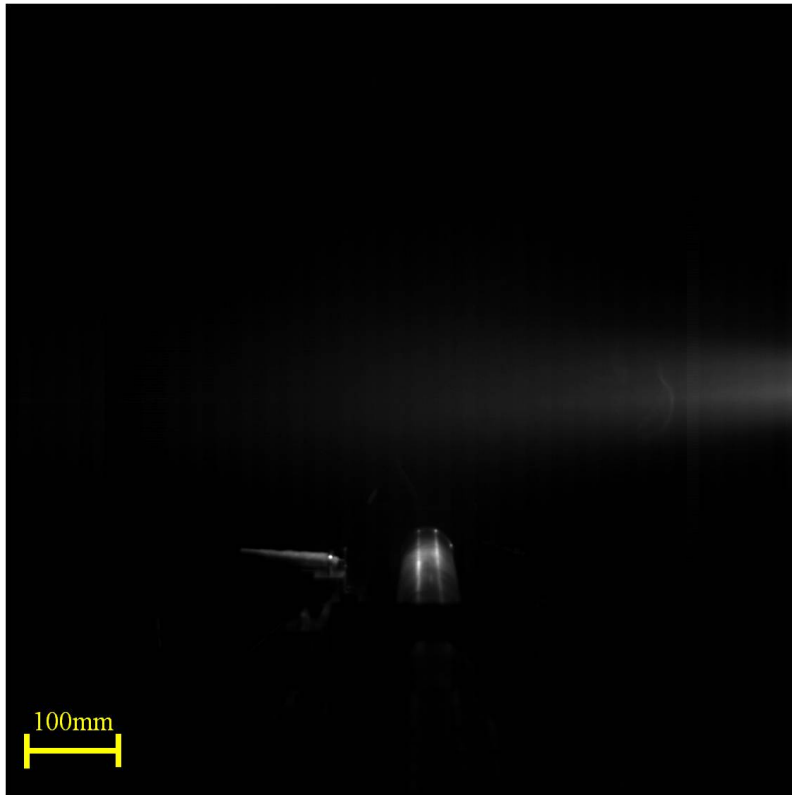


Fig. 4.24 Bubble profile at 0ms after the burst for No.1, axial view

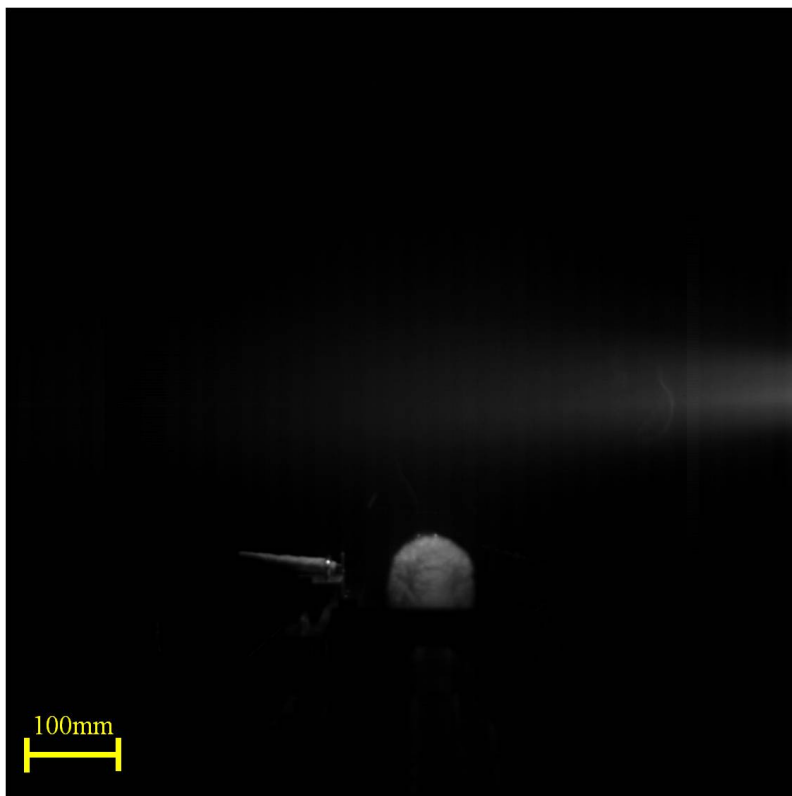


Fig. 4.25 Bubble profile at 2ms after the burst for No.1, axial view

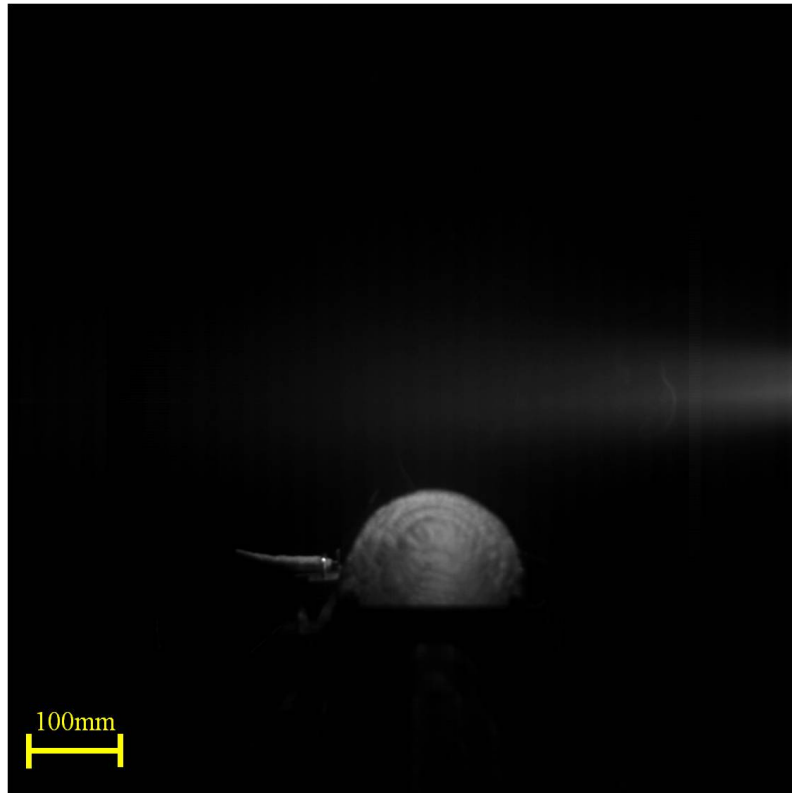


Fig. 4.26 Bubble profile at 4ms after the burst for No.1, axial view

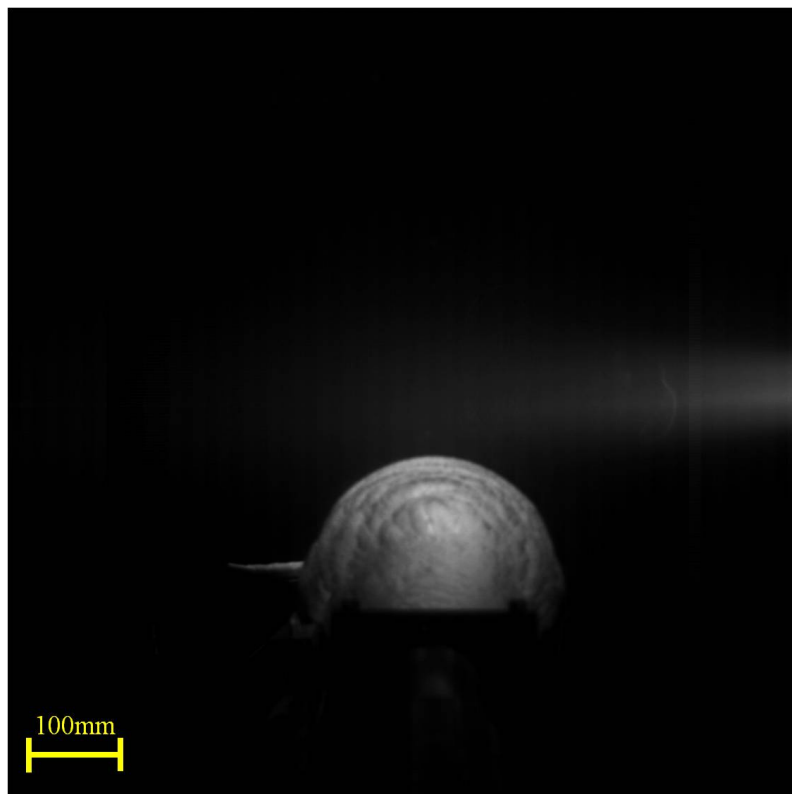


Fig. 4.27 Bubble profile at 6ms after the burst for No.1, axial view

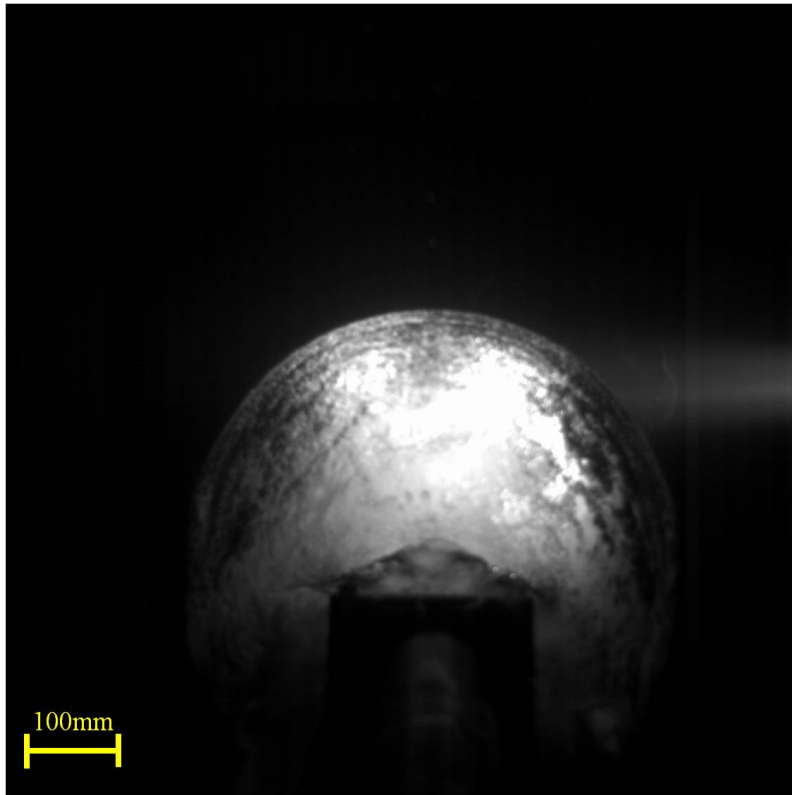


Fig. 4.28 Bubble profile at 20ms after the burst for No.1, axial view

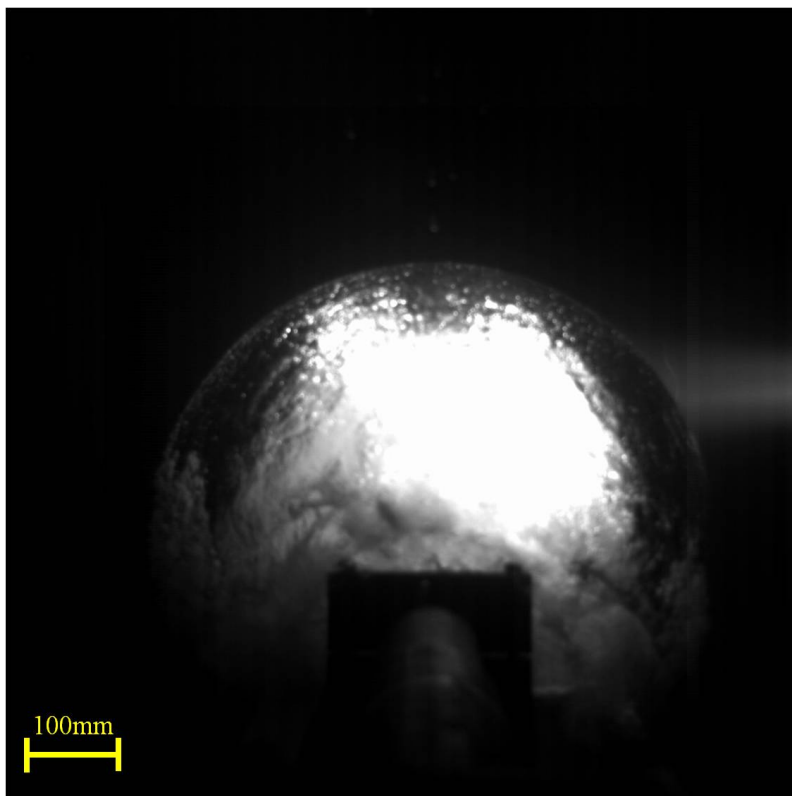


Fig. 4.29 Bubble profile at 40ms after the burst for No.1, axial view

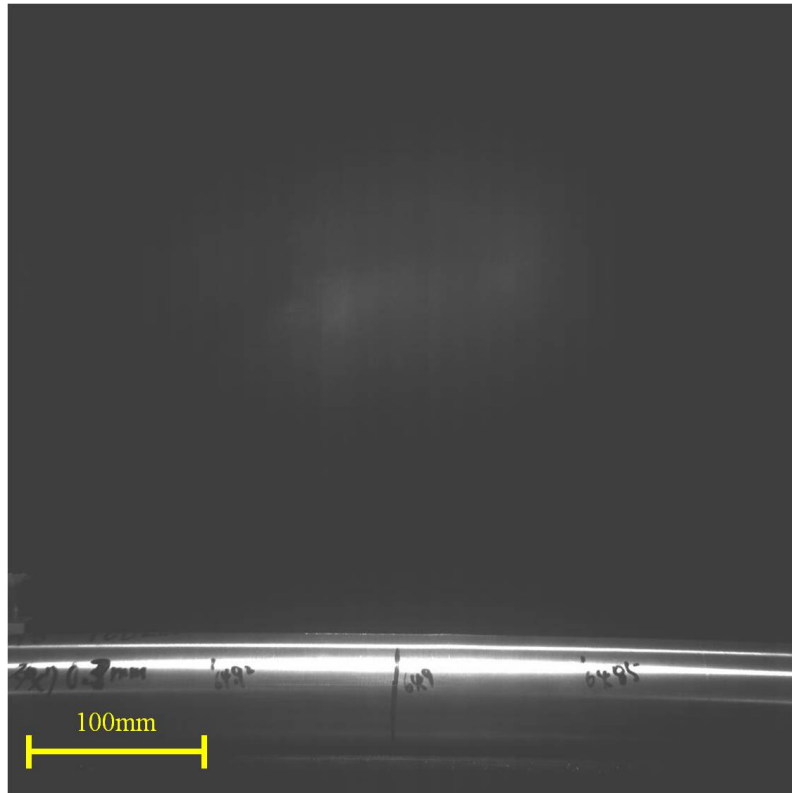


Fig. 4.30 Bubble profile at 0ms after the burst for No.2, side view

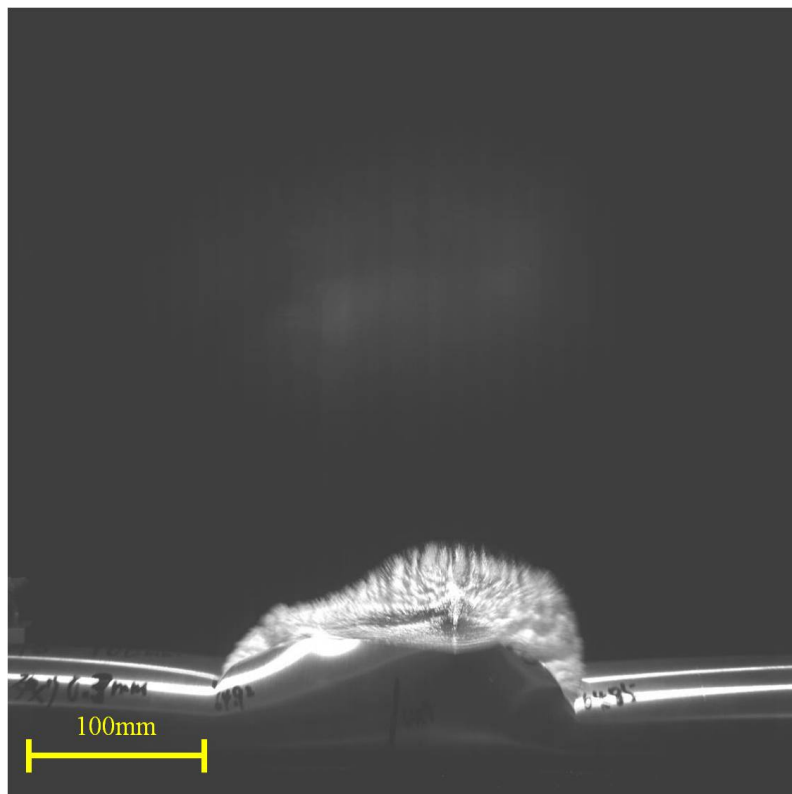


Fig. 4.31 Bubble profile at 2ms after the burst for No.2, side view

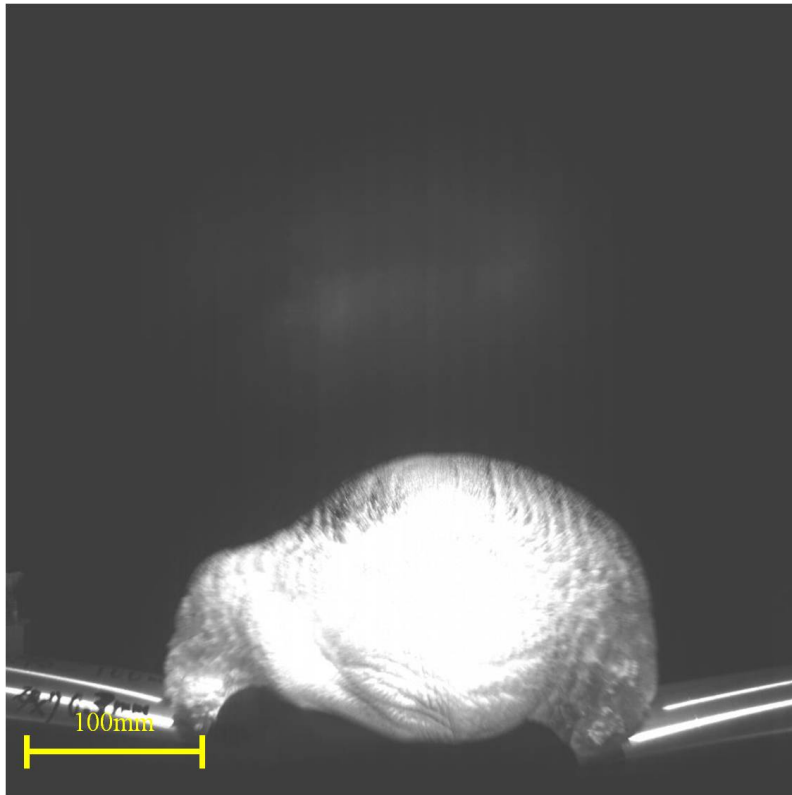


Fig. 4.32 Bubble profile at 4ms after the burst for No.2, side view

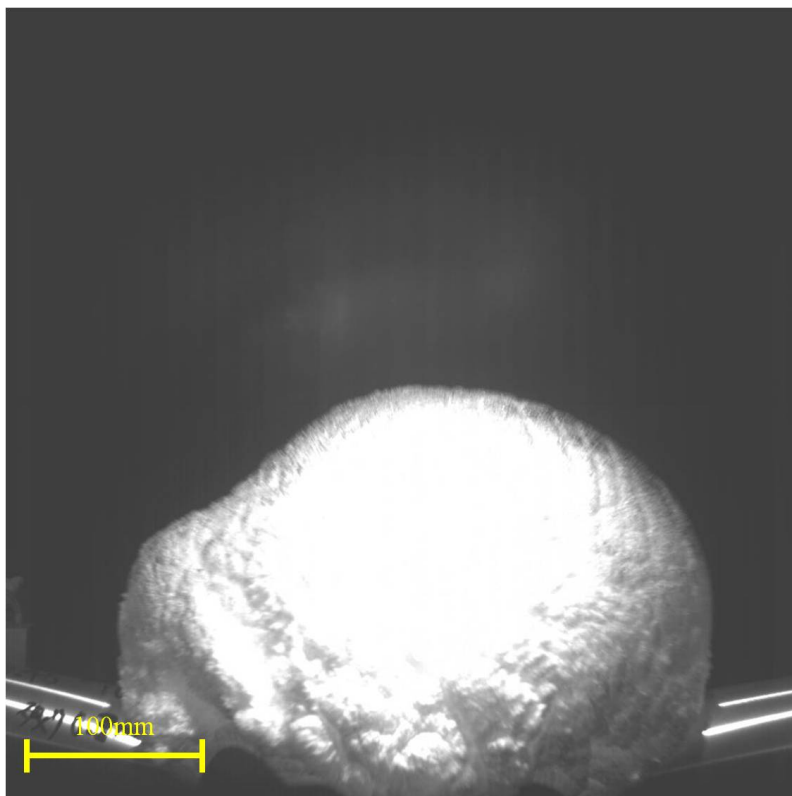


Fig. 4.33 Bubble profile at 6ms after the burst for No.2, side view

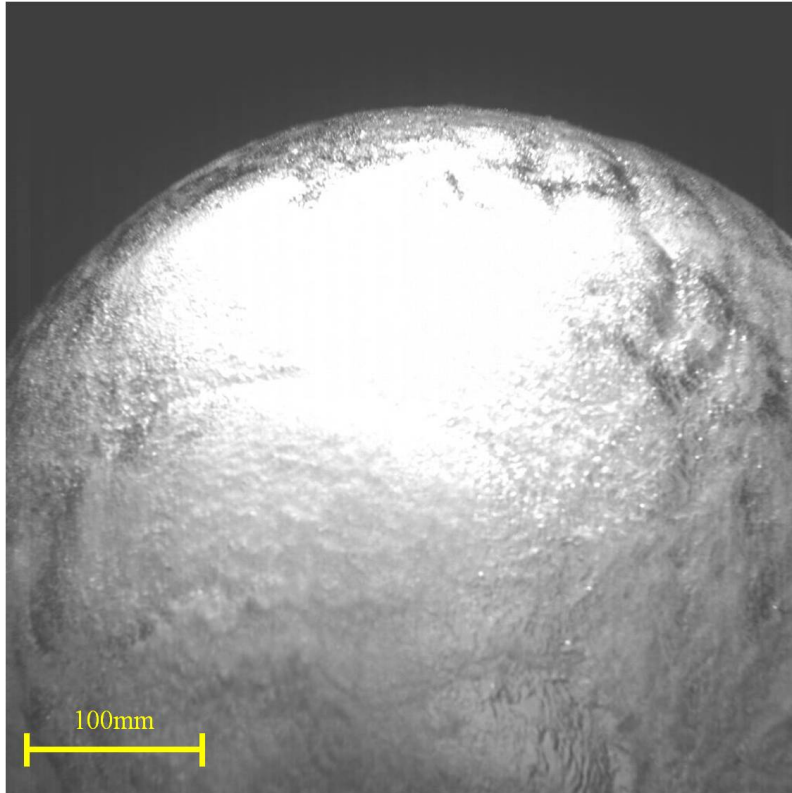


Fig. 4.34 Bubble profile at 20ms after the burst for No.2, side view

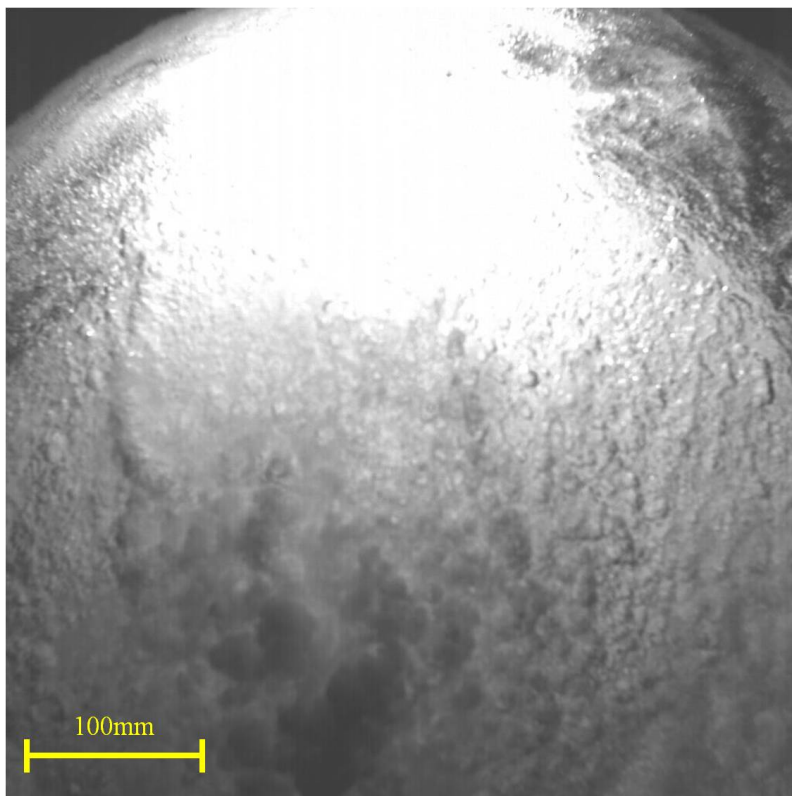


Fig. 4.35 Bubble profile at 40ms after the burst for No.2, side view



Fig. 4.36 Bubble profile at 0ms after the burst for No.2, axial view

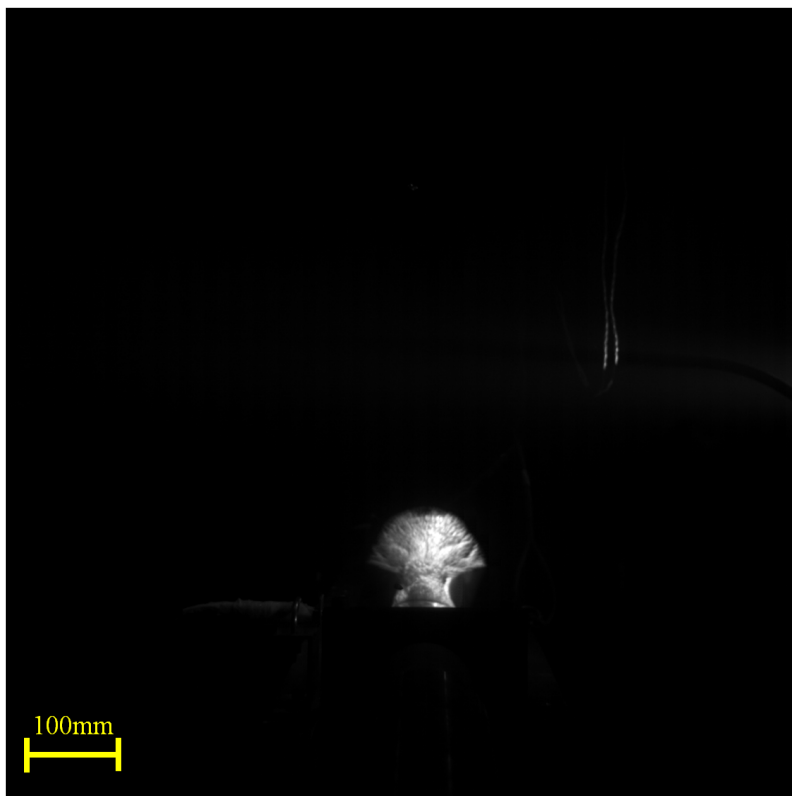


Fig. 4.37 Bubble profile at 2ms after the burst for No.2, axial view

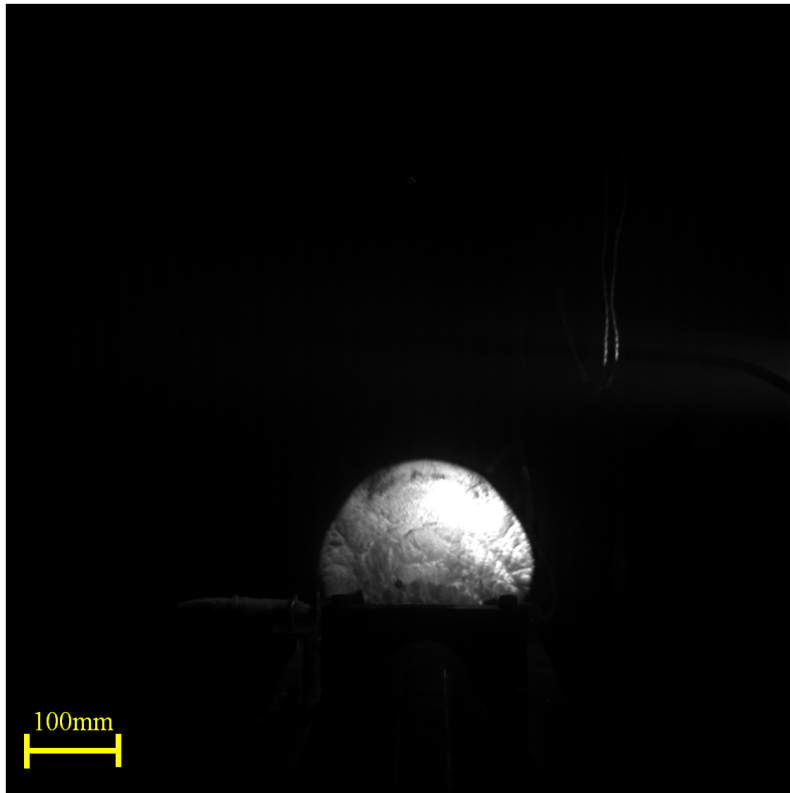


Fig. 4.38 Bubble profile at 4ms after the burst for No.2, axial view

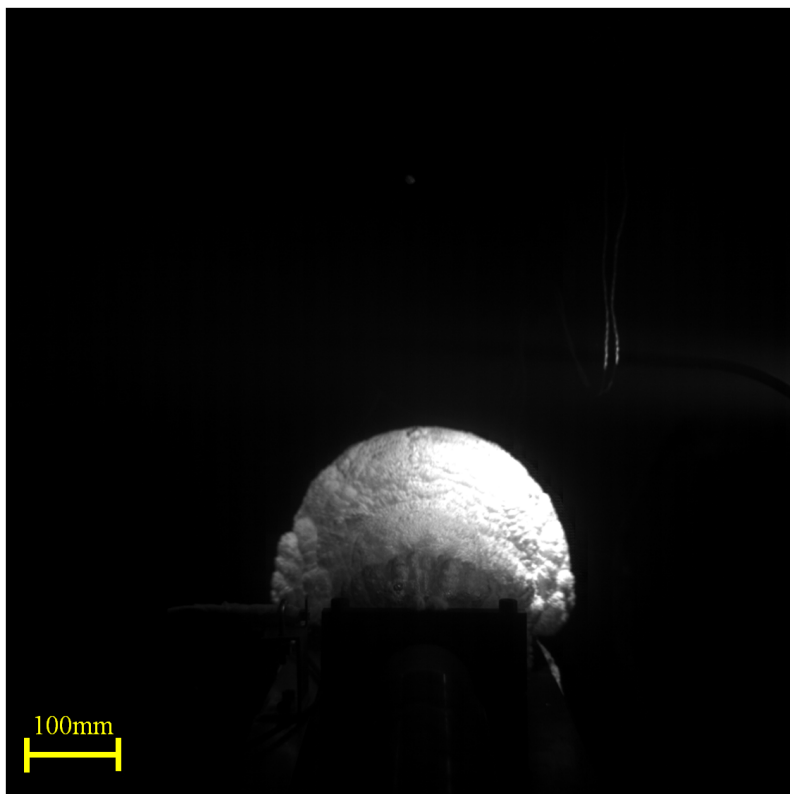


Fig. 4.39 Bubble profile at 6ms after the burst for No.2, axial view

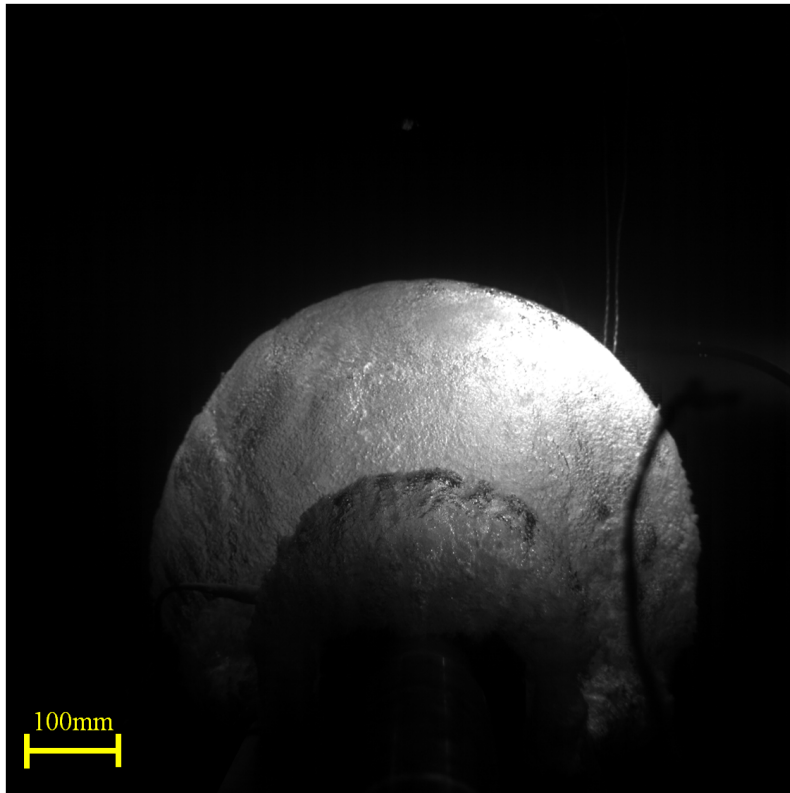


Fig. 4.40 Bubble profile at 20ms after the burst for No.2, axial view

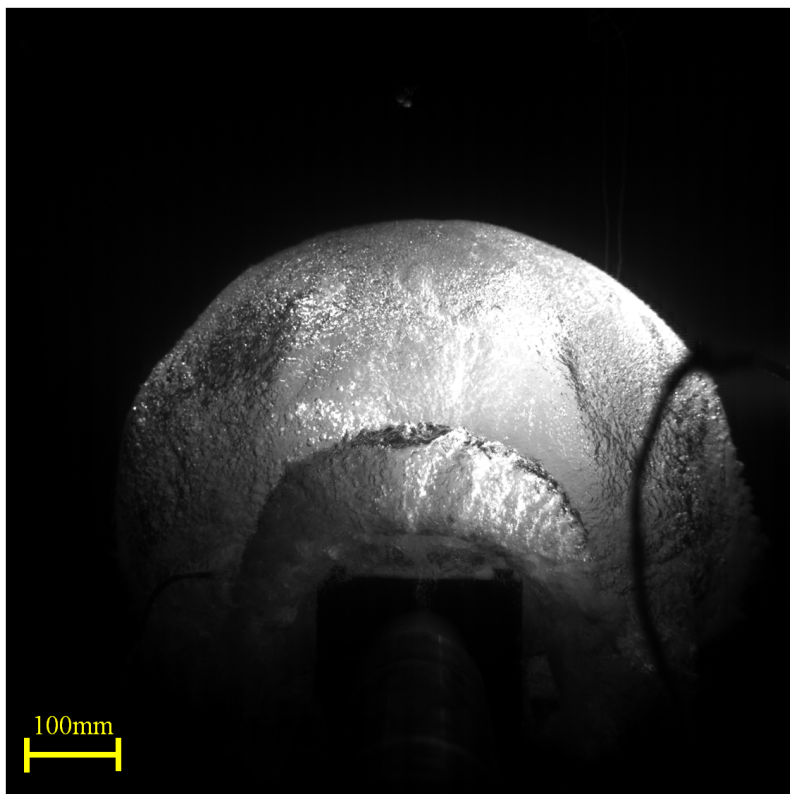


Fig. 4.41 Bubble profile at 40ms after the burst for No.2, axial view

4.2.2 The history of the bubble growth

In order to measure the histories of the bubble growth quantitatively, transparent board with white grids, each of which is 20mm by 20mm, was captured at the same position as the tested pipes, see Fig. 4.42. Actual size of the captured photos is about 420mm by 420mm. On the other hand, outline of each captured bubble profile was traced by yellow line which has particular RGB data, see Fig. 4.43. By the image processing code developed by the author, the distribution of the bubble radius was obtained as shown in Fig. 4.44; bubble radius was assumed to be half of the distance between top and bottom of the outline at each position along the axial direction. Horizontal axis directly corresponds to the width of Fig. 4.44; the center of the pipe corresponds to 220mm in the horizontal axis.

By repeating above procedure, histories of the bubble profile are obtained as shown in Fig. 4.45 and Fig. 4.46. The average bubble growth rate at the maximum radius until 6ms for the test No.1 was around 15m/s. For the test No.2, that was around 19m/s. Although the tip of the bubble is assumed to be fixed at the crack tip in the UT offshore model, experimental results clarified that the bubble expands to the axial direction beyond the crack tip. The UT offshore model needs improvements regarding this discrepancy for analyzing a bubble growth for a non propagating crack.

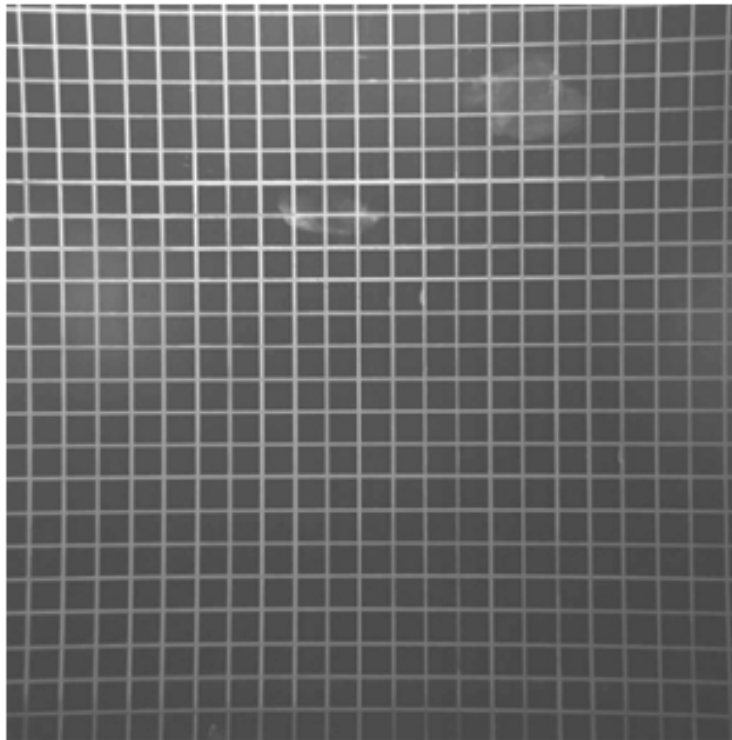


Fig. 4.42 Transparent board with white grids at the same position as the tested pipes, captured by high-speed camera

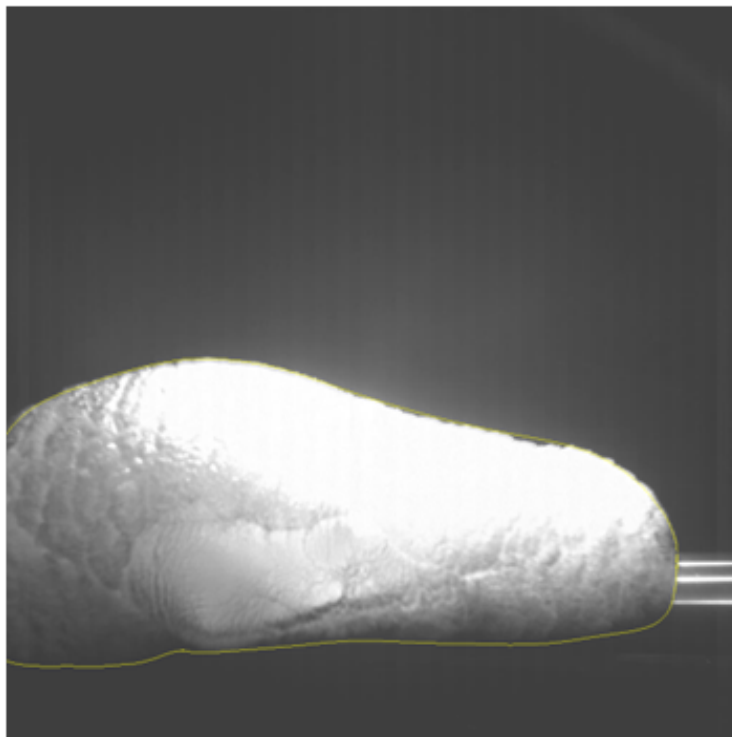


Fig. 4.43 An example of bubble outline traced by yellow line

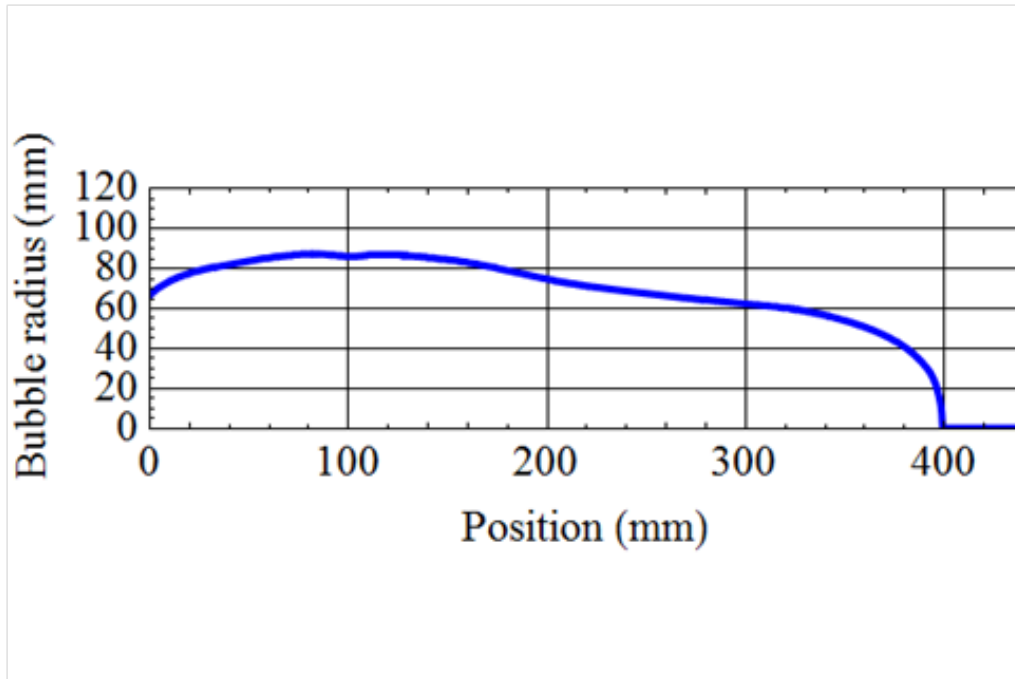


Fig. 4.44 An example of bubble profile, bubble radius distribution

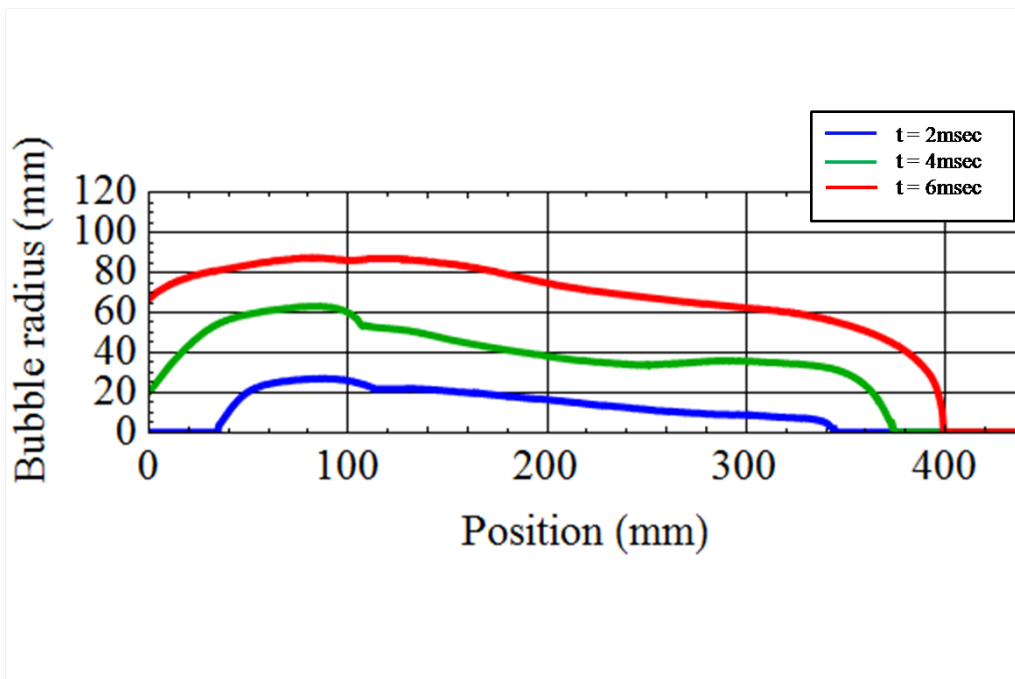


Fig. 4.45 Time history of bubble profile at each time for No.1

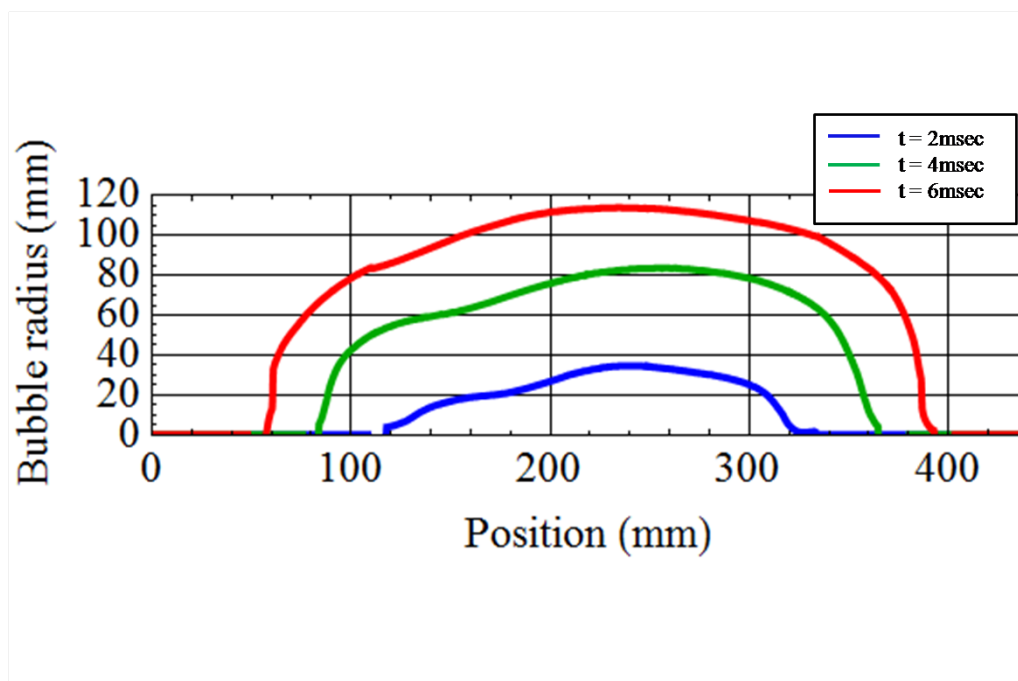


Fig. 4.46 Time history of bubble profile at each time for No.2

4.3 Calculation results for the validation of the bubble growth modeling in the UT offshore models

For the validation of the bubble growth modeling in the UT offshore model, simulating calculations were conducted by inputting the same conditions as the experimental ones. In the present calculations, the cracks were assumed not to propagate beyond the tip of the surface notch because the experimental results showed that the cracks deviated to the circumferential direction at the tip of the surface notch. Therefore, simplified crack opening profiles, which is determined by shape parameter ψ as shown in Fig. 3.3, were incorporated into the calculations as input conditions according to the experimental measurements;

For test No.1,

$$\psi(x, t) = \begin{cases} -\frac{2t}{x_{st}^2 \cdot 0.006} x^2 + \frac{2t}{0.006} & \text{for } 0 \leq t < 0.003, 0 \leq x \leq x_{st} \\ -\frac{2}{x_{st}^2} \left(1 - \frac{t}{0.006}\right) x^2 + 1 & \text{for } 0.003 \leq t \leq 0.006, 0 \leq x \leq x_{st} \end{cases} \quad (4.4)$$

For test No.2,

$$\psi(x, t) = \frac{t}{0.006} \quad \text{for } 0 \leq t < 0.006, 0 \leq x \leq x_{st} \quad (4.5)$$

where units of x and t are meter and second, respectively. x_{st} is the positions of the tips of surface notched which correspond to 0.15m and 0.05 m for test No.1 and No.2. It was assumed that there was no crack opening ahead of the surface notches.

It follows that the present calculations are for the validation of only the bubble growth and gas decompression modeling in the UT offshore model. Calculation conditions are shown in Table 4.3 Incremental length Δx and time step size Δt are set to 1mm and $0.25\mu s$, respectively.

Calculated internal pressure histories are shown in Fig. 4.47 and Fig. 4.48. Calculations were conducted until 6ms when the crack was arrested in the circumferential direction and the pipe did not deforms any more. Red and blue lines show the calculated and experimental result, respectively. Although small difference are seen, there are generally good agreements between the calculated and experimental result.

4.3. CALCULATION RESULTS FOR THE VALIDATION OF THE BUBBLE GROWTH MODELING IN

Figure 4.49, Fig. 4.50 and Fig. 4.51 show comparison between calculated and experimental histories of the bubble profile for No.1. Note that the tip of the bubble was fixed at the tip of the surface notch in the calculated results. Except for the small difference at the bubble end, good agreements between calculated and experimental bubble profile are seen. Fig. 4.52 shows the comparison between calculated and experimental history of the bubble radius at the pipe center. The slope of the curves correspond to the bubble growth rate at the position. There is also a good agreement between them.

Figure 4.53, Fig. 4.54 and Fig. 4.55 show comparison between the calculated and experimental histories of the bubble profile for No.2. Unlike the calculated results for No.1, there are big discrepancies between calculated and experimental results. The main reason for the discrepancies is supposedly that the bubble tip is fixed at the crack tip. In the test No.1, the bubble did not expand to the axial direction beyond the tip of the surface notch. On the other hand, in the test No.2, the bubble clearly expanded beyond the tip of surface notch. It might be said that prediction accuracy for the bubble growth drops if the model is applied to the test where the bubble expansion to the axial direction is far greater than the crack length. However, the crack velocity, which is usually around 200m/s, might be greater than bubble expansion velocity to the axial direction. Therefore, the bubble can expand beyond the crack tip only when the crack is already arrested or drastically slowed down. Because the surface notch length for No.2 is shorter than that for No.1, the discrepancies supposedly happened due to the long time calculation after the crack was arrested.

To summarize, gas decompression modeling was successfully validated through the good agreements between calculated and experimental results. Also, bubble growth modeling was validated through the good agreements between calculated and experimental result for No.1. From the discrepancies seen in the calculation results for No.2, it might be clarified that the bubble growth model is applicable until the crack is arrested; in other words, the UT offshore model is not suitable for the bubble growth for a stationary crack.

Table 4.3 Calculation condition

Medium	Pure nitrogen
Initial pressure (MPa)	0.95 for No.1 & 1.31 for No.2
Temperature (° C)	20
Outer diameter (mm)	70
Pipe thickness (mm)	1.00 for No.1 & 0.45 for No.2
Pipe length (m)	1.6
Initial crack length (mm)	300 for No.1 & 100 for No.2
Water depth (m)	1
Water density (kg/m ³)	1000
Water dynamic viscosity (m ² /s)	1.0×10^{-6}
Water surface tension (N/m)	72.75×10^{-3}
Software for isentropic process	REFPROP
Δx (mm)	1
Δt (μs)	0.25

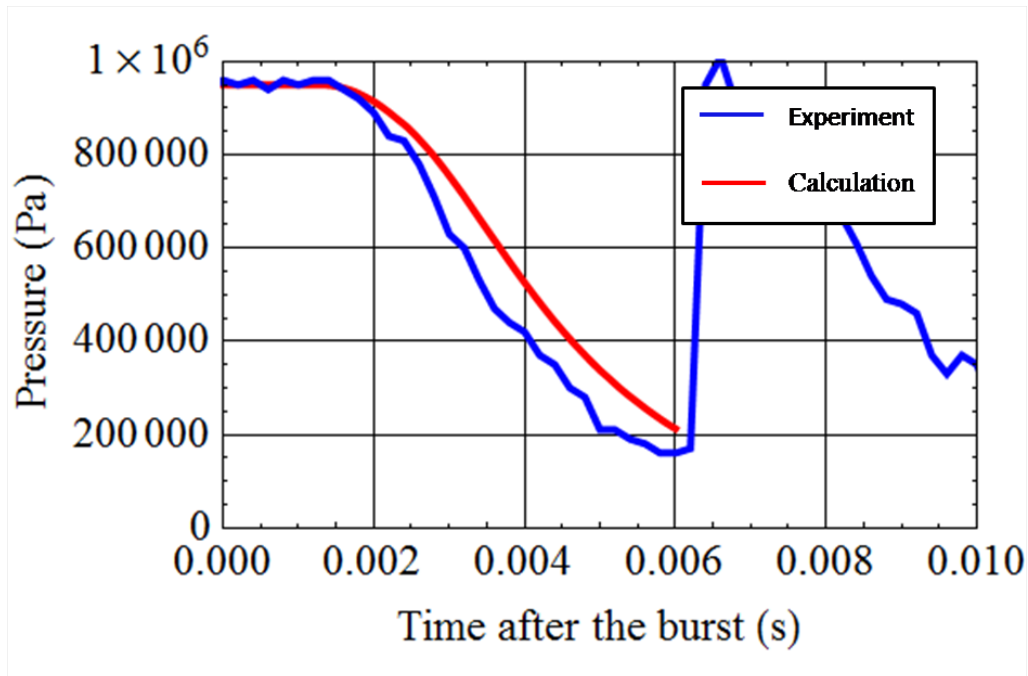


Fig. 4.47 Calculated time history of dynamic internal pressure for No.1

4.3. CALCULATION RESULTS FOR THE VALIDATION OF THE BUBBLE GROWTH MODELING IN

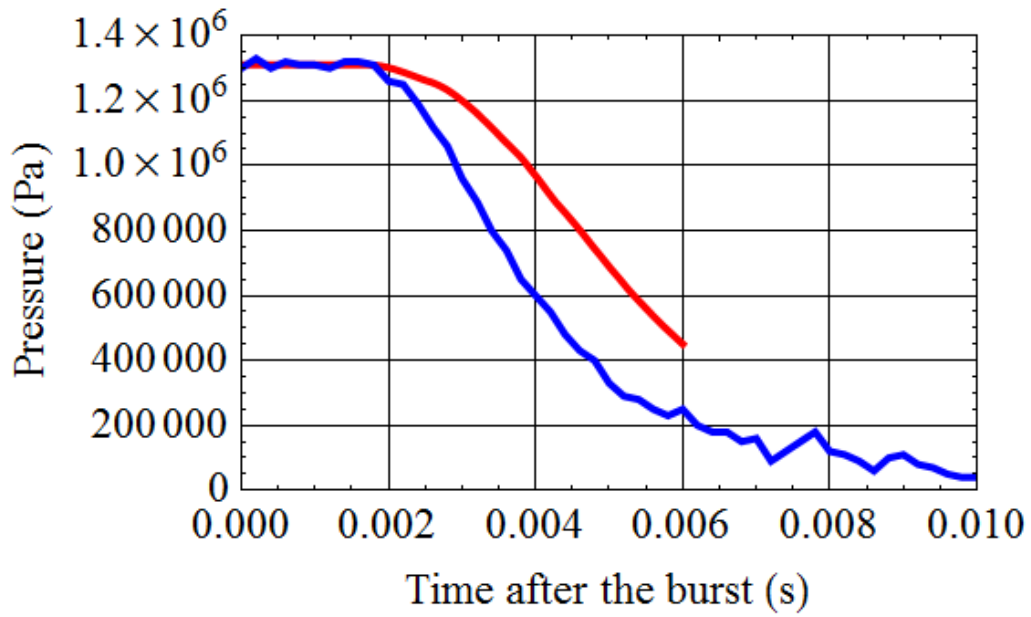


Fig. 4.48 Calculated time history of dynamic internal pressure for No.2

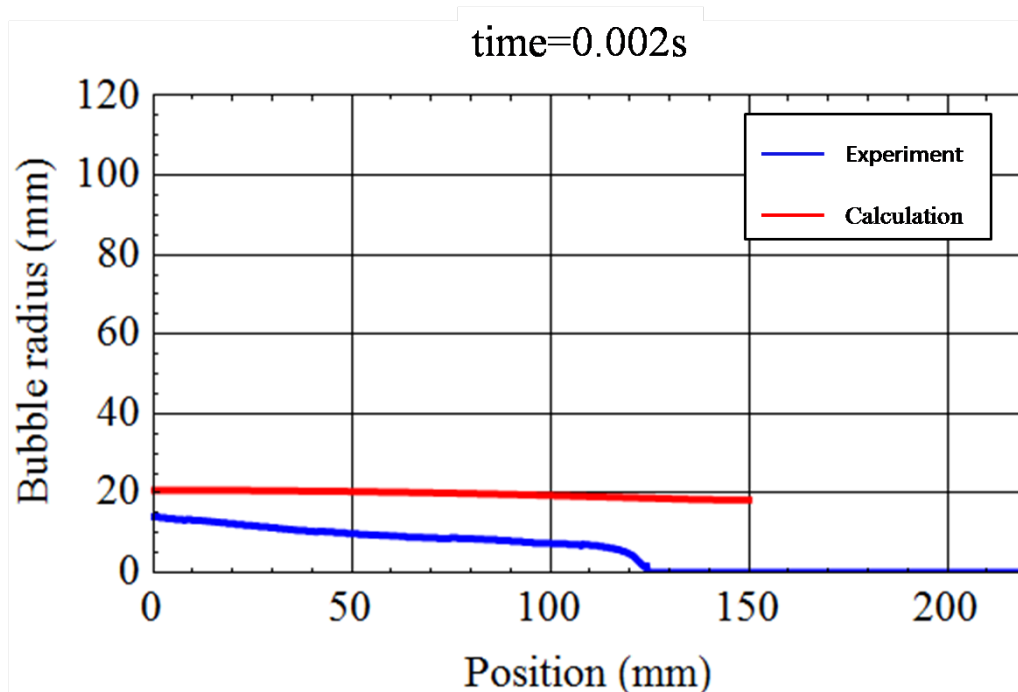


Fig. 4.49 Calculated bubble profile at 2ms after the burst for No.1

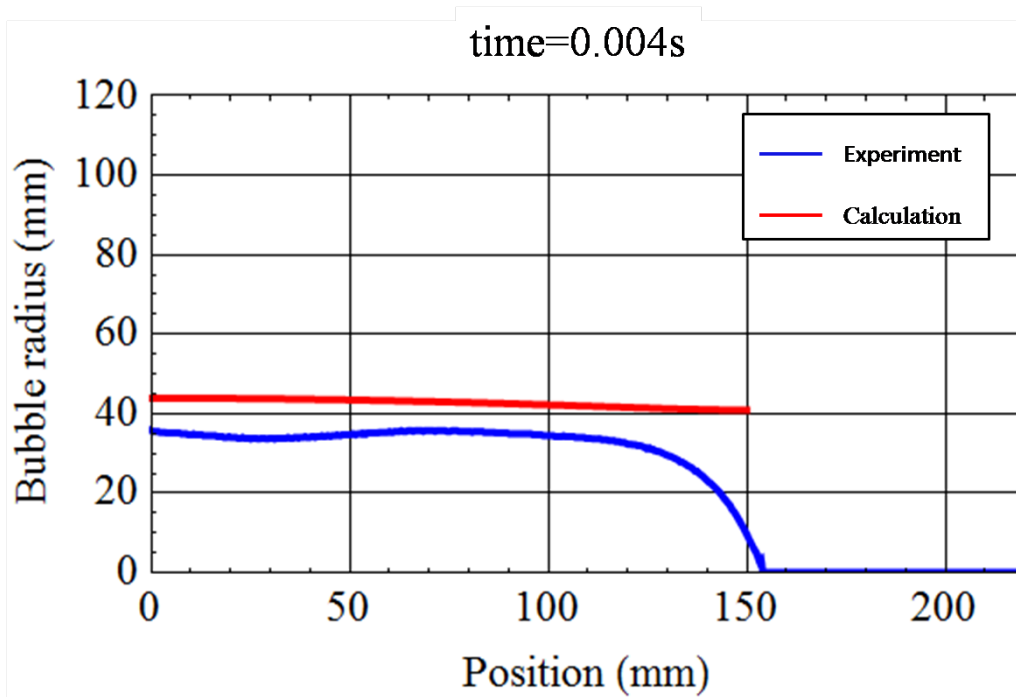


Fig. 4.50 Calculated bubble profile at 4ms after the burst for No.1

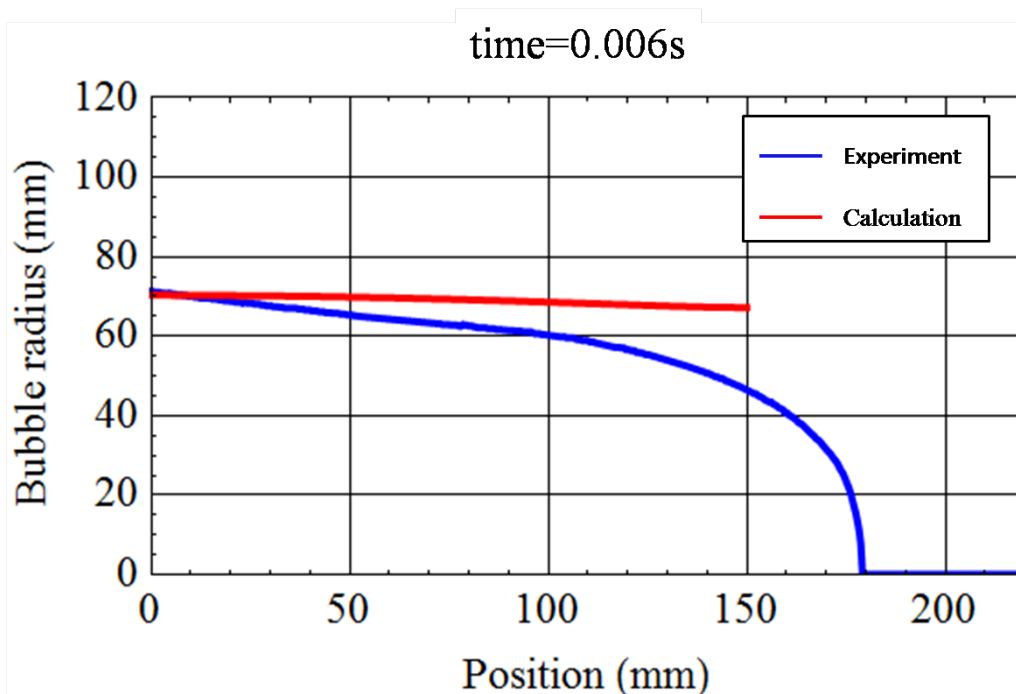


Fig. 4.51 Calculated bubble profile at 6ms after the burst for No.1

4.3. CALCULATION RESULTS FOR THE VALIDATION OF THE BUBBLE GROWTH MODELING IN

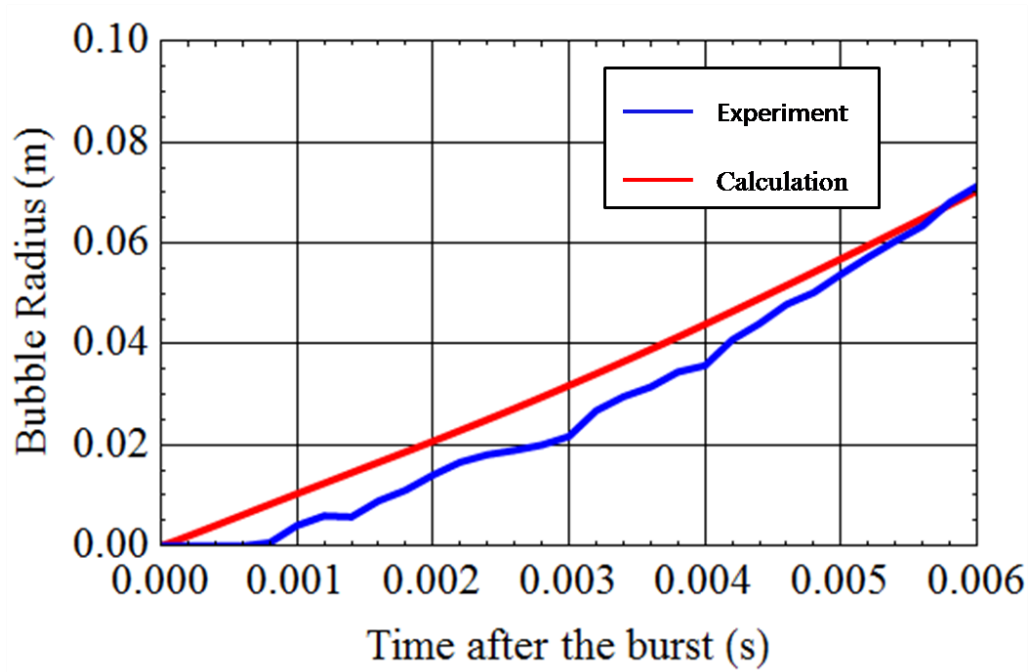


Fig. 4.52 Calculated time history of bubble radius at the pipe center for No.1

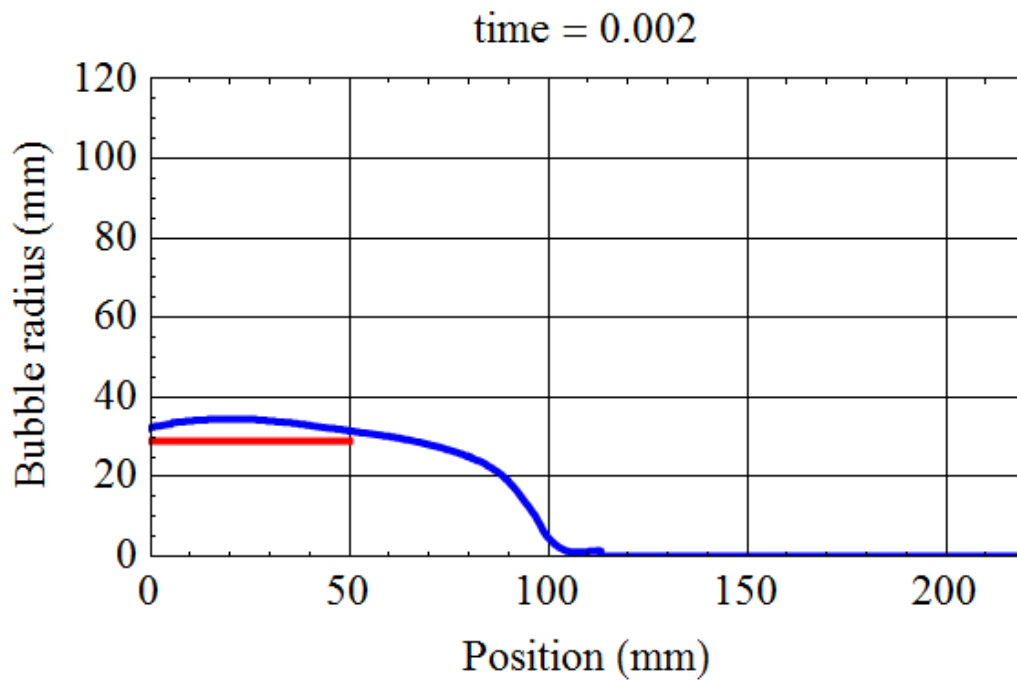


Fig. 4.53 Calculated bubble profile at 2ms after the burst for No.2

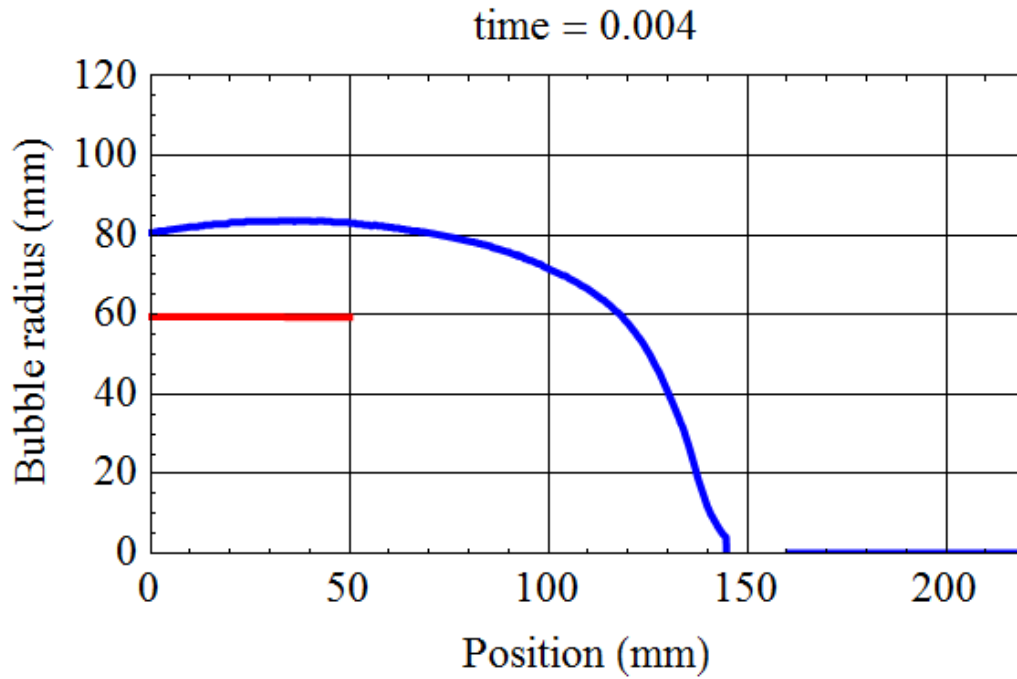


Fig. 4.54 Calculated bubble profile at 4ms after the burst for No.2

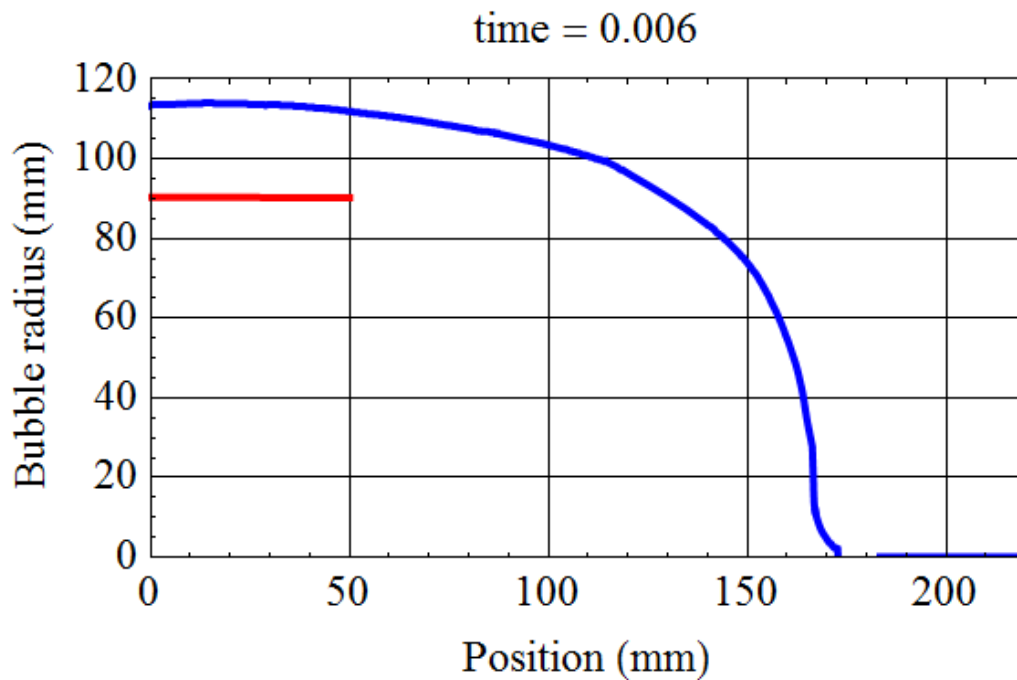


Fig. 4.55 Calculated bubble profile at 6ms after the burst for No.2

4.3. CALCULATION RESULTS FOR THE VALIDATION OF THE BUBBLE GROWTH MODELING IN

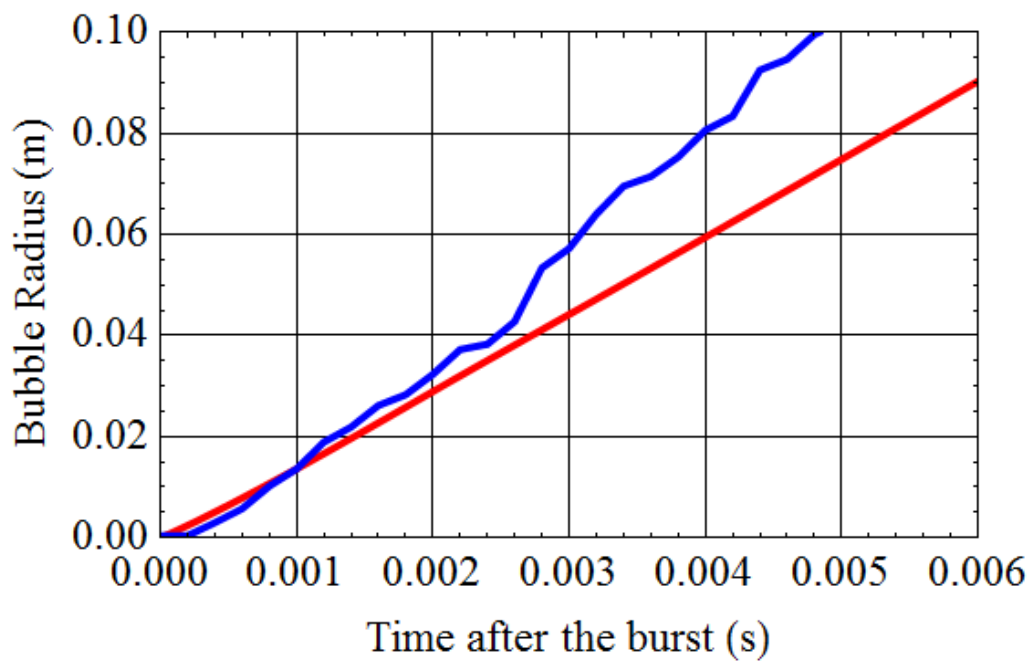


Fig. 4.56 Calculated time history of bubble radius at the pipe center for No.2

4.4 Summary

- The small-scale underwater pipe rupture tests were conducted.
- The time histories of bubble profile and dynamic internal and external pressure were successfully observed using high-speed camera and pressure transducers.
- The calculation by gas decompression model and bubble growth model in the UT offshore model showed good agreements with the experimental results especially for No.1.
- The applicable range of the UT offshore model is clarified through the discussion about the discrepancies between the calculated and experimental results for No.2.

Chapter 5

Calculation for the full-scale offshore pipeline burst test

For the validation of the whole UT offshore model, calculation for the full-scale offshore pipeline burst test was conducted. The UT offshore model was applied to the test conducted by C.S.M in the 1980s[36]. The detail of the calculation is described below.

5.1 Testing conditions[36]

Reference [36] includes two offshore tests on 20 and 36 inch X60 pipes. The present calculation was conducted for the test on the 36 inch pipe, because this test is reported in more detail in Ref.[36].

The geometry of the tested pipe was:

- Outside diameter : 36 inches
- Thickness : 20.5 mm
- Length of each pipes : 9 m

The pipes were welded to total length of 108m, see Fig. 5.1. Figure 5.1 also shows Charpy absorbed energy of each pipe. Testing instrumentations are shown in Fig. 5.2. Solid and open marks represent internal and external pressure transducers, respectively. Also, 32 timing wires were attached on the surface of the tested pipe. Testing conditions are shown in Table 5.2.

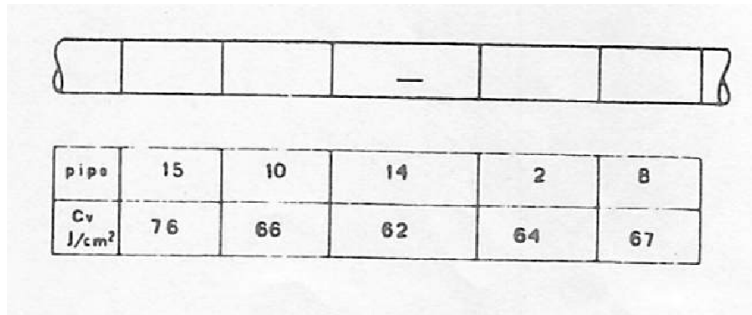


Fig. 5.1 Tested pipe arrangement and Charpy energy of each pipe[36]

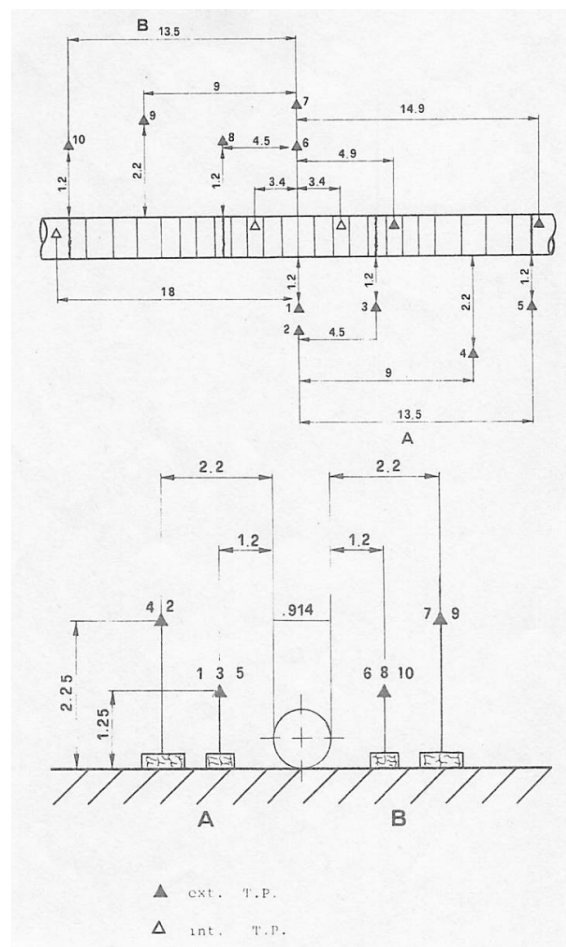


Fig. 5.2 Instrumentation layout[36]

Table 5.1 Testing condition[36]

Outside diameter (inch)	Thickness (mm)	Length (m)	Depth (m)	Pressure (MPa)	Medium	Temperature (° C)
36	20.8	108	30	15.7	Air	15

5.2 Testing result[36]

Photos of the test are shown in Fig. 5.3. High water column, reaching around 70m, was observed.

The histories of the internal pressure at the positions 3.4m and 18m away from the pipe center are shown in Fig. 5.4. Also, the histories of the crack propagation are shown in Fig. 5.5, where the slope of the lines correspond to the crack velocities. These testing results are compared with the calculated results described in the next section.

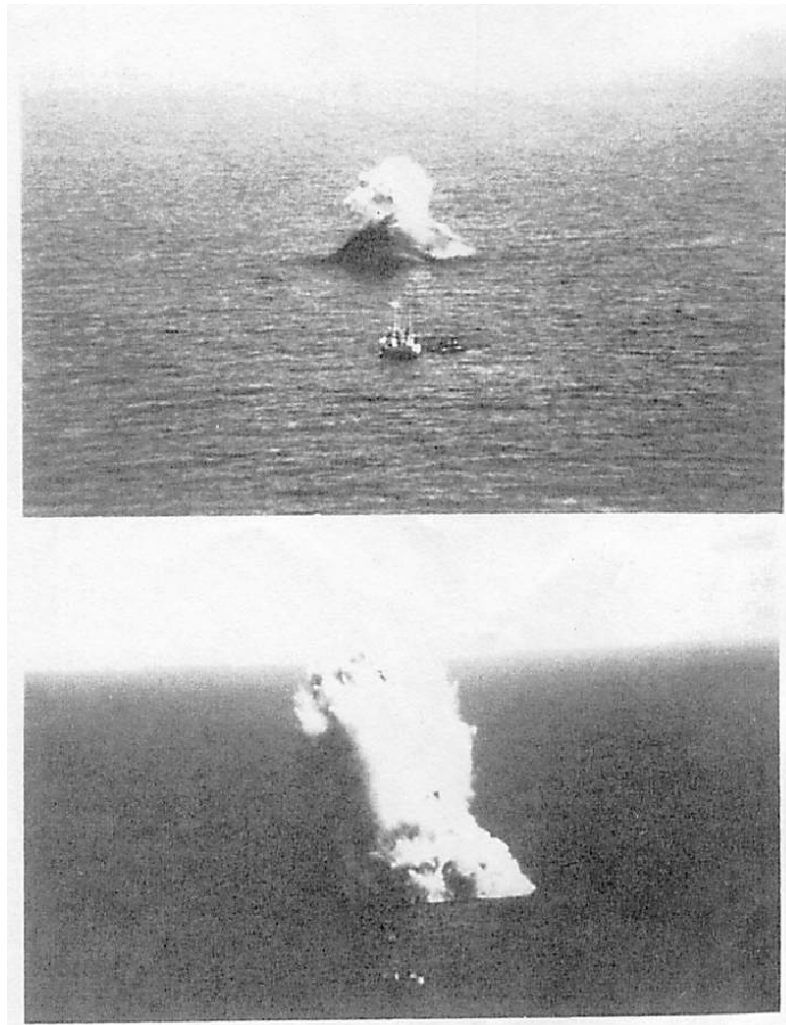


Fig. 5.3 Photos of the test showing high water column[36]

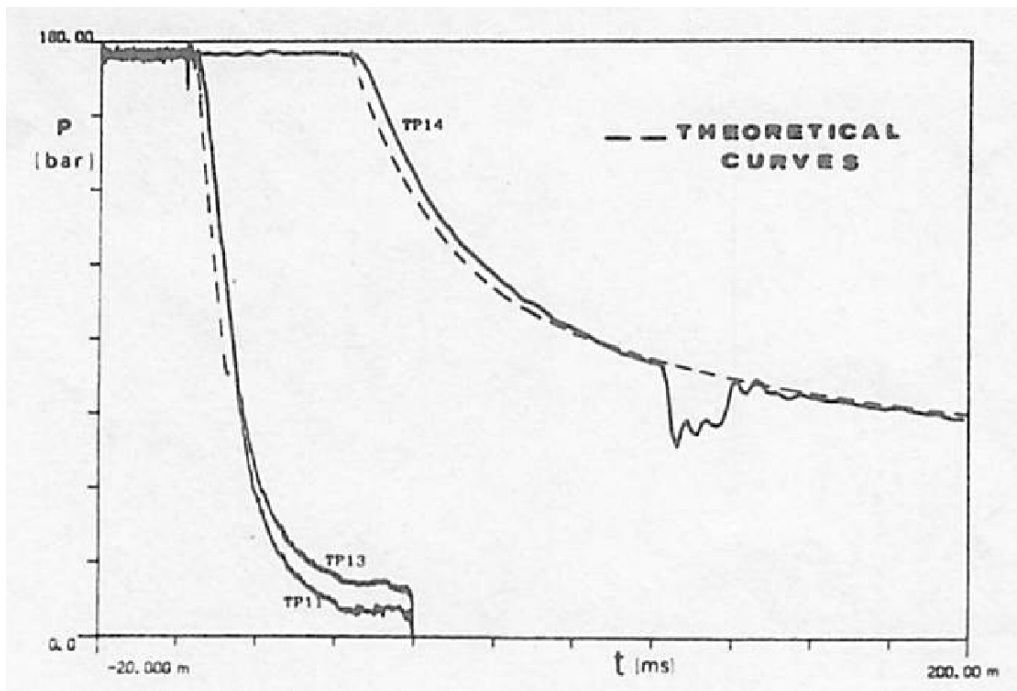


Fig. 5.4 Experimental time histories of internal pressure 3.4m and 18m away from the pipe center[36]

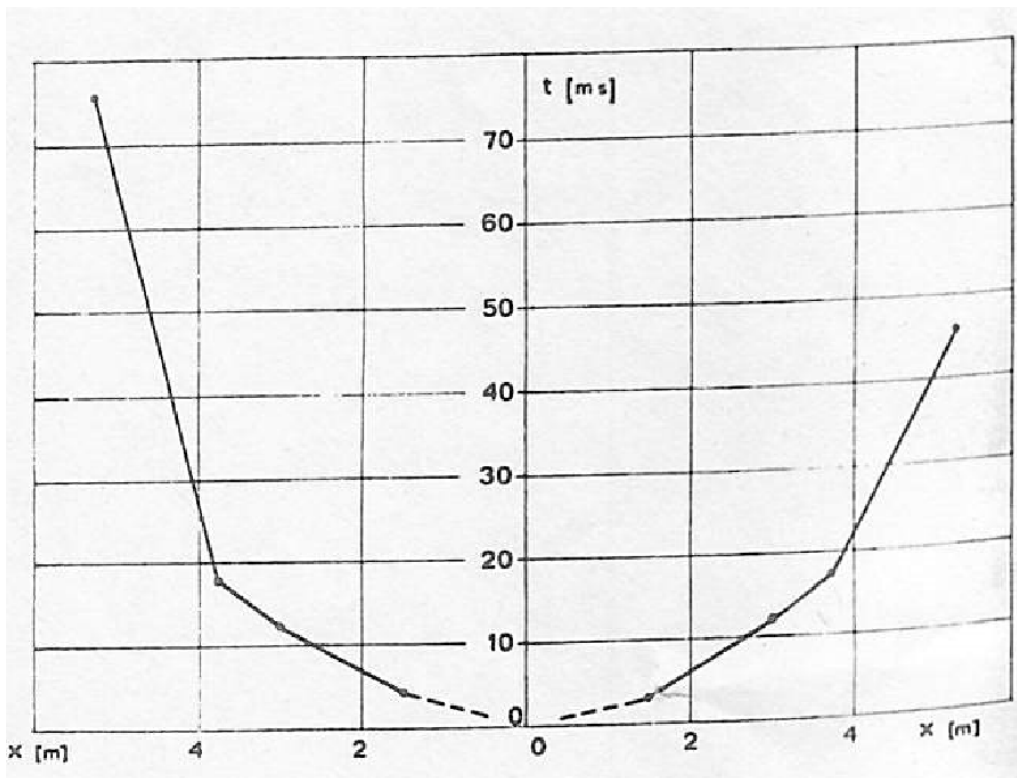


Fig. 5.5 Experimental time histories of the crack length[36]

5.3 Calculated result

Calculation conditions are shown in Table 5.2. Incremental length Δx and time step size Δt were set to 20mm and $5\mu s$, respectively. The calculation was conducted for a half of the pipe in the right hand side of Fig. 5.1.

Figure 5.6 shows the comparison between calculated and experimental histories of the internal pressure at the position 3.4m and 18m away from the pipe center. Fig. 5.7 shows the comparison between calculated and experimental histories of the crack propagation, showing the crack tip position versus the crack velocity. Blue and black lines represent calculated and experimental results, respectively.

In Fig. 5.6, the calculated history of the internal pressure at the position 3.4m away from the pipe center is higher than the experimental one, because the calculated crack is arrested behind the pressure measurement position, i.e., 3.4m, as shown in Fig. 5.7. After the crack propagates at particular position, the crack opening occurs together with the pipe deformation, then the pressure at the position suddenly decreases due to the gas leak from the crack opening. Therefore, the discrepancy in Fig. 5.6 is resulted from small discrepancy of crack propagation history which means that there is not the problem of the gas decompression model.

In Fig. 5.7, the calculated average crack velocity is close to the experimental one, which are around 180m/s. Also, there is generally good agreement between the calculated and experimental arrest length because both of the cracks are arrested within the same pipe which is 9m long.

Due to the good agreements between calculated and experimental results, it is clarified that the UT offshore model can be applied to the unstable ductile crack in offshore pipelines. Needless to say, more calculations for the validation of the model are necessary. However, because there have been only a few full-scale offshore pipeline burst tests in history, a lack of number of calculations for the validation is inevitable at the current moment. It is strongly necessary that more full-scale offshore pipeline burst tests on newer pipe grade should be conducted in the future.

5.4 Summary

- For the validation of the UT offshore model, the calculation for the full-scale offshore pipeline burst test was conducted.

- The calculated results showed good agreements with the experimental ones.
- To validate the UT offshore model more precisely, more full-scale offshore pipeline burst tests are necessary.

Table 5.2 Reference conditions for the parametric studies

Medium	Air
Initial pressure (MPa)	15.7
Temperature (° C)	15
Outer diameter (inch)	36
Pipe thickness (mm)	20.8
Pipe density (kg/m ³)	7860
Pipe length (m)	108
Tensile yield strength (MPa)	413
Grade	X60
Charpy energy (J/cm ²)	see Fig. 5.1
Initial crack length (inch)	36
Water depth (m)	30
Water density (kg/m ³)	1000
Water dynamic viscosity (m ² /s)	1.0×10^{-6}
Water surface tension (N/m)	72.75×10^{-3}
Software for isentropic process	GASDECOM
Δx (mm)	20
Δt (μ s)	5

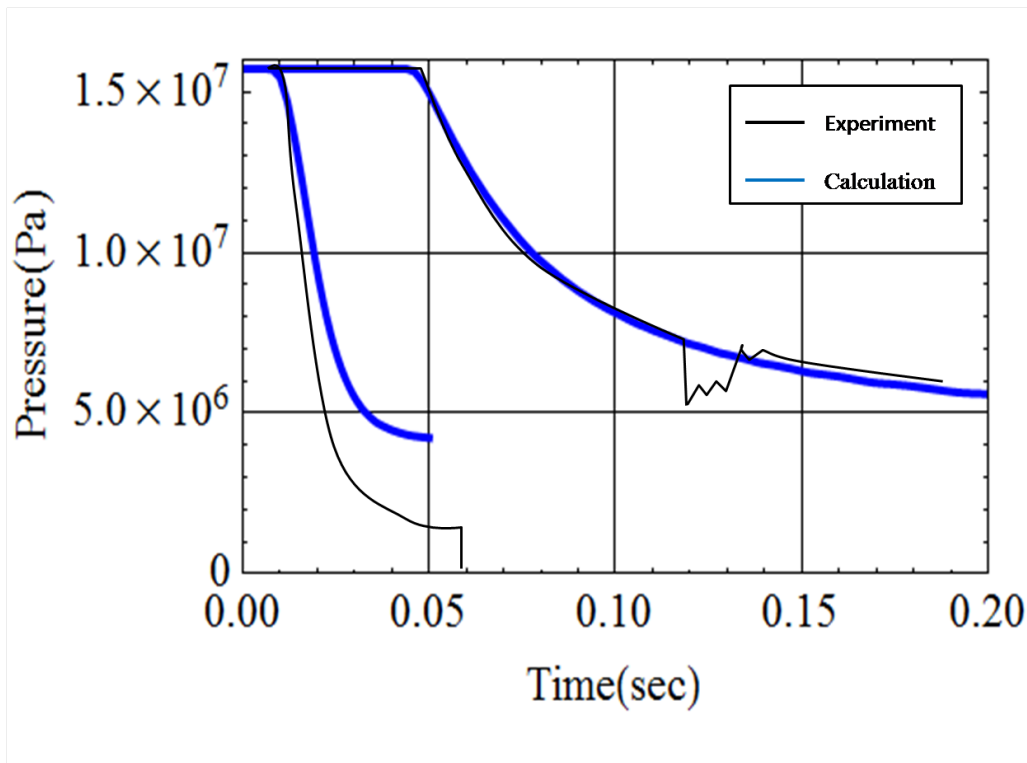


Fig. 5.6 Calculated time histories of internal pressure 3.4m and 18m away from the pipe center

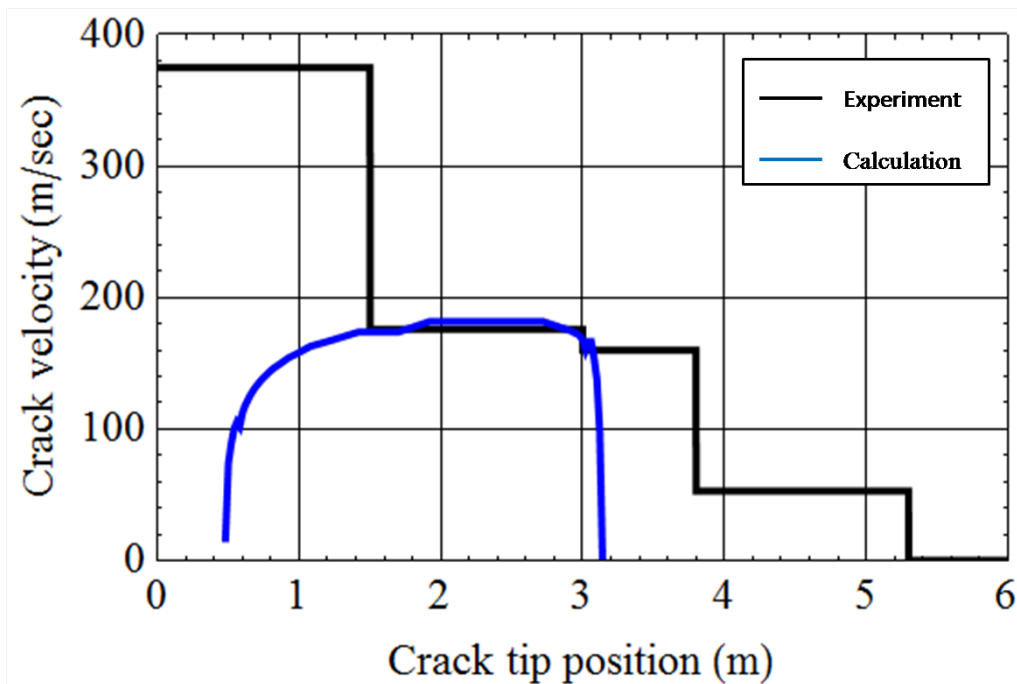


Fig. 5.7 Calculated crack tip position versus crack velocity

Chapter 6

Parametric study

Parametric study was conducted to discuss the effects of pipe geometry, mechanical properties and water depth on unstable ductile crack propagation/arrest in offshore pipelines by the UT offshore model.

6.1 Reference conditions

The conditions of full-scale offshore pipeline burst test conducted by CSM as described in the previous chapter are adopted as reference conditions, see Table 6.1. Parameters which are changed in the present chapter are as follows: water depth, pipe thickness, outer diameter, pipe grade (tensile yield strength) and toughness. The effect of each parameter on unstable ductile crack propagation/arrest behavior is described below.

6.2 Water depth

Calculations were conducted by changing water depth from 0m to 1,000m, see Tab. 6.2. Calculated histories of crack propagation are shown in Fig. 6.1. The peak velocities at the beginning decreases with increasing water depth, and unstable propagation happens only for the case with water depths of 0m, which are regarded as the case of onshore pipeline. The calculated results that increasing water depth makes a crack more likely to be arrested is reasonable.

Figure 6.2 shows internal pressure distributions at 50ms for each water depth. Increasing water depth results in much more delay of gas decompression. Note that the pressure close to the pipe center goes to plateau, because internal pressure does not drop below the hydrostatic pressure in

Table 6.1 Reference conditions for the parametric study

Medium	Air
Initial pressure (MPa)	15.7
Temperature (° C)	15
Outer diameter (inch)	36
Pipe thickness (mm)	20.8
Pipe density (kg/m ³)	7860
Pipe length (m)	108
Tensile yield strength (MPa)	413
Grade	X60
Charpy energy (J/cm ²)	right hand side of the test section as shown in Fig. 5.1
Initial crack length (inch)	36
Water depth (m)	30
Water density (kg/m ³)	1000
Water dynamic viscosity (m ² /s)	1.0×10^{-6}
Water surface tension (N/m)	72.75×10^{-3}
Software for isentropic process	GASDECOM
Δx (mm)	20
Δt (μ s)	5

the UT offshore model. Although the delays of gas decompression lead to high crack driving force, the cracks inversely get more likely to be arrested. The reason for that might be because increasing hydrostatic pressure and water backfill dominantly affect the behavior of unstable ductile crack propagation in offshore pipelines.

Table 6.2 Changed water depth

Water depth (m)
0(air)
30(reference value)
100
300
1000

6.3 Pipe thickness

Calculations were conducted by changing pipe thickness from 10mm to 35mm, see Table 6.3. Calculated histories of crack propagation are shown

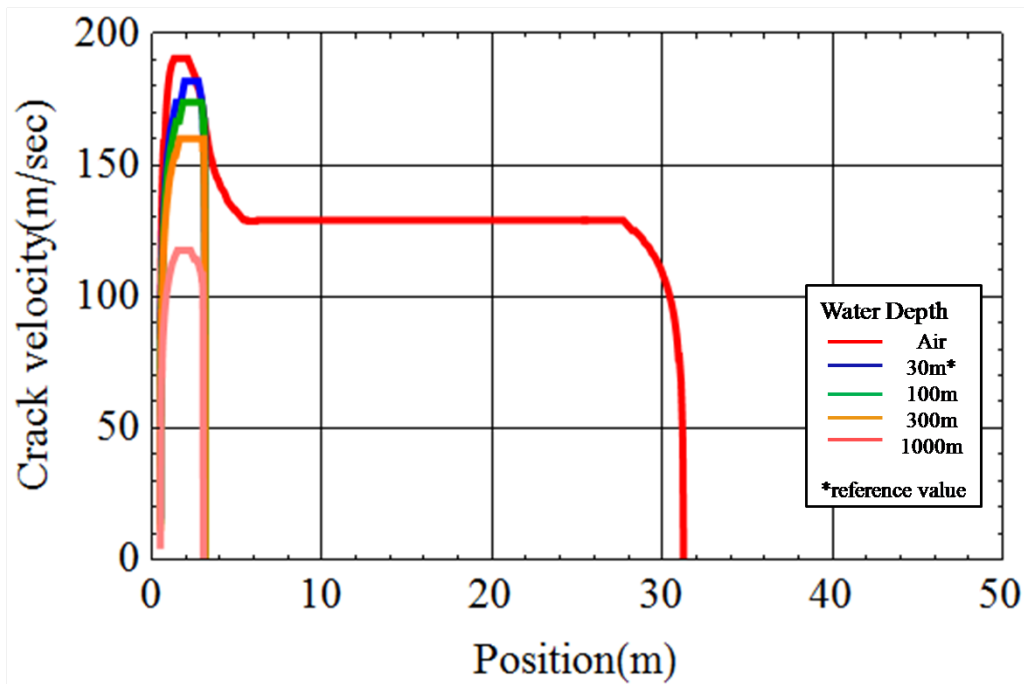


Fig. 6.1 Dependence of crack propagation/arrest on water depth

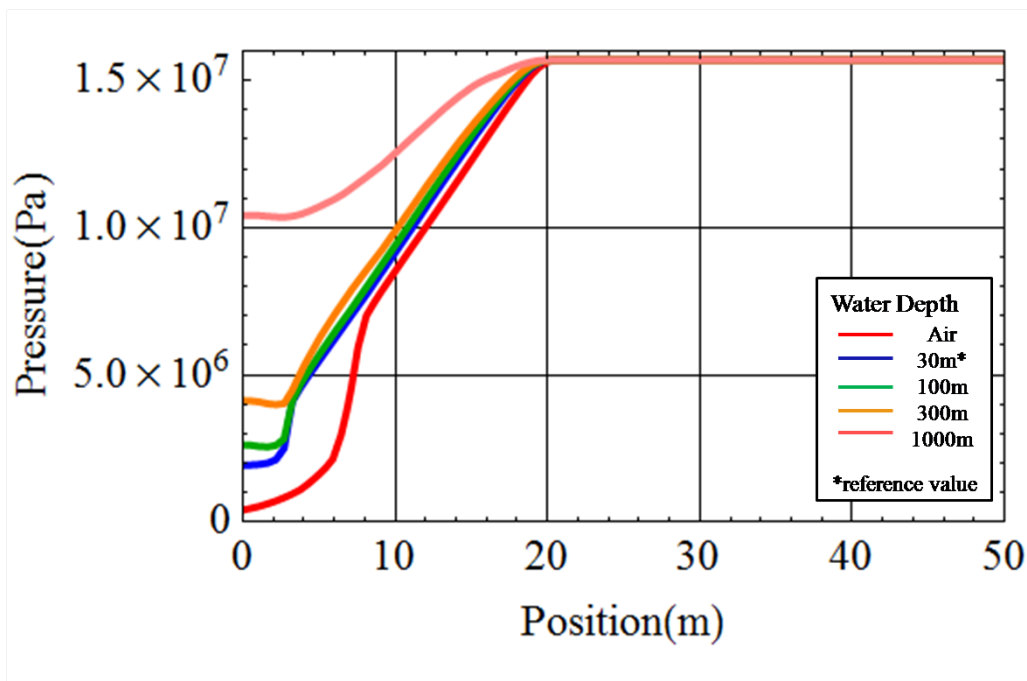


Fig. 6.2 Dependence of internal pressure distributions on water depth, $t=50$ ms

in Fig. 6.3.

The peak velocities at the beginning increases with decreasing pipe thickness, and unstable propagation happens only for the case with pipe thickness of 10mm. This trend is reasonable because circumferential stress in a pipe inversely increases with decreasing pipe thickness. The calculated results also indicate that the reduction of pipe thickness to half of the reference value has almost the same effect as lifting up offshore pipeline in water depths of 30m to the ground; in other words, there is a possibility that pipe thickness can be reduced in offshore pipelines regarding the safety against unstable ductile crack propagation.

Table 6.3 Changed pipe thickness

Pipe thickness (mm)
10
15
20.5(reference value)
25
35

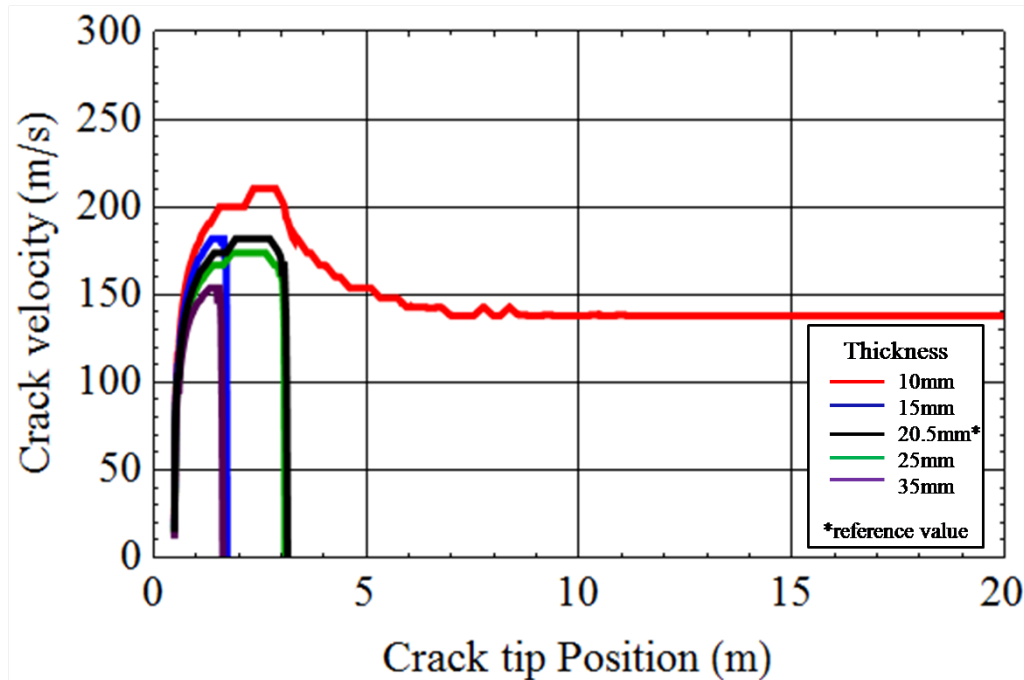


Fig. 6.3 Dependence of crack propagation/arrest on pipe thickness

6.4 Pipe outer diameter

Calculations were conducted by changing pipe outer diameter from 15inch to 80inch, see Table 6.4. Calculated histories of crack propagation are shown in Fig. 6.4. The peak velocities at the beginning decreases with decreasing pipe outer diameter, and crack arrest lengths decreases with decreasing pipe outer diameter. Although unstable crack propagation does not happen in any cases, the trend that decreasing pipe outer diameter makes a crack more likely to be arrested is reasonable because circumferential stress in a pipe proportionally decreases with decreasing pipe outer diameter. However, the calculated results indicate that the effect of pipe outer diameter is not as strong as that of pipe thickness.

6.5 Pipe grade(tensile yield strength)

Calculations were conducted by changing pipe grade from X40 to X100, see Table 6.5. Calculated histories of crack propagation are shown in Fig. 6.5. The calculated results indicate that the effect of pipe grade is much weaker than that of other parameters.

Table 6.4 Changed pipe outer diameter

Pipe outer diameter (inch)
15
20
36(reference value)
60
80

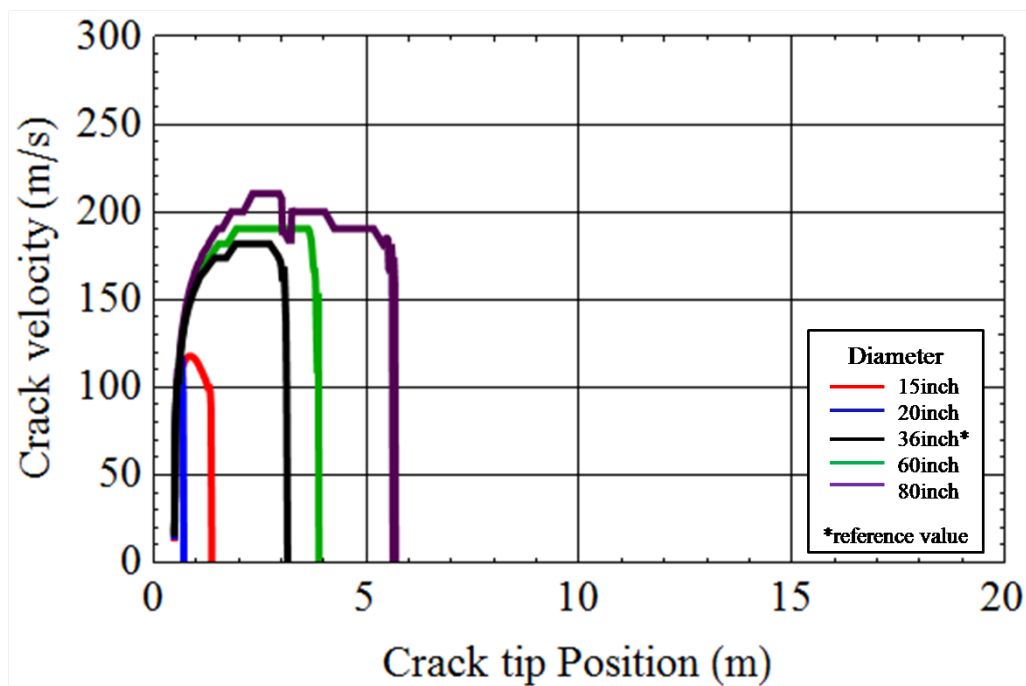


Fig. 6.4 Dependence of crack propagation/arrest on pipe outer diameter

Table 6.5 Changed pipe grade

Pipe grade (tensile yield strength)

X40(276MPa)
X50(345MPa)
X60(413MPa reference value)
X80(551MPa)
X100(689MPa)

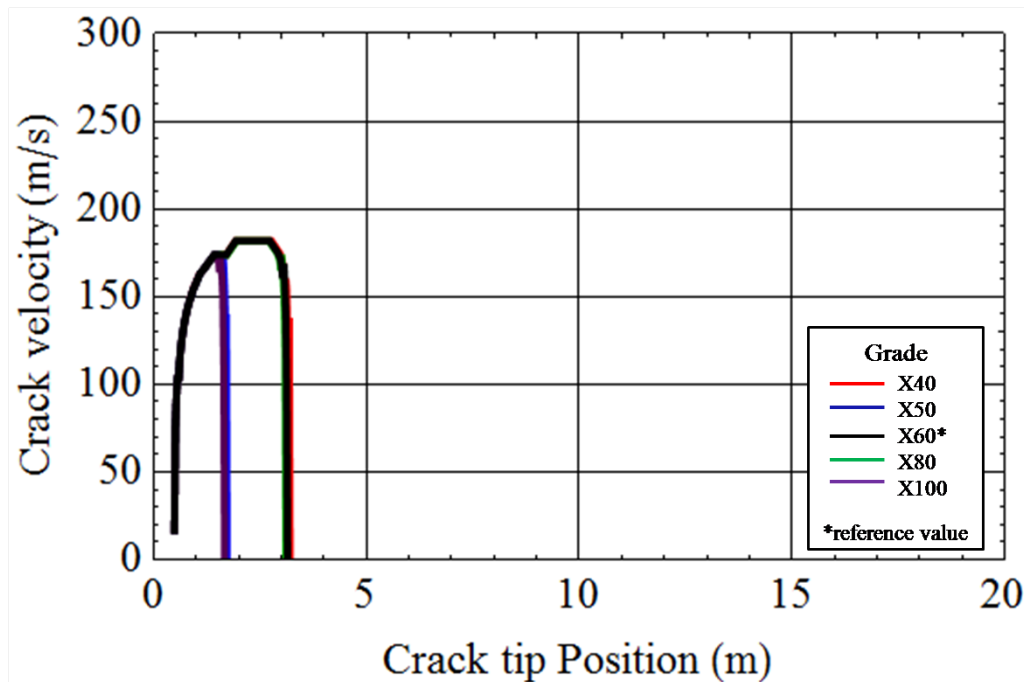


Fig. 6.5 Dependence of crack propagation/arrest on tensile yield stress (pipe grade)

6.6 Toughness

Calculations were conducted by changing toughness of the all pipes in the test section as shown in Fig. 5.1, from one-tenth of reference value to nine-tenth of the reference value, see Tab. 6.6. Note that toughness referred here corresponds to Charpy energy. Calculated histories of crack propagation are shown in Fig. 6.6. The peak velocities at the beginning increases with decreasing toughness, and unstable propagation happens only for the case with toughness ratio of 0.1. The calculated results that increasing toughness makes a crack more likely to be arrested is reasonable. The calculated results also indicate that the reduction of toughness to one-tenth of the reference value has almost the same effect as lifting up offshore pipeline in water depths of 30m to the ground; in other words, there is a possibility that pipe toughness can be reduced in offshore pipelines regarding the safety against unstable ductile crack propagation. In the present calculated result, unstable ductile crack propagation does not happen if the toughness is reduced to half of reference value.

Table 6.6 Changed toughness	
Toughness ratio to reference value	
	0.1
	0.5
	0.7
	0.9
	1.0(reference value)

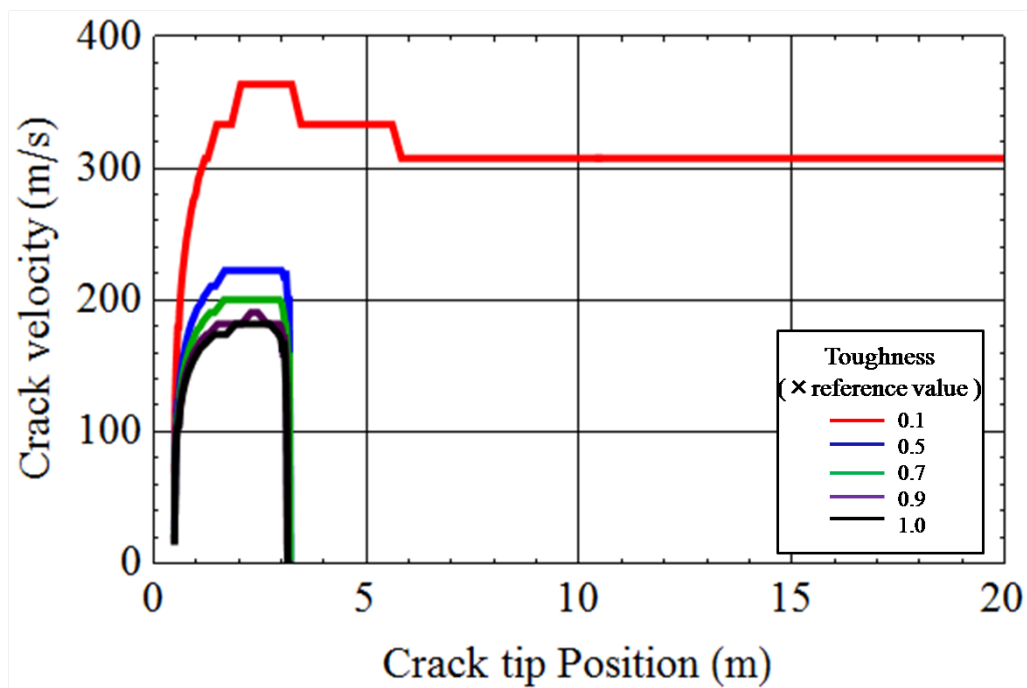


Fig. 6.6 Dependence of crack propagation/arrest on toughness

6.7 Summary

- Parametric studies are conducted by changing water depth, pipe thickness, pipe outer diameter, pipe grade and toughness.
- Increasing water depth makes a crack more likely to be arrested mainly because increasing hydrostatic pressure and water backfill have strong effect on crack propagation in offshore pipelines
- The effects of pipe thickness, pipe outer diameter, pipe grade and toughness on unstable ductile crack propagation/arrest are discussed.

Chapter 7

Conclusions

7.1 Summary of the present study

In the present study, numerical model for the safety design against unstable ductile fracture in offshore pipelines, which is called the UT offshore model, was developed. There has not been any established numerical model considering the interactions between pipe deformation, gas decompression, bubble growth and crack propagation. In the UT offshore model, the above phenomenon are formulated based on the mechanical approach such as material mechanics, elastic mechanics, thermo dynamics, fluid mechanics and fracture mechanics. The features of the model are as follows:

- Pipe deformation, gas decompression and bubble growth are formulated based on time dependent one-dimensional partial differential equations which are solved by finite difference method.
- The model is weak two-way coupling model where the interactions between pipe deformation, gas decompression, bubble growth and crack propagation are considered.
- Pipe deformation is formulated using a single parameter, shape parameter determining pipe deformation profile in the cross section. In the pipe deformation modeling, the effect of hydrostatic pressure on pipe deformation is incorporated.
- Water backfill effect, which constrains pipe deformation, is formulated as an added density effect.
- Gas decompression and bubble growth are modeled as one-dimensional compressible gas flow under the isentropic condition. For the bubble growth modeling, the increase in the bubble radius is described

modifying the bubble growth equation derived from Rayleigh-Plesset equation in the bubble dynamics.

- One of water effects that gas decompression is delayed by bubble generation/growth is incorporated into the model by formulating mass flow rate from a pipe to a bubble through a crack opening.
- Crack propagation is judged by dynamic energy balance, where strain energy generated by pipe deformation behind a crack tip, work done by gas to a pipe wall, kinetic energy of a pipe wall and strain energy generated by a crack tip singularity, which is usually referred to as resistance for crack propagation, are considered.
- Because the model is based on one-dimensional finite differential method, lower CPU cost is consumed as compared with three-dimensional finite element based models. Therefore, the model has a potential as an engineering tool for offshore pipeline design.

For the validation of the bubble growth modeling in the UT offshore model, small-scale underwater pipe rupture tests were conducted on pure aluminum pipes pressurized by pure nitrogen in water depth of 1m. The results from the tests are as follows:

- Tested pipes successfully bursted at intended pressure close to 1MPa.
- Time histories of dynamic internal and external pressure were measured.
- Time histories of bubble profile were successfully captured by high-speed camera with filming rate of 5,000fps.
- Quantitative data of time histories of bubble profile was obtained using image processing code developed by the author.

Calculations for the rupture tests using bubble growth modeling in the UT offshore model were conducted. The results from the calculations are as follows:

- The calculated time histories of dynamic internal pressure were in good agreement with the experimental ones.

- the calculated time history of bubble profile for the case with longer initial notch length were in good agreement with the experimental one. On the other hand, there was no close agreement between calculated and experimental result for the case with shorter initial notch length.
- It is clarified that the present bubble growth modeling is applicable only if there is no appreciable bubble growth in the axial direction. If the bubble grows beyond the crack tip, prediction accuracy of bubble growth might drop. However, this discrepancy can be small for a propagating crack.

Also, for the validation of the whole UT offshore model, a calculation for the full-scale offshore pipeline burst test performed ever by C.S.M was conducted. The results from the calculations are as follows:

- Calculated time histories of the dynamic internal pressure showed generally good agreements with the experimental ones.
- The UT offshore model successfully predicted arrest length; both of calculated and experimental arrest length were within one pipe, which means that unstable ductile crack did not happen.
- It is suggested that the UT offshore model is applicable to full-scale offshore pipeline burst tests.
- Because the number of full-scale offshore pipeline burst tests performed ever is so small, the complete validation of the whole UT model is inevitably difficult. More full-scale offshore pipeline burst tests especially on newer grade pipe in the deeper water are necessary in the future.

Finally, parametric studies were conducted by changing water depth, pipe thickness, pipe radius, pipe grade and toughness to discuss the effects of each parameter on unstable ductile crack propagation/arrest in offshore pipelines. The obtained remarks are as follows:

- Increasing water depth makes a crack more likely to be arrested mainly because increasing hydrostatic pressure and water backfill have strong effect on crack propagation in offshore pipelines although increasing water depth results in gas decompression delay which keeps crack driving force at higher level.

- Peak crack velocities increases with decreasing pipe thickness, and the trend toward the occurrence of unstable ductile crack propagation is strengthened by decreasing pipe thickness.
- Peak crack velocities increases with increasing pipe outer diameter, and the trend toward the occurrence of unstable ductile crack propagation is strengthened by increasing pipe outer diameter.
- Dependence of crack propagation/arrest on pipe grade (yield strength) is not clearly observed.
- Peak crack velocities increases with decreasing pipe toughness, and the trend toward the occurrence of unstable ductile crack propagation is strengthened by decreasing pipe toughness.

Although all the above remarks correspond to general understandings and are reasonable, the fact that the UT offshore model is able to present quantitative evaluation is crucially important. Therefore, the UT model has a potential as an engineering tool for offshore pipeline design such as required toughness, design pressure, pipe geometry and so on. It shall be noted that the UT offshore model is for the safe design against unstable ductile crack propagation. When designing offshore pipelines, the safety design against other fracture types such as brittle crack and fatigue crack is also necessary.

7.2 Future works

The UT offshore model contains some shortcomings to be improved as follows:

- A mesh size dependency is not clarified yet.
- More calculations for the validation of the model is necessary.
- Speed dependency of strain energy ahead of a crack tip, which is regarded as J resistance in fracture mechanics, is determined by limited experimental data. Moreover, the mechanism of speed dependency is not clarified yet.
- Bubble expansion to the axial direction beyond a crack tip is not incorporated.

- External dynamic pressure generated by rapid bubble growth is not calculated. As mentioned in the present thesis, external dynamic pressure is expected not to affect unstable ductile fracture behavior strongly. However, understandings on external dynamic pressure is crucially important in risk assessment.

The author will be continuously improving the UT offshore model especially regarding the above topics. The eventual goal is that the UT offshore model is adopted as a tool for offshore pipeline design in pipeline industry.

Bibliography

- [1] IEA. Key world energy statistics 2014.
- [2] 井原賢. 非在来天然ガスの開発技術の動向. 配管技術, Vol. 53, No. 9, pp. 1–10, July 2011.
- [3] Asia Pacific Energy Research Centre. Natural gas pipeline development in southeast asia. March 2000.
- [4] Asia Pacific Energy Research Centre. Natural gas pipeline development in northeast asia. April 2000.
- [5] 経済産業省資源エネルギー庁. エネルギー白書 2014.
- [6] Heleen de Coninck et.al. B.Metz, O.Davidson. *Carbon Dioxide Capture and Storage*. Cambridge University Press, 2005.
- [7] 大橋一彦. 天然ガス・パイプライン利用によるCO₂、H₂、バイオガスの輸送（その3）. 配管技術, pp. 74–75, December 2007.
- [8] British Geological Survey. Storing carbon dioxide beneath the moray firth explored. <http://www.bgs.ac.uk/research/highlights/2010/scottishCCS.html>, 2010.
- [9] 越後屋佐助. 世界の石油及び天然ガス・パイプライン計画(その3). *Applied Mechanics Reviews*, Vol. 53, No. 10, pp. 7–13, August 2011.
- [10] 一般社団法人日本エネルギー学会天然ガス部会輸送・貯蔵分科会. 天然ガスパイプラインのすすめ. 日本工業出版, 2011.
- [11] Saipem. Offshore pipelines -engineering and construction project references-. 2012.
- [12] Nord Stream AG. Pipelay vessel castoro sei. <https://www.nord-stream.com/press-info/images/pipelay-vessel-castoro-sei-with-numbers-2658/>, 2010.

- [13] Eurogas. Eurogas statistical report. 2010.
- [14] Nord Stream AG. European gas pipeline system. <http://www.nord-stream.com/press-info/images/european-gas-pipeline-system-2915/>, 2011.
- [15] K.Chiba. Sakhalin to japan gas pipeline project. 溶接構造シンポジウム 2004 論文集, pp. 235–242, 2004.
- [16] R.M.Andrews. The fracture arrest behaviour of 914 mm diameter x100 grade steel pipelines. In *Proc. of Int. Pipeline Conf.2004*, Calgary, 2004. IPC2004-0596.
- [17] W.A Maxey. *Fracture initiation, propagation, and arrest in 5th symp. line pipe research*. Catlog No.L30174. Pipeline Research Committee of A.G.A, November 1974.
- [18] H. Mimura. Some consideration on the condition of crack propagation in gas pipe line. In *Proc. of 16th Japan Congress on Materials Research*, Kyoto, Japan, 1973. The Society of Materials Science.
- [19] E.Sugie, M.Matsuoka, T.Akiyama, H.Mimura, and Y.Kawaguchi. A study of shear crack propagation in gas-pressurized pipelines. *Journal of Pressure Vessel Technology*, Vol. 104, pp. 338–343, 1982.
- [20] E.Sugie, H.Kaji, T.Taira, M.Ohashi, and Y.Sumitomo. Shear fracture arrestability of controlled rolled steel x70 line pipe by full-scale burst test. *Journal of Pressure Vessel Technology*, Vol. 106, pp. 55–62, 1984.
- [21] E.Sugie, M.Matsuoka, T.Akiyama, K.Tanaka, and Y.Kawaguchi. Notch ductility requirements of line pipes for arresting propagating shear fracture. *Journal of Pressure Vessel Technology*, Vol. 109, pp. 428–434, 1987.
- [22] H.Makino, T.Inoue, S.Endo, T.Kubo, and T.Matsumoto. Simulation method for crack propagation and arrest of shear fracture in natural gas transmission pipelines. Pipe Dreamer ' s Conf., Yokohama, 2002.
- [23] H.Makino, I.Takeuchi, and R.Higuchi. Fracture propagation and arrest in high-pressure gas transmission pipeline by ultra high strength line pipes. In *Proc. of 7th Int. Pipeline Conf.*, Calgary, 2008. IPC2008-64078.

- [24] H.Makino, I.Takeuchi, and R.Higuchi. Fracture arrestability of high pressure gas transmission pipelines by high strength linepipes. In *Proc. of Pipeline Tech. Conf.*, Ostend, 2008. Ostend2009-008.
- [25] A. F. Emery, Y. H. Chao, A. S. Kobayashi, and W. J. Love. Numerical modeling of full-scale pipe rupture tests. *Int.J.Pressure Vessels and Piping*, Vol. 114, pp. 265–270, 1992.
- [26] C.P.Leung G.Demofonti P.E.O'Donoghue, M.F'¿Kanninen. The development and validation of a dynamic fracture model. *Int.J.Pressure Vessels and Piping*, Vol. 70, pp. 1–5, 1997.
- [27] S. Yoshimura, M. Ino, H. Akiba, S. Igi, T. Inoue, and H. Makino. Development of 3d finite element simulation system for burst phenomenon of pipelines containing high pressure liquid natural gas. *CAMP-ISIJ*, Vol. 22, pp. 394–397, 2009.
- [28] P. Salvini, A. Fonzo, and G. mannucci. Identification of ctoa and fracture process parameters by drop weight tear test and finite element simulation. *Journal of Engineering Fracture Mechanics*, Vol. 70, pp. 553–566, 2003.
- [29] P. Aursand, T. Berstad, C. Dorum, M. Hammer, S. T. munlejord, and H. O. Nordhagen. Coupled fluid-structure simulation of running fracture in co2 pipelines. In *Proc. of 3rd Int. Forum on the Transportation of CO2 by Pipeline*, Newcastle, 2012.
- [30] K.Misawa, Y.Imai, and S.Aihara. a new model for dynamic crack propagation and arrest in gas pipelines. In *proc. of 8th Int.Pipeline Conf.* IPC2010-31475.
- [31] L. B. Freund. Running ductile fracture in a pressurized line pipelines. *ASTM STP 590*, pp. 243–262, 1976.
- [32] H.Nakai, K.Misawa, and S.Aihara. Numerical model for unstable ductile crack propagation / arrest in natural gas pipelines incorporating backfill effect. In *Proc. of 11th Int. Pipeline Conf.*, Calgary, 2014. IPC2014-33709.
- [33] W.A.Maxey. Fracture propagation in underwater gas pipelines. *Journal of Energy Resources Technology*, Vol. 108, pp. 29–34, 1986.

- [34] T.Inoue. Crack propagation and arrest of structural steels and pipelines. In *Doctoral thesis at Norwegian University of Science and Technology*, 2008.
- [35] H.Nakai. Experimental and numerical analyses on unstable ductile fracture in offshore pipelines. Master's Thesis The University of Tokyo, February 2012.
- [36] G.Demofonti, A.Maresca, and G.Buzzichelli. Ductile fracture propagation and arrest in offshore pipelines. *Applied Mechanics Reviews*, Vol. 41, No. 2, pp. 85–95, February 1988.
- [37] 松尾一泰. 圧縮性流体力学—内部流れの理論と解析—. 理工学社, 1994.
- [38] 九州大学大学院総合理工学府大気海洋環境システム学専攻. 地球環境をまなぶための流体力学. 成山堂書店, 2001.
- [39] 三宅哲. 熱力学. 裳華房, 1989.
- [40] C.E.Brennen. *Cavitation and Bubble Dynamics*. Oxford University Press, 1995.
- [41] 鷺津久一郎. 弾性学の変分原理概論. 培風館, 1972.
- [42] K. Gotoh, H. Hirasawa, and M. Toyosada. A simple estimating method of constitutive equation for structural steel as a function of strain rate and temperature. *Journal of the Society of Naval Architects of Japan*, Vol. 176, pp. 501–504, 1994.
- [43] M. Toyosada and Gotoh K. The estimating method of critical σ_{td} and J integral at arbitrary crosshead speed. *Journal of the Society of Naval Architects of Japan*, Vol. 172, pp. 663–674, 1992.
- [44] R.J.Eiber, T.A.Bubenik, and W.A.Maxey. Fracture control technology for natural gas pipelines. In *PRCI*, Catalog No,L51691, December 1993.
- [45] NIST Standard Reference Database 23. Nist reference fluid thermodynamic and transport properties-refprop. In *ver.9.0*, 2010.
- [46] Shen Wang B.L.Mehaute. *Water waves generated by underwater explosion*. Advanced Series on Ocean Engineering Vol.10. World Scientific, 1995.

- [47] C.Hsu, C.Liang, A.Nguyen, and T.Teng. A numerical study on the underwater explosion bubble pulsation and the collapse process. *Journal of Ocean Engineering*, Vol. 81, pp. 29–38, 2014.
- [48] Zhang A, W.Shi, H.Chao, and W.Bin. Influences of initial and boundary conditions on underwater explosion bubble dynamics. *European Journal of Mechanics B/Fluids*, Vol. 42, pp. 69–91, 2013.
- [49] J.Li and J.Rong. Bubble and free surface dynamics in shallow underwater explosion. *Journal of Ocean Engineering*, Vol. 38, pp. 1861–1868, 2011.
- [50] M. Di Biagio G. Demofonti A. Meleddu, M. Bertoli. Co2 decompression modeling for ductile fracture propagation control in deep-water pipelines. In *24th Int. Ocean and Polar Engineering Conf.*, pp. 198–204, June 2014.
- [51] S. Aihara, K. Shibayama, Imai Y, T. Fujishiro, and T. Hara. Evaluation on dependence of ductile crack propagation resistance on crack velocity. In *proc. of 9th Int. Pipeline Conf. IPC2012-90637*.
- [52] 栗飯原周二. 鋼管における破壊形態とその制御について. 西山記念技術講座, 日本鉄鋼協会, 2010.